The effect of surface waves on buoyant jets

Alistair Charles Shawcross

A thesis submitted in fulfilment of the requirements

for the degree of Doctor of Philosophy

to the

University of Edinburgh

2002

Abstract

A Laser Induced Fluorescence (LIF) technique has been used to measure the effect of surface waves on the dilution of a line plume produced by the merging of buoyant jets discharged from a model outfall. Full-field, time averaged concentration maps were produced of plumes both in wave and still conditions. From these an increase in dilution was found comparable with published values for wave effects on round plumes. The full field nature of the technique also allowed the region of the plume in which the increase in dilution takes place to be clearly identified.

LIF and Particle Image Velocimetry (PIV) measurements were also made of a single round buoyant jet discharged into quiescent and simulated wave conditions. Again full-field, time averaged concentration and also velocity maps of the plume were produced and increases in dilution due to wave effects were found to be in line with previously published data. The apparatus allowed LIF measurements to be taken under simulated wave conditions that could be used to produce three dimensional concentration maps of the plume.

Finally, proposed improvements to the current experimental techniques are outlined along with areas of possible future research.

Acknowledgements

I would like to thank my supervisor, Professor Clive Greated, for his guidance and support throughout this work. Particular thanks also go to Dave Sharp, Frank Morris for continually bailing me out of problems (almost literally on occasion), the technicians in the workshops for building my apparatus and everyone who helped me with my computer problems, especially John Pullen, Alistair Young and Liz McIvor. Thanks also to Will Hossack for those little bits of information that nobody else would know. Also thanks go to my office mates, Ted, Anthony, Scott, Tom, Dawn and the rest of Susan's gang, Big Jim, John Cosgrove, Dave and Naz and especially Arny for the climbing trips.

Thanks of course go to my other friends and flatmates (including Barry) namely Alan, Chris, Emily, Claire, Lucy and John for all their friendship and support during my time in Edinburgh. Also to the big and little kids for giving me a weekly break from student life and some great weekends away.

Finally thanks to my Mum, Dad and Lissie for their help throughout my time at university and also to Emma for putting up with me.

This project was funded by the Engineering and Physical Sciences Research Council (EPSRC) and their support is greatly appreciated.

Declaration

I declare that this thesis was composed by myself and that, except where explicitly stated otherwise in the text, the work contained therein is my own

(*Alistair C. Shawcross*)

June 2002

Table of Contents

List of Figures

List of Tables

Chapter 1

Introduction

Waste fluid is commonly discharged into the marine environment by means of submerged outfall pipes. In order to limit the impact on the surrounding area, a high initial dilution must be obtained. This is usually achieved by terminating the outfall pipe with a multi-port diffuser. At its simplest this may consist of a length of pipe with ports at regular intervals along its side (fig. 1.1a) or, where conditions necessitate the pipe being buried, a pipe with multiple risers along its length leading to the ports (fig. 1.1b)[1].

As the effluent is often less dense than the receiving water it will be discharged initially as a buoyant jet that may then form a plume [2]. While the properties of such jets and plumes have been well studied [3], as have the mechanics of outfall diffusers [4], the effects of surface waves, a common feature in the marine environment, on buoyant jets such as those produced by outfalls are less well understood.

This thesis reviews previous experimental and theoretical work and describes experiments conducted to investigate the effect of surface waves on buoyant jets of the type commonly associated with marine discharges. Measurements of velocity and concentration were made using Particle Image Velocimetry (PIV) and Laser Induced Fluorescence (LIF) respectively. These are both optical techniques

allowing non intrusive, full field measurements to be made.

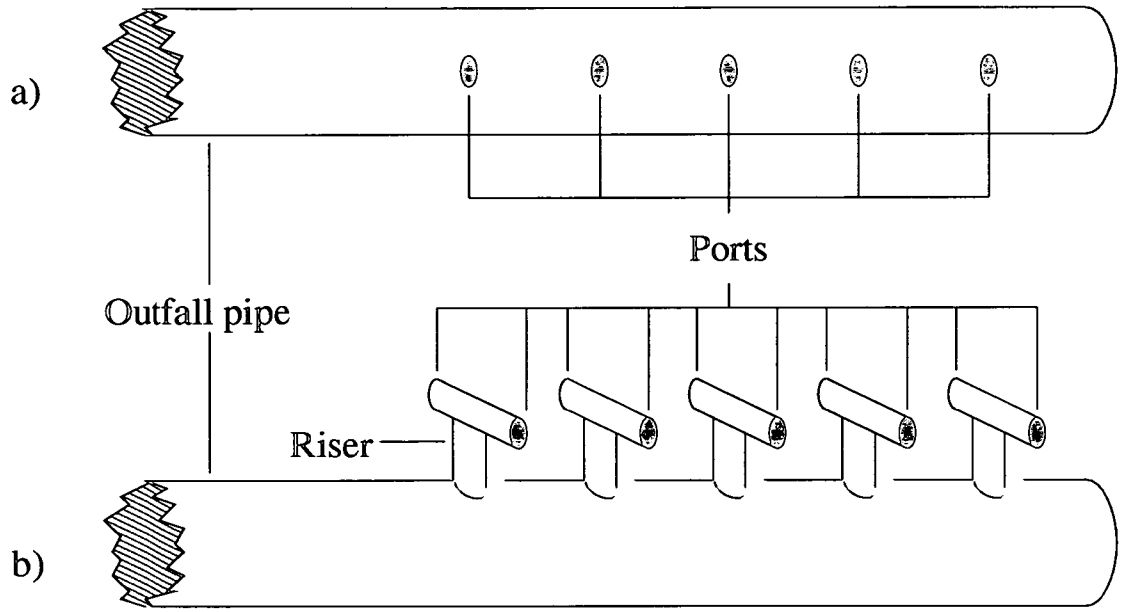

Figure 1.1: Two typical multi-port diffusers terminating outfall pipes. a) Typical configuration for outfall laid on sea bed. b) Typical configuration for buried outfall with risers lifting ports above sea bed.

1.1 Jets, buoyant jets and plumes

The fundamental difference between a jet and a plume is the source of the energy that drives the flow. A pure jet, which may be formed by the discharge of a fluid through an aperture into a larger body of the same or a similar fluid, is purely momentum driven. For example the water issuing from a hose-pipe held into a bath of water will be discharged as a jet of water. The smoke rising in a plume above a fire however, is driven solely by buoyancy due to the density difference between the warm air above the fire and the colder surrounding air. A pure plume therefore is a flow which is solely driven by a source of potential energy that provides the fluid with either negative or positive buoyancy in comparison with its surroundings.

Discharges of the type studied in the present work may however be classed as buoyant jets, flows driven by both momentum and buoyancy. Though the discharge is initially almost exclusively momentum driven, as the effluent is less dense than the receiving fluid, buoyancy will also affect the jet. As the fluid moves away from the discharge port so the effect of the jets' initial momentum will be reduced. The effects of buoyancy will then dominate, tending in the far field to a pure plume.

Jets and plumes may be either laminar or turbulent and, as with pipe flow, this may be described by the flow's Reynolds number. Though, unlike in pipe flow, it is not yet possible to predict at what value of Reynolds number a laminar jet will become turbulent [2]. Experiments performed have shown that a jet with a Reynolds number of 2000 may be described as turbulent, though the turbulence will not be fully developed until a Reynolds number of 4000 [2]. In practice most marine discharges will be turbulent in nature and this must be taken into account when modelling such discharges.

1.2 Previous Studies

1.2.1 Jets and Plumes

As previously mentioned the physics and mechanics of jets and plumes have both been well studied, experimentally and theoretically, both as phenomena in themselves and also with reference to outfall diffusers. Good overviews are given by both Fischer et al [2] and List [3]. Work by Papanicolaou and List [5, 6] however is of particular interest. They not only investigated buoyant jets with reference to outflows, but they too used optical measuring techniques for both concentration and velocity measurements.

Velocity measurements were taken using Laser Doppler Anemometry (LDA - also known as LDV, Laser Doppler Velocimetry). This technique is based on

measuring the Doppler signal in laser light scattered by seeding particles in a small interrogation area within the flow [7]. Simultaneously LIF concentration measurements were made at the same point by measuring the light intensity from a fluorescent dye present in the flow. The LIF technique is described in greater detail in chapter 3. While both velocity and concentration measurements were gained without disturbance of the flow, the technique employed still limited measurement to that of a single point in the flow. Measurement of the entire flow field would therefore require large numbers of experiments to be performed. Despite this limitation their study investigated a wide range of momentum jets and both positive and negatively buoyant jets, their data confirming many of the theoretically predicted results for jets.

1.2.2 Outfalls and multi port diffusers

As the construction of large outfalls may be extremely expensive, a lot of work, both experimental and theoretical has been conducted on the performance of different diffuser configurations. The main aim of these studies has been to produce the required dilution of the effluent for the minimum construction cost given the environmental conditions that exist at the proposed site; currents, natural stratifications and tides. A good overview of outfall design, giving a number of examples of actual outfalls is given by Roberts [4]. Further examples, where environmental conditions lead to more elaborate diffuser configurations are also given by Roberts and Toms [8], Roberts and Snyder [9] and Isaacson et al[10].

1.2.3 Wave-jet interaction studies

The first work on the effect of surface waves on buoyant jets was conducted by Shuto and Ti [11] who investigated the effects of standing waves on a round, fresh water jet discharged vertically into salt water.

While they were interested in the effect of waves on plumes, the work was not based on specifically modelling realistic outfalls. The discharge parameters that they studied therefore were not those typically associated with realistic outfalls. Buoyancy effects were relatively unimportant through the full rise height and the wave parameters too were more extreme than those normally encountered near outfalls, the induced motion being uniform with depth.

Concentration measurements were taken within the waste-field at three points 1-2cm below the free surface: one above the outlet; one 50cm upstream; and the other 50cm downstream. To make measurements the plume was allowed to reach steady state before the wave-maker was turned off and samples were then siphoned from the three points. The siphoning rate was controlled so as not to entrain liquid from other layers. Spectrophoto analysis was then used to find the chromium concentration in the samples and by comparison with chromium levels in the fresh water, the concentration determined.

While limited by a point measuring technique, their work showed that plumes released under the influence of waves had a lower surface dilution than those discharged into ambient conditions. They concluded that the diluting factor was inversely proportional to the ratio of the discharge velocity to a characteristic horizontal velocity of the ambient fluid, the characteristic horizontal velocity of the ambient fluid that they used being the mean wave induced velocity, averaged over half a wave period.

As well as producing a relationship for the surface dilution, an expression for an entrainment coefficient, defined as the ratio of entrainment velocity to the velocity exciting the entrainment, was also proposed. While of practical value in calculating surface dilutions of plumes in a wavy environment, the theoretical background behind the proposed expression was physically unrealistic. This led to values greater than unity being predicted for some discharge conditions.

Later, Ger [12] based on earlier experimental work by himself and Çiray [13],

examined the effect of waves on a horizontally discharged, round, buoyant jet. Their discharge and wave conditions however were also outside the range usually associated with outfalls, the wave induced motion again being almost uniform with depth and the discharge being momentum dominated for at least half of the rise height.

They noted a 'significant effect' of the wave motion on both jet trajectory and on dilution due, they theorised, to increased entrainment resulting from the induced horizontal motion of the plume and an altered rate of rise.

Like Shuto and Ti, Ger found that the axial dilution varied linearly with the ratio of the average wave velocity over half a wave period to the outlet velocity. However unlike Shuto and Ti, his proposed expression for the entrainment coefficient was more physically viable. Using expressions proposed by Chan and Kennedy [14] for the jet trajectory and axial dilution, he defined a modified entrainment coefficient to take into account the wave motion. Agreeing with accepted values for quiescent conditions, his entrainment coefficient was also shown to vary linearly with wave effect.

While not directly linked to the type of jets associated with outfalls, a study by Ismail and Wiegel [15] gave results of interest to the present study. They investigated, both theoretically and experimentally, the effect of waves on a pure surface jet. Study of this type of phenomena is important in the understanding of flows such as rivers and tidal flows from bays entering the sea.

Their experiments studied a pure momentum jet discharged at the surface of the ambient water and compared the spreading rate of the jet in still water to that in opposing wave conditions. Measurements were made of the flow's velocity along the jet centreline using an electromagnetic flow sensor and the flow was also dyed to allow flow visualisation photographs to be taken.

They predicted that within the range of conditions studied there would be a linear

increase in the spreading rate of a developed jet due to opposing wave motion and their experiments showed this to be the case. Though actual concentration measurements were not made, conservation of mass implies that the increase in the rate of spreading would also lead to an increase in the rate of dilution.

The outfall problem was revisited by Chin [16] who investigated a horizontally discharged, single, buoyant jet under the influence of progressive, sinusoidal waves. His discharge and wave parameters however were carefully chosen to realistically match those of a typical outfall.

Unlike previous studies where the discharges had been more jetlike, that is momentum dominated, the discharges investigated by Chin became plumelike, that is buoyancy dominated, very quickly as is found in typical outfalls. The wave parameters were also modelled so that the wave-induced motions, while reaching the bottom, became less with depth. These are the wave conditions more commonly associated with the sites of outfalls.

Chin, like Shuto and Ti, was primarily interested in the wave effect on surface dilution. Therefore point measurements, using a siphoning technique, were made from the centre of the boil at the point where the plume surfaces. Again the rate of siphoning was controlled, this time to be smaller than the minimum flow rate at the top of the plume. This would again prevent entrainment of liquid from below the measurement point. Measurement of conductivity of the samples and calibration with known concentrations then allowed the dilution at the sampling point to be found.

Observation of the wave-induced plume motion suggested to Chin that the primary influence of the waves was close to the source of the discharge. He noted that when the wave motion opposed the discharge velocity then the jet would 'explode' and become plumelike closer to the port than under quiescent conditions. However when the induced motion was co-directional with the jet velocity, then the flow was observed to become plumelike further from the source than for

the no-waves case. Chin noted that the combined result of these two effects was a spraying effect at the source.

Once the plume began to rise he observed that the the whole plume was merely advected backwards and forwards and from a Lagrangian viewpoint, that it appeared no different to a plume under still ambient conditions. Like the previous researchers before him, his measurements of surface dilution again showed a linear relationship between increase in dilution and increased wave effect.

Following his experimental work [16], Chin developed a numerical model to simulate the effect of waves in increasing the dilution of a buoyant jet of the type associated with outfalls [17]. The model was based upon solving simultaneous equations describing the motion of the plume relative to the ambient fluid. Experimental results were also used to determine the value of two empirical entrainment coefficients: one describing the entrainment due to the rise of the plume; the other the entrainment due to the forced motion of the plume. The resultant model was able to give both the plume position and dilution for a range of discharge and wave conditions, though with some limitations in the latter.

The simulated surface centreline concentrations were compared to his earlier experimental work and showed good agreement. Further verification of the model was shown by setting the wave amplitude to zero and comparing with the work of Fan and Brooks [18] on buoyant jets under still conditions. The simulated schemematic of the plume position produced by the model, also showed features very similar to those produced in the earlier experiments, the primary feature of these being abrupt widenings of the plume along its axis.

While previous studies of buoyant jets had concentrated on the measurement of plume concentration alone, work by Chyan et al [19] made simultaneous point measurements of both concentration and velocities in a turbulent, round jet. Using a combined LIF-LDV system based on one used by Hwung and Chyan [20] and similar to that used by Papanicolaou and List [5, 6], they studied jets

discharged vertically into realistic wave conditions. In addition to the quantitative measurements, photographs of the fluorescing plume enabled visualisation of the whole flow.

The flow visualisation results showed that the jet was translated backwards and forwards, in the same way that Chin had observed the movement of a rising plume under wave conditions. Again conservation of mass would imply that as the area covered by the jet is larger than for ambient conditions, then there must be an increase in dilution. This was more clearly seen on time-averaged images of the jets motion which also showed that the rate of widening of the time-averaged jet boundary was not linear. Instead it showed two linear regions separated by a transition region. The first of these regions, closest to the discharge port, showed the highest rate of widening while the region above the transition region leading to the surface showed a lower rate of broadening.

While the reason for the large rate of spreading in the initial region was attributed to the wave induced motion's action on the direction of the jet rather than any increase in a mixing process, the investigators believed that the transition region did offer a new mixing mechanism. In this region they postulated that a large amount of fresh water would be enclosed by the jet fluid as it was oscillated by the wave induced motion. This, they thought, would lead to increased mixing opportunities between the ambient and jet fluid.

Their quantitative results seemed to reinforce the existence of this new mixing mechanism. Concentration measurements through cross sections of the plume in the transition region showed a profile with two peaks symmetric about the jet axis, rather than the Gaussian profile associated with jets in quiescent conditions. They attributed the lower axial concentration to the same observed process of the engulfing of fresh water by the jet which they named the 'enclosing mechanism'.

The observation that the rise of the jet under wave conditions could be characterised by a number of different regions was also shown by quantitative measure-

ment of the axial concentration. In the initial region close to the port a large decrease in concentration was measured corresponding to the region in which the jet was oscillated by the wave induced motion. The second or 'transition' region showed a small increase in dilution and this was attributed to the breakdown of the jet structure limiting entrainment of ambient fluid. Finally, in the third region, the jet showed a gradual decay of the jet concentration. This was explained as the characteristic scale of the jet having become larger than that of the wave induced motion.

Though not directly comparable, the authors having studied a vertically discharged pure plume and Chin a horizontally discharged buoyant jet, Chyan et al found that the effect on dilution in their study was almost twice that found by Chin. They concluded that the primary factor in this increase was the orientation of the jet, the enclosing mechanism being more powerful when the wave motion was orthogonal to the jet orientation.

In a later paper, Chyan and Hwung [21] further analysed the experimental results of their earlier work [19]. Their enclosing mechanism was renamed a 'wave tractive mechanism' and they also postulated that a further increase in dilution could take place due to the shedding of a wake vortex from the jet as it was oscillated by the wave. However they concluded that when the wave period was less than the shedding period a wake vortex could not fully develop and therefore the enlarged jet area and wave tractive mechanisms would be the dominant factors in increasing the dilution. They also proposed the title of 'deflection region' for the initial region of increased dilution due to jet deflection; 'transition region' for the area in which the rate of dilution is less or indeed negative; and finally a 'developed region' in which the dilution rate is similar to that for no waves cases in which the jet is merely oscillated horizontally by the wave motion.

Comparison was also once again made between Chin's and their own experimental results. While as mentioned previously the effect of wave motion seemed to be

greater for a vertically discharge jet, it was noted that the actual initial dilution was higher for a horizontally jet. Arguing that the wave tractive mechanism will have greater effect when the wave motion is orthogonal to the jet motion, but also acknowledging the higher initial dilution given by a horizontal discharge, it was suggested that even greater dilutions could be achieved if the jet was discharged horizontally but at right angles to the wave motion.

Returning to theoretical work Hwang, Yang and Chiang [22] produced a new numerical model based on that of Chin [17]. This overcame one of the limitations of the previous model; the inability to predict dilutions of plumes in waves inducing large vertical motions in the water column. Again solutions were found by solving simultaneous equations describing the plume's movement relative to the receiving water. However adjustments were made to allow the vertical motion induced by waves to be accounted for.

Comparison of predicted schematic plumes agreed well with those observed by flow visualisation experiments. Theoretical surface dilutions were also in agreement with both the experimental work of Chin and also Fan and Brooks's [18] model for a buoyant jet. As well as the positional and surface dilution simulations however, centreline velocity and concentration predictions were also presented, showing the effect of the wave on dilution increasing with rise height. Though no experimental work existed at the time for direct comparison, Chyan et al's[19] work having considered a vertically orientated jet; the velocity and concentration measurements from the present study however will produce data with which these simulations may be compared directly.

1.3 Present study

Following Chin's approach of modelling a realistic outfall, the present study investigated the effect of surface waves on a two dimensional, line, buoyant jet. This

is the type of flow produced by typical multi-port diffusers. Flows were studied in both quiescent conditions and under a range of realistic wave conditions.

To make concentration measurements over the full area of interest, rather than being limited to specific points as with earlier measuring techniques, a full field LIF technique was used. As this technique had not previously been used within the group it was necessary to develop equipment, techniques and analysis programs in order to make LIF measurements of the plume. This development is described in chapter 3.

It was also intended to make full field velocity measurements on these plumes using Particle Image Velocimetry (PIV) a further optical technique, but this proved impractical so further LIF and also PIV experiments were carried out on a single, three dimensional plume under simulated wave conditions. This further study also allowed comparison of the properties of the two dimensional, line plume to those of the three dimensional plume released from a point source in both still and wave conditions.

In the following chapters the theoretical background to the wave-buoyant jet problem is first described before an outline of the experimental techniques used is given. The experimental methods for the two sets of experiments undertaken are then outlined as well as the data processing techniques used. Finally the results from the two sets of experiments are presented and areas for further development of the work highlighted.

Chapter 2

Background

2.1 Summary

This chapter defines the equations describing the motions of flows investigated in this study. Those governing the behaviour of buoyant jets are first shown and as the flows in this study become plumelike very quickly, the equations for both line and round plumes are then given. Finally the effect of waves on the water column beneath them is reviewed, before the interaction between wave induced motion and that of a jet examined.

2.2 The buoyant jet

As described in chapter 1, the discharge from an outflow can initially be described as a buoyant jet and the most important factors governing a jet's dynamics are the mass, momentum and buoyancy fluxes of the flow [2].

For a turbulent jet, the mass flux $\rho\mu$, where μ is the specific mass or volume flux of the jet, is defined as the mass of fluid passing a jet cross section per unit time and is given by

$$\rho\mu = \int_A \rho w dA \tag{2.1}$$

where ρ is the fluid's density, A the cross-sectional area of the jet and w the

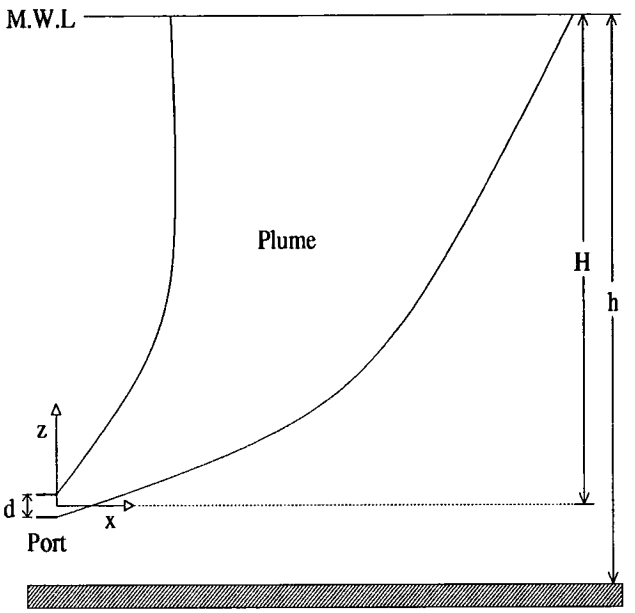

Figure 2.1: Schematic of plume showing discharge parameters

time-averaged jet velocity in the axial direction.

From the previous equation the momentum flux ρm, the amount of streamwise momentum passing a jet cross section per unit time, is then given by

$$\rho m = \int_A \rho w^2 dA \tag{2.2}$$

m being known as the specific momentum flux.

Finally, the buoyancy flux $\rho\beta$, defined as the buoyant weight of the fluid passing through a cross section per unit time is given by

$$\rho\beta = \int_A g\Delta\rho w dA \tag{2.3}$$

where g is the acceleration due to gravity, $\Delta\rho = \rho_a - \rho$, the difference between the density of the jet fluid ρ and the surrounding fluid ρ_a and β the specific buoyancy flux of the jet.

When examining the discharge parameters it will be the initial values of these fluxes that will be of interest and for round jets, the type used in this study, the

initial specific volume, momentum and buoyancy fluxes are defined respectively as

$$Q = \frac{\pi}{4} d^2 v_o \tag{2.4}$$

where d is the port diameter and v_o the initial port discharge velocity.

$$M = \frac{\pi}{4} d^2 v_o^2 \tag{2.5}$$

and

$$B = g'_o Q \tag{2.6}$$

where g'_o, the initial reduced gravity is given by

$$g'_o = \frac{\Delta\rho}{\rho_a} g \tag{2.7}$$

As well as the initial values of the fluxes a further useful quantity in determining the discharge's behaviour would be a characteristic length scale. For a pure jet, that is a flow which is purely momentum driven, this can be in terms of only Q and M. Combining these to give a dimension of length, the simple jet's characteristic length scale can then be defined as [2]

$$l_Q = \frac{Q}{M^{\frac{1}{2}}} \tag{2.8}$$

It is also useful to note that l_Q is then equal to the root of the jet's initial cross sectional area and more specifically for jets discharged from a round port

$$l_Q = \sqrt{A} = \sqrt{\frac{\pi}{4}} d \tag{2.9}$$

If z is taken to be the distance from the source along the jet centreline, then, for $z \gg l_Q$ the flow will be a fully developed jet, while for $z \sim O(l_Q)$, the flow is still controlled by the port geometry [2].

If a buoyant jet, a flow driven by both momentum and buoyancy, but one with no initial volume flux is considered, then a further characteristic length scale can be derived from the initial specific momentum and buoyancy fluxes M and B. Again

combining these to give a dimension of length a second characteristic length scale can be defined as [2]

$$l_M = \frac{M^{\frac{3}{4}}}{B^{\frac{1}{2}}} \tag{2.10}$$

From this length scale we are able to determine the jetlike or plumelike nature of the flow. For $z \gg l_M$ the flow will be plumelike, while for $z \ll l_M$, the flow will be jetlike [2].

The ratio of these two characteristic length scales $\frac{l_Q}{l_M}$ is known as the jet Richardson number R_o and defines how quickly a buoyant jet will become plumelike. If l_M and l_Q are of the same order then the buoyant jet will be plumelike from the start.

As mentioned in chapter 1 however, in the design of out-falls the properties of jet are more commonly classified by two dimensionless quantities, the Reynolds and Froude numbers. The former, a measure of how turbulent the discharge is, is given by the ratio of inertial to viscous forces in the flow

$$R = \frac{v_o d}{\nu_o} \tag{2.11}$$

where ν_o is the kinematic viscosity given by $\frac{\mu_o}{\rho_o}$, where μ_o is the initial viscosity of the plume and ρ_o its initial density.

For a round jet, such as those used in this study the Reynolds number may also be defined in relation to the initial value of the jet's specific momentum flux M, as

$$R = \frac{M^{\frac{1}{2}}}{\nu_o} \tag{2.12}$$

In order for the flow to be turbulent, as it is from a real diffuser, the discharge Reynolds number must be greater than 4000 [2]. In this study, at the port the discharge had a Reynolds number of 4600, ensuring the discharge was turbulent.

The second quantity, the port densimetric Froude number, which again determines how soon the discharge evolves from a jet to a plume, is defined as the

ratio of inertial to buoyancy forces in the flow

$$F_d = \frac{v_0}{\sqrt{g'_o d}} \tag{2.13}$$

In terms of the initial specific fluxes and characteristic length scales, for a round jet the Froude number can be written as

$$F_d = \left(\frac{\pi}{4}\right)^{\frac{1}{4}} \frac{l_M}{l_Q} = \left(\frac{\pi}{4}\right)^{\frac{1}{4}} \frac{M^{\frac{5}{4}}}{QB^{\frac{1}{2}}} \tag{2.14}$$

Typical outflows have Froude numbers of 16 [16] and from equation 2.14 we can see that this would lead to a flow with l_Q approximately 16 times larger than l_M and therefore a flow which becomes plumelike very quickly. Indeed this is the case with a typical outflow and the flows investigated in this study were discharged with a Froude number of the same order as that of a typical outflow.

2.3 Plume parameters

2.3.1 Plume concentration

As we have already seen the parameters that govern a buoyant jet's behaviour are the initial values of its specific volume, mass and buoyancy fluxes and the distance from the source. Therefore any property of the flow may be written as a suitably non-dimensionalised function of these variables. The main parameter of interest in this investigation is the time-averaged, minimum centreline dilution S_m. Following Roberts [1], the local buoyant weight, from which the dilution may be obtained is taken as the dependent variable to give

$$g' = f(z, Q, M, B) \tag{2.15}$$

Dimensional analysis of these five variables using the Buckingham Π theorem [2] then gives three dimensionless variables

$$\frac{B^{\frac{3}{2}}}{M^{\frac{5}{4}}g'} \quad (2.16) \quad , \quad \frac{zM^{\frac{1}{2}}}{Q} \quad (2.17) \quad \text{and} \quad \frac{zB^{\frac{1}{2}}}{M^{\frac{3}{4}}} \quad (2.18)$$

which then gives

$$\frac{B^{\frac{3}{2}}}{M^{\frac{5}{4}}}\frac{1}{g'} = f\left(\frac{zM^{\frac{1}{2}}}{Q}, \frac{zB^{\frac{1}{2}}}{M^{\frac{3}{4}}}\right) \tag{2.19}$$

While the above non-dimensional groupings are not the only ones possible, grouping as above then easily allows substitution in terms of previously defined length scales. Thus using equations 2.8 and 2.10, the two terms on the right can be expressed in terms of the characteristic length scales to give

$$\frac{B^{\frac{3}{2}}}{M^{\frac{5}{4}}}\frac{1}{g'} = f\left(\frac{z}{l_M}, \frac{z}{l_Q}\right) \tag{2.20}$$

Now as S_m will be proportional to $\frac{g'_o}{g'}$ the previous expression becomes

$$\frac{1}{g'_o}\frac{B^{\frac{3}{2}}}{M^{\frac{5}{4}}}\frac{g'_o}{g'} = \frac{1}{g'_o}\frac{B^{\frac{3}{2}}}{M^{\frac{5}{4}}}S_m = f\left(\frac{z}{l_M}, \frac{z}{l_Q}\right) \tag{2.21}$$

substituting for g'_o using equation 2.6 and then using the Froude equation (eq. 2.14) then gives

$$\frac{S_m}{F_d} = f\left(\frac{z}{l_M}, \frac{z}{l_Q}\right) \tag{2.22}$$

However for the type of flows under investigation where the flow quickly becomes plumelike we can neglect the effect of l_Q and write this equation solely in terms of $\frac{z}{l_M}$

$$\frac{S_m}{F_d} = f\left(\frac{z}{l_M}\right) \tag{2.23}$$

l_M is not the most easily measured quantity, so using equation 2.9 to give an expression for l_M in terms of d and substituting into equation 2.14 gives

$$l_m = \left(\frac{\pi}{4}\right)^{\frac{3}{4}} F_d d \tag{2.24}$$

Finally substituting this into the equation for the centreline dilution gives

$$\frac{S_m}{F_d} = f\left(\frac{z}{dF_d}\right) \tag{2.25}$$

The exact coefficients must be found experimentally and for a pure round plume the equation is accepted to be [1]

$$\frac{S_m}{F_d} = 0.107 \left(\frac{z}{dF_d}\right)^{\frac{5}{3}} \tag{2.26}$$

with experimental results tending towards those given by the plume equation for $\frac{z}{l_M} > 10$ [1].

If we now consider a line of round ports as is often found on a multi-port diffuser, then a new parameter s, the port spacing must be taken into account. Therefore the minimum centreline concentration may be written in the form

$$\frac{S_m}{F_d} = f\left(\frac{z}{dF_d}, \frac{z}{s}\right) \tag{2.27}$$

If the receiving water is sufficiently deep, as is normally the case with out-falls, then each of the individual plumes will merge together to form a flow the same as that generated by a line source. In this case the coefficients for the equation are those of the line plume solution [1]

$$\frac{S_m}{F_d} = 0.50 \left(\frac{2z}{s}\right)^{-\frac{2}{3}} \left(\frac{z}{s}\right)^{\frac{5}{3}} \tag{2.28}$$

Previous experimental work has shown that for a row of round sources, the resultant plume's minimum centreline dilution will tend towards the line plume solution for $\frac{2z}{s} > 50$ [1].

2.3.2 Plume velocities

In the previous section it was seen that where buoyant jets become plumelike quickly the solutions to the resulting flow are given by the pure plume solutions. Therefore in determining the form of the equation for the maximum, time-averaged centreline velocity only the pure plume will be analysed.

Following the arguments of the previous section, all variables of a pure plume must be a function of only the buoyancy flux, the distance from the origin and the

viscosity of the fluid. Therefore the time-averaged, maximum centreline velocity may be written in the form

$$w_m = f(B, z, \nu) \tag{2.29}$$

However for fully turbulent flows the effects of viscosity will be very small and the equation can be written in terms of only B and z. Including the experimentally found coefficients then gives for a round plume[2]

$$w_m = 4.7 \left(\frac{B}{z}\right)^{\frac{1}{3}} \tag{2.30}$$

and for a plane plume

$$w_m = 1.66 \left(\frac{B}{z}\right)^{\frac{1}{3}} \tag{2.31}$$

2.3.3 Cross-sectional profiles

While the exact shape of both the initial jet and resultant plume of the discharge will vary with time, once the jet is established time-averaged measurements show a Gaussian concentration profile [2]. This may then be written in the form

$$C = C_m e^{-k(\frac{x}{z})^2} \tag{2.32}$$

where C is the concentration at a point, C_m the centreline concentration and x the radial distance from the centreline. The time-averaged velocity profile also shows a Gaussian distribution and in an established jet the two profiles are said to be self-similar. This means that any cross section through the jet or plume may be expressed in terms of the maximum, centreline velocity or concentration and a measure of the plumes width [2]. The concentration and velocity profiles may therefore be expressed as

$$C = C_m e^{-\left(\frac{x}{b_T}\right)^2} \tag{2.33}$$

and

$$w = w_m e^{-\left(\frac{x}{b_w}\right)^2} \tag{2.34}$$

The coefficients b_T and b_w must again be found experimentally and the accepted values for a round plume are $\frac{b_T}{z} = 0.120 \pm 0.005$ and $\frac{b_w}{z} = 0.100 \pm 0.005$ and for a plane plume $\frac{b_T}{z} = 0.157 \pm 0.003$ and $\frac{b_w}{z} = 0.116 \pm 0.002$ [2].

2.4 Wave theory

The waves used in the study (fig. 2.2), modelling those typically found at discharge sites, may be classed as being of small amplitude, that is with a small amplitude in comparison to their wavelength. Velocities found within these waves will therefore be small, allowing linear, or small amplitude wave theory to be used [23]. Full mathematical treatments of this theory may be found in other literature [23, 24] so only results relating to the present study are included here.

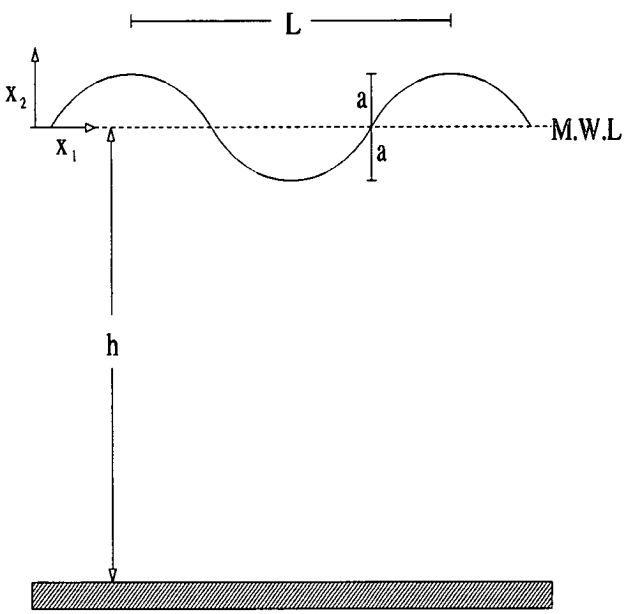

Figure 2.2: Schematic showing sinusoidal wave parameters

The factor most important to this study is the wave induced velocity in the water column beneath it. Using linear theory for simple sinusoidal waves, those used in the study, the horizontal component of this velocity is given as [23]

$$u = \frac{agk}{\omega} \frac{\cosh k(h + x_2)}{\cosh kh} \cos(kx_1 - \omega t) \tag{2.35}$$

and the vertical component as

$$v = \frac{agk}{\omega} \frac{\sinh k(h + x_2)}{\cosh kh} \sin(kx_1 - \omega t) \tag{2.36}$$

where k, the wave number, is given by

$$k = \frac{2\pi}{L} \tag{2.37}$$

and ω, the radian wave frequency, by

$$\omega = \frac{2\pi}{T} \tag{2.38}$$

A further useful theoretical result, the Lagrangian paths traced by particles in the water column under a wave, may also be derived from the equations for the velocities beneath the wave. The horizontal motion is given by [23]

$$x_1(t) = -a\frac{\cosh k(h + x_2)}{\sinh kh}\sin(kx_1 - \omega t) \tag{2.39}$$

and the vertical motion by

$$x_2(t) = a\frac{\sinh k(h + x_2)}{\sinh kh}\cos(kx_1 - \omega t) \tag{2.40}$$

As can be seen in figure 2.3 the effect that the surface waves have on the water column beneath them depends on the dimensionless factor $\frac{h}{L}$ where h is the depth of the water and L is the wavelength of the waves. For values greater than 0.5 a deep water approximation may be used for the above two expressions giving [23]

$$x_1(t) = -ae^{kx_2}\sin(kx_1 - \omega t) \tag{2.41}$$

and

$$x_2(t) = ae^{kx_2}\cos(kx_1 - \omega t) \tag{2.42}$$

Similarly for $\frac{h}{L} < 0.05$ a shallow water approximation may be used [23]

$$x_1(t) = -\frac{a}{kh}\sin(kx_1 - \omega t) \tag{2.43}$$

and

$$x_2(t) = a\left(1 + \frac{x_2}{h}\right)\cos(kx_1 - \omega t) \tag{2.44}$$

Examining the paths traced by the particles, their distance from the origin $r = \sqrt{x_1^2 + x_2^2}$ in the case of the deep water approximation is given by

$$r = ae^{kx_2} \tag{2.45}$$

in the case of intermediate water by

$$r = \frac{a}{\sinh kh}\left[\cosh^2 k\,(x_2+h)\sin^2(kx_1-\omega t) + \sinh^2 k\,(x_2+h)\cos^2(kx_1-\omega t)\right]^{\frac{1}{2}} \tag{2.46}$$

and in the case of the shallow water approximation by

$$r = a\left[\frac{1}{k^2h^2}\sin^2(kx_1-\omega t) + \left(1+\frac{x_2}{h}\right)^2\cos^2(kx_1-\omega t)\right]^{\frac{1}{2}} \tag{2.47}$$

It can be seen that for deep water the particles trace circular orbits with radii that decrease with depth. For both shallow and intermediate water however the orbits are elliptical. While in intermediate water the horizontal distance the particles move through decreases with depth, in shallow water the horizontal movement is independent of depth (fig. 2.3).

It is the intermediate case, where the particles' horizontal movement decreases with depth that is normally encountered at the sites of out-falls [16] and experiments were conducted with $\frac{h}{L} = 0.16$ to reproduce these conditions. The reasons for this precise choice of value are explained in section 2.3 of chapter 4, 'Wave design'.

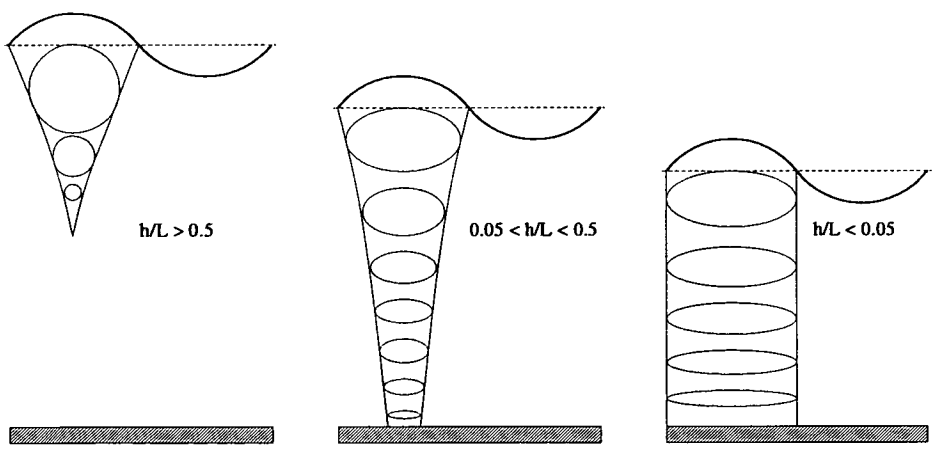

Figure 2.3: Effect of waves on water column

2.5 Wave interaction

The inclusion of waves into the buoyant jet problem requires the introduction of a third characteristic length scale related to the influence of the waves on the discharge. Following Chin [16] this is defined as z_M, a ratio of the initial momentum flux of the discharge to the maximum horizontal wave induced velocity at the port u_{max}.

$$z_M = \frac{M^{1/2}}{u_{max}} \tag{2.48}$$

where, from equation 2.35, u_{max} is given by

$$u_{max} = \frac{agk}{\omega \cosh kh} \tag{2.49}$$

The dimensionless parameter $\frac{l_Q}{z_M}$, numerically equal to the ratio of the maximum horizontal wave induced velocity at the port to the port velocity, then gives a measure of the wave effect at the port. This study looked at values of $\frac{L_Q}{Z_M}$ in the range of 5.1×10^{-2} to 9.5×10^{-2} constrained by the tank dimensions and wave paddle, but of the order of real outflows [16].

Chapter 3

Experimental Techniques

3.1 Summary

This chapter describes the two measurement techniques used in the study, Particle Image Velocimetry (PIV) and Laser Induced Fluorescence (LIF). Both of these are optical techniques and require the flow to be illuminated. As the method of illumination used for both techniques is similar, a description of the illumination method is presented first.

3.2 Flow illumination

Both measurement techniques used required that the full area of a thin slice through the plume be illuminated. PIV has the further requirements that the period of illumination be short enough that the particles do not move significantly while illuminated, resulting in a streaked image and also that they scatter sufficient light to be recorded. As the particles in question are often very small, an intense light source is required. The LIF experiments also required a light source at the correct wavelength to excite a fluorescent dye. Laser illumination is eminently suited to all these tasks as it is both intense and at a precise wavelength. The small divergence shown by a laser beam is also useful in producing a thin

light sheet. Where the period of illumination needs to be very small, for example with very fast flows, it is often necessary to use pulsed lasers, the beam being expanded to a sheet by optical methods. However for the maximum flow speed encountered in this study, just over $1.2ms^{-1}$, it was possible to use a continuous wave laser [25]. Used in conjunction with a scanning beam box a thin, pseudo light sheet large enough to illuminate the whole flow could be produced.

3.2.1 The scanning beam system

The scanning beam system developed at Edinburgh University [26] produces a pseudo light sheet by reflecting the laser beam first onto a spinning octagonal mirror and then onto a second, parabolic mirror. As the rotating mirror is placed at the focus of the parabolic mirror, the beam will always be reflected vertically upwards by the second mirror. This produces the pseudo light sheet (fig. 3.1). The period of illumination of a particle in the sheet, an important factor for the PIV experiments, will be governed by the scan rate of the beam and therefore the rotation rate of the octagonal mirror.

If the beam path between the laser and the scanning beam box is long the divergence of the laser beam, though small, over a large distance may result in a thick sheet being produced. This can be overcome by means of collimating optics to narrow the beam prior to reflection from the octagonal mirror. The argon-ion laser used however, having a beam aperture of 0.79mm and a divergence, θ, of 0.56mrad, produced a beam with a diameter of 0.89mm at the scanning beam box in the purple tank and 0.90mm at that in the red tank. Further collimation was therefore unnecessary.

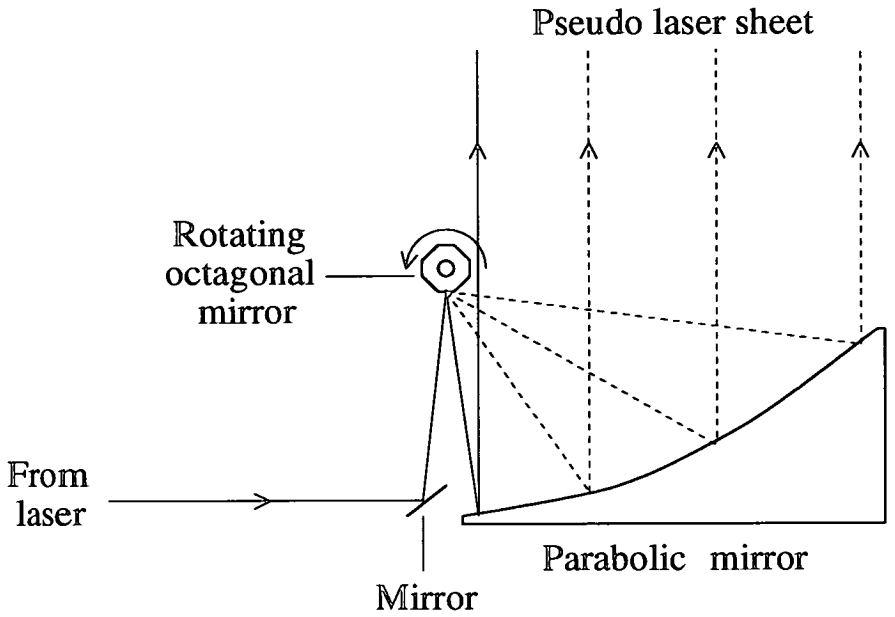

Figure 3.1: Scanning beam box laser sheet optics

3.3 Laser induced fluorescence

As mentioned in chapter 1, laser induced fluorescence is a non-intrusive optical technique that can produce a concentration map for the full flow field. The process central to the technique is that of fluorescence.

A photon colliding with an atom can either be absorbed or scattered. The chance of absorption will be highest if the photon's energy matches that of one of the atom's excitation energies. If such a photon is absorbed then the energy is transferred to one of the atom's electrons leaving it in an excited state. This however is not a stable state for the atom and it can dissipate the energy by means of emitting another photon of the same frequency as the first. If the atom though is not isolated, as in a gas, but surrounded by others, as in a liquid or solid, then this energy can also be dissipated by means of intermolecular collisions. These collisions will result in the emission of photons at a range of frequencies and if within the visible range, the material will be seen to glow. If this process occurs quickly, that is within less than 10^{-7}seconds then the material is said to fluoresce.

The same process may also occur over a longer time period than this, in which case it is known as phosphorescence [27].

Fluorescence can be used to measure concentration by dissolving a fluorescent dye into the liquid to be studied. When illuminated by the correct frequency light the intensity of the fluorescence will be proportional to the concentration of the dye and therefore of the liquid under study [28].

3.4 Development of the LIF technique

3.4.1 Illumination

The flow illumination systems developed previously in the group for use with PIV give an intense, thin, mono-chromatic light sheet that can cover a large measurement region. As previously stated this is exactly the type of illumination that is also required for LIF measurements and it was therefore decided to use the laser systems already in place for the present study.

The lasers used within the fluids group at Edinburgh are of the Argon-ion type (λ=514.5nm and 488nm) and therefore a dye that fluoresces when illuminated by light at one of these wavelengths was required. Snavely [29] shows that the organic dye Rhodamine B ($C_{28}H_{31}N_2O_3Cl$)(fig. 3.3) when dissolved in water will fluoresce orange-red when illuminated by the blue-green light of an Argon-ion laser (λ=514.5nm). However the dye was initially to be dissolved in pure methanol and Drexhage [30] shows that the wavelength of both absorption maximum and fluorescence of the dye will vary, dependent on the solvent in which it is dissolved. If the absorption maxima of the dye were to shift dependent on the concentration of the plume, then this may lead to a change in intensity of the fluorescent light. This problem is compounded by the fact that the dye's fluorescent efficiency is also dependent on the dissolving solvent. However if calibration images were taken using known concentrations of plume solution, methanol plus

dye, diluted with fresh water then these factors would be taken into account.

3.4.2 Calibration

Calibration using known intensities of dye is also necessary in order to convert images of the plume into concentration maps. A technique to produce such calibration images therefore needed to be developed.

While ideally the entire area of the tank covered by the light sheet would require filling with known concentrations of dye, this would in practical terms mean filling the whole tank. Given the dimensions of the tanks to be used for the experiments this was not practical in either terms of time or the amount of dye that would be required. To make the calibration process more efficient a smaller calibration tank was built. This tank could be filled with dye of a known concentration and then suspended in the light sheet allowing calibration images to be quickly taken (fig. 3.2).

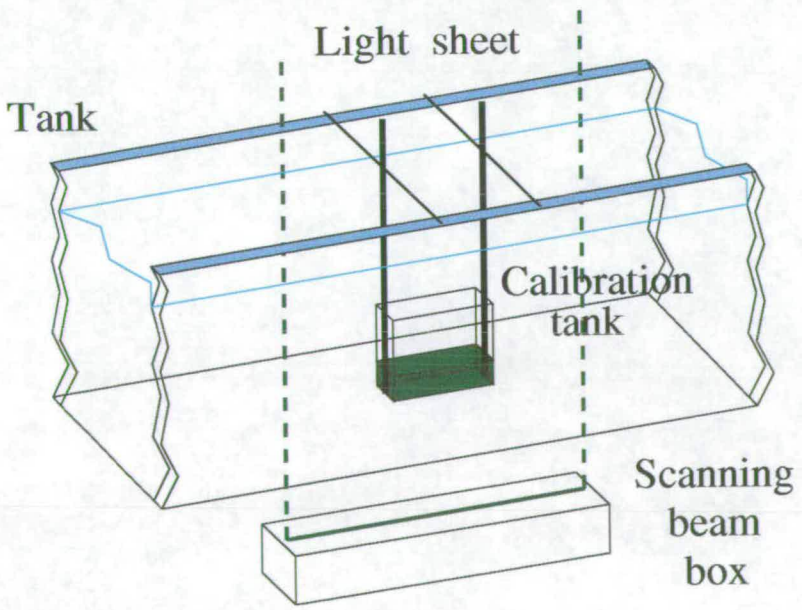

Figure 3.2: Diagram showing calibration tank in position for taking calibration image

Add	11ml	to give	4.50% conc
Add	14ml	to give	4.00% conc
Add	18ml	to give	3.50% conc
Add	24ml	to give	3.00% conc
Add	33ml	to give	2.50% conc
Add	22ml	to give	2.25% conc
Add	28ml	to give	2.00% conc
Add	36ml	to give	1.75% conc
Add	48ml	to give	1.50% conc
Add	67ml	to give	1.25% conc
Add	100ml	to give	1.00% conc
Add	167ml	to give	0.75% conc
Add	333ml	to give	0.50% conc
	Discard	500ml	
Add	500ml	to give	0.25% conc

Table 3.1: Calibration run concentration values

Initial experiments showed that the plume soon became highly diluted especially in the regions of interest at the edges of the plume. It was found therefore only to be necessary to conduct calibration measurements at low concentrations, that is less than around three percent concentration. Trial and error also showed that initially it was possible to distinguish only between concentrations no less than 0.25% apart and so calibration readings were taken at these intervals from 2.5% down to 0.25%. Readings were also taken at 0.5% intervals between 2.5% and 5.0% so that coarser measurements could be made in the core of the plume without greatly extending the length of a calibration run.

To perform a calibration run 50ml of neat plume solution were added to 450ml of clean water, mixed and then 450ml discarded. This gave 50ml of ten percent concentration solution. Adding a further 50ml of fresh water then produced a five percent solution which could be added to the calibration tank and the first calibration image taken. Further quantities of fresh water were then added to the calibration tank to give the concentrations shown in table 3.1. At each addition of fresh fluid the calibration tank was well stirred and a calibration image taken.

If the plume were to be directly imaged, then the intensity of the plume would be a combination of the background laser light and the fluorescent intensity of the plume. To prevent the intensity of the laser light swamping low levels of fluorescent intensity the background laser light can be filtered out allowing only an image of the orange fluorescent light to be recorded. This was achieved using a pair of laser safety goggles, designed to absorb the wavelength of light emitted by the laser, placed in front of the camera lens.

In order to utilise the calibration images and convert the images of the fluorescing plume into concentration maps computer software had to be developed. This software also allowed for imperfections in the laser light sheet to be corrected. Further details of the analysis software are given in chapter 6.

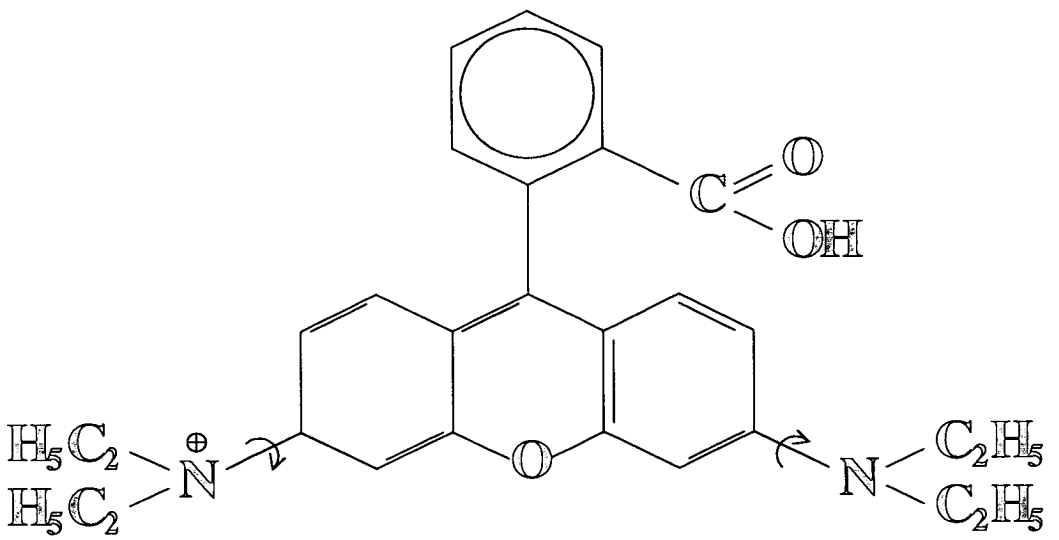

Figure 3.3: Chemical structure of Rhodamine B

3.5 Particle image velocimetry

Particle image velocimetry is also a non-intrusive, optical measuring technique but one that can provide velocity information about the flow. The principle of the technique is based on recording images of small particles, either naturally

present or seeded into the flow, at small time intervals apart. As the particles' displacement can be found from analysis of the successive images and the time interval between images is known, the particles' velocity may be calculated. If the particles have been correctly chosen then the velocity of the particles in a region of the fluid will also be equal to that of the liquid in the same region. As the seeding particles are dispersed throughout the flow, it is therefore possible to gather velocity information over the full flow field.

The technique is now widely used with commercial systems available to measure a diverse range of flows, both gaseous and liquid. A large increase in use is mainly due to the advent of CCD devices to record images, allowing much faster processing than was previously possible with systems using wet film photographic techniques.

The following sections provide only sufficient background for an understanding of how the PIV technique has been used in the present experiments, for a comprehensive guide to the subject the reader is directed to Raffel et al [25] and also Melling's detailed study on tracer particles and seeding for PIV [31].

3.5.1 Fluid mechanical properties of seeding particles

Possibly the most important property of a seeding particle is that it will faithfully follow the flow under study and not perturb it in any way. Therefore an understanding of the particles' fluid mechanical properties is very important in choosing seeding particles. There are three main factors that will govern whether a particle will follow the flow; inertial effects, gravity and the spatial averaging of turbulence [32].

If there is a difference in density between the seeding particles and the fluid under study then there may be a delayed response of the particle to any acceleration of the fluid. This however will only be significant if the density difference is large

or there are high frequency fluctuations in the fluid flow [32].

As well as accelerations of the fluid, the particles may also drift due to the acceleration of gravity. For small particles the drift due to gravity may be defined as

$$V_v = \frac{d_p^2 g}{18\mu_o}(\rho_p - \rho_o) \tag{3.1}$$

where d_p is the particle diameter, μ_o fluid viscosity and ρ_p and ρ_0 the particle and fluid densities respectively [32].

Finally the particles must be small enough that no spatial averaging takes place due to the particle diameter being larger than the dimensions of eddies in the fluid.

3.5.2 Light Scattering behaviour of particles

As well as faithfully following the fluid flow the seeding particles must also scatter sufficient of the illuminating light that their position can be recorded. The particles used in PIV for seeding are normally spherical and their diameters larger than the wavelength of the illuminating light. Their light scattering properties may therefore be predicted by Mie scattering theory [33]. This states that if a particle's normalised diameter q, given by

$$q = \frac{\pi d_p}{\lambda} \tag{3.2}$$

where d_p is the particles diameter and λ the wavelength of the illuminating light, is greater than unity, then approximately q local scattering maxima will appear between the scattering angles of 0-180 degrees. The average scattered intensity will then increase approximately with q^2.

While it can be seen that for better scattering a large particle diameter is required, as shown in the previous section, this may have an adverse effect in the particle's ability to follow the flow. The diameter of the particles is also important as

analysis of the PIV technique has shown that error in velocity measurements is strongly dependent on particle image diameter [25]. The smaller the image diameter the lower will be any uncertainty in finding the centre of the peak and the sharper the images, the higher the particles' image intensity.

The particle image size can be found by considering the image formed from a distant point source. This image will not appear as a point in the image plane but will form a Fraunhoffer diffraction pattern, even if imaged by a perfectly aberration-free lens [34]. The diffraction pattern takes the form of a circular pattern known as an Airy disk and the diameter of this disk, d_{diff}, represents the smallest particle image that can be obtained for a given imaging configuration. For a point source d_{diff} is defined as

$$d_{diff} = 2.44 f_{\#}(M + 1)\lambda \tag{3.3}$$

where $f_{\#}$ is the f-number and M the magnification of the lens system being used.

In practice however, unless very small seeding particles are being used with a very low magnification lens system, it is unlikely that the particles can be regarded as point sources. As particle size increases, the influence of geometric imaging becomes more and more important. For an image of a particle with finite diameter, the size is given by a convolution of the lens's point spread function (PSF) with the geometric image of the particle. If any aberration of the lens is neglected the PSF may be approximated by the Airy function and the image size given by [25]

$$d_\tau = \sqrt{(M d_p)^2 + d_{diff}^2} \tag{3.4}$$

For the current application $M << 1$, the smallest $f_{\#}$ possible 1.6 and the wavelength of the illuminating laser light $514.5 \text{x} 10^{-9}$. Therefore the smallest image size possible, assuming a point source will be

$$d_{diff} = 2\mu m \tag{3.5}$$

3.5.3 Seeding density

It is not only the seeding particle size however that must be chosen carefully, the seeding density too is an important practical consideration in performing PIV experiments.

If the seeding density is low, that is images of individual particles can be detected and the same particle identified on successive images, then particle tracking velocimetry (PTV) analysis algorithms are used as opposed to PIV. As velocities can only be found where there are particles to measure, a low seeding density may also result in the loss of information from some areas of the flow.

PIV analysis is best used when there is a medium seeding density, that is individual particles can still be detected in images, but it is no longer possible to identify the same particle in a successive image. Here rather than a tracking algorithm, a statistical approach must be used.

If the seeding density however is too high, individual particles may start to overlap and a speckle pattern will be seen. Again statistical methods may be used to obtain velocity information from these images. This is what is done in laser speckle velocimetry (LSV). The high particle concentration may however begin to perturb the flow.

As well as a medium particle density, PIV works best when there is a homogeneous distribution of particles. In this way velocity information may be found from all regions of the images under analysis.

3.5.4 Illumination

As mentioned in the general discussion of flow illumination at the beginning of this chapter, the PIV technique requires illumination that fulfills a number of requirements: the illumination period must be short enough that particles do

not form streaks on the image; and the particles also need to be illuminated twice, with a short delay in between. This time delay must be long enough that the particles' displacements may be found with sufficient resolution, but also short enough to avoid out of plane particles entering the interrogation area, or particles in the plane leaving it. The minimum time delay possible between images using a scanning beam system is the time period of the scan, the particle being illuminated on consecutive scans. Longer time delays may be achieved using a delay between exposures of the camera.

3.5.5 Imaging of the flow

The first PIV systems made use of wet film photography to record images of the seeding particles in the flow field but advances in electronic imaging have given rise to a more convenient recording medium. Electronic recording has the advantage of immediate image availability and provides the images in a form that may be readily processed by computer.

The most common method of recording images electronically is by means of a charge coupled device (CCD). CCDs are small, of the order of $10 \times 10 \mu m^2$, solid state devices that convert light to an electrical signal. CCD sensors are usually arranged into an array with each of the individual sensors being known as a *pic*ture *el*ement or pixel. Typical, commercially available arrays are of the order of hundreds or thousands of pixels square. Like any electronic device CCDs are susceptible to electronic noise and as the amount of light scattered from a tracer particle may well be small, this must be minimised. A major source of noise in CCD sensors is the generation of a current from the device due to thermal effects. Noise of this type may be reduced by cooling the array and though this was once an expensive solution, electrically cooled cameras are now increasingly available.

As well as the recording medium, the method of recording PIV images is also important. Though many variations exist on each, two inherently different types

of recording are used: single frame/multiple exposure and multiple frame/single exposure. With single frame/multiple exposure methods, successive recordings of the flow are made onto the same image, while for multiple frame/single exposure, only one image is ever recorded per frame, the successive image being exposed onto the following frame. Figure 3.4 shows a synthetic single frame/double exposure image while figure 3.5 shows the same two exposures but on two separate frames. As can be seen from the two separate images, between exposures the particles were shifted down and to the right.

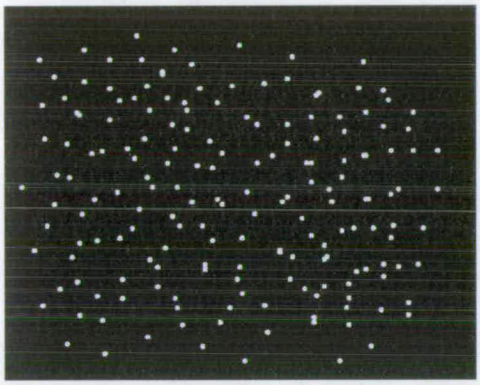

Figure 3.4: Synthetic single frame/double exposure PIV image

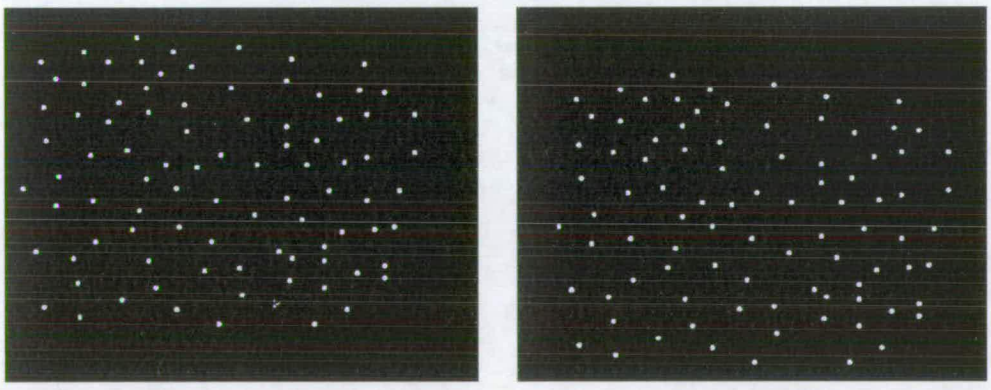

Figure 3.5: Synthetic double frame/single exposure PIV images

As short time intervals are normally required between exposures, the physical difficulty of winding-on the film in the required time led to the single frame/multiple

exposure method often being the only option for use with wet film photography. This method however has the major drawback that, without additional information, it cannot be determined which of the exposures preceded the other. When processing the image this may lead to directional ambiguity in the calculated velocity vector. To overcome this difficulty a number of solutions were proposed, with many investigators using an image shifting technique [25]. By adding a constant, known shift between exposures all particle displacements are constrained to be positive and the directional ambiguity removed. The known shift could then be removed from the calculated velocity vector to give the true result.

The advent of widely available CCD cameras able to take successive exposures within a short time interval has meant that multiple frame/single exposure methods, which do not suffer from temporal ambiguity, can now be more widely used. This has removed the necessity for incorporating apparatus solely to overcome temporal ambiguity and greatly simplified PIV systems.

3.5.6 Processing of PIV images

As mentioned in section 3.5.3, individual particles cannot normally be identified on PIV images and statistical methods are therefore used to evaluate them. Detailed descriptions of the mathematical background behind the processing are given by Adrian [35, 36] and Westerweel [37] so only an overview is presented here.

In order to process a PIV image it is first broken down into a number of smaller interrogation regions. As each of these of regions will provide one velocity measurement, the spatial resolution of the resultant velocity map will be increased for decreasing interrogation area. Decreasing the interrogation area size will however reduce the number of particles with which the analysis is being made and this may reduce the accuracy of the individual measured velocities.

In order to find the displacement of the particles within the interrogation area a type of pattern matching is used. Using as an example two successive images produced using a multiple image/single exposure method, one image is essentially shifted over the other until the greatest match between the images is found. The displacement between the two images will then be equal to the displacement of the particles between the two images. This method is known as cross-correlation [38].

Mathematically, the cross-correlation function R of two functions f and g each with arrays of size ixj is defined as

$$R_{fg}(i,j) = f(i,j) \otimes g(i,j) = \int_{-\infty}^{\infty} \int_{-\infty}^{\infty} f^*(\alpha,\beta) g(i+\alpha, j+\beta) d\alpha d\beta \qquad (3.6)$$

where α and β are dummy variables. However in PIV analysis this function is only calculated over a finite interrogation area and can therefore be rewritten as

$$R_{fg}(i,j) = \frac{1}{MN} \sum_{m=0}^{M-1} \sum_{n=0}^{N-1} f^*(i,j) g(i+m, j+n) \qquad (3.7)$$

Using as functions two successive images of the flow at each shift the sum of all the overlapping pixel intensities will be calculated producing the cross-correlation value for that point. Where the number of overlapping particle images is high, the correlation value for that position will also be high resulting in a peak in the correlation function. This value can then be used as an estimate of the particle image displacement. It is important to remember that this technique will only recover from the pairs of interrogation regions the average linear shift of the particles within the area. This places another constriction on the interrogation area size in that it must be small enough such that second order effects, for example displacement gradients, can be neglected. Figure 3.6 shows the cross-correlation function for the synthetic images shown in figure 3.5 calculated using TedPIV PIV analysis software [39]. The position of the strong correlation peak shows clearly that the particles have been displaced down and to the right between the two exposures. While the cross-correlation method may be applied to multiple

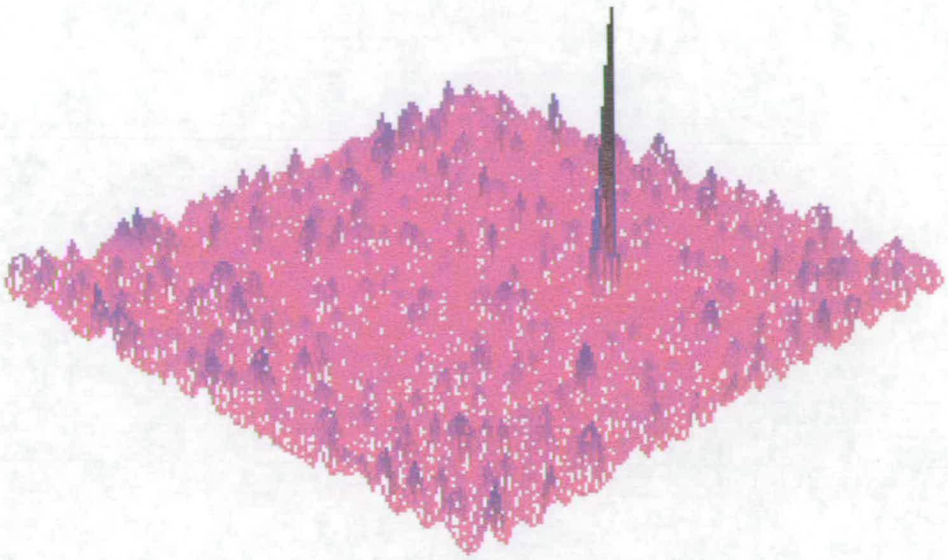

Figure 3.6: Cross-correlation function of two successive PIV images

frame/single exposure images, it cannot be used for single frame/multiple exposure images. In order to evaluate these images auto-correlation must be used. Instead of the correlation being found between two images, the image is correlated with itself

$$f(i,j) \circ f(i,j) = \frac{1}{MN} \sum_{m=0}^{M-1} \sum_{n=0}^{N-1} f^*(i,j) f(i+m, j+n) \tag{3.8}$$

The auto-correlation function, figure 3.7, of the single image shown in figure 3.4, again calculated using TedPIV, shows three distinct peaks as opposed to the single peak of the cross-correlation function. The large, central, self-correlation peak is due to the image matching itself exactly. The two smaller peaks correspond to the correlation of the images of the particles from the first exposure with the images from the second exposure and vice versa. Once again a correlation peak correctly shows the displacement of the particles down and to the right, but the second peak also shows a displacement up and to the left. This again highlights the directional ambiguity of the single frame/double exposure method. The displacement peaks are also of lower amplitude than that of the displacement peak gained from cross-

correlation. It is therefore necessary to have lower noise levels in images to be processed by auto-correlation than those required for cross-correlation.

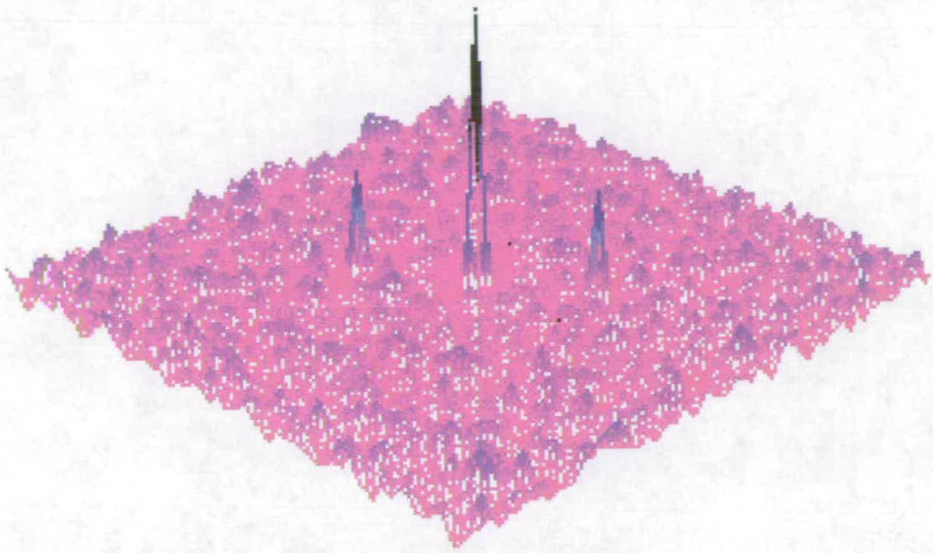

Figure 3.7: Auto-correlation function of a double exposure PIV image

If the correlation function were to be calculated directly using equation 3.7 then it can be seen that the number of calculations required will be proportional to the image size. Indeed there is a quadratic increase between the number of multiplications to be calculated and the sample size. Given that typical PIV interrogation area sizes may be of the order of thousands of pixels, the computational effort required to directly calculate the correlation function may be very large. However if use is made of the correlation theorem and a Fast Fourier Transform (FFT) algorithm, this effort may be significantly reduced. The correlation theorem states that the cross-correlation of two functions is equivalent to a complex conjugate multiplication of their Fourier transforms:

$$f(x,y) \otimes g(x,y) \leftrightarrow F^*(u,v)G(u,v) \tag{3.9}$$

The use of the correlation theorem still requires $O[N^4]$ calculations to be performed, where N is the width in pixels of the interrogation area, but this number

interrogation area must be increased. The prevention of aliasing places a further criterion on the choice of interrogation region size.

The Nyquist theorem must be borne in mind not only when considering the interrogation region size, but also in determining the shift of the interrogation region across the image [40]. Given an interrogation region width of N the highest spatial frequency that can be measured will be

$$f = \frac{1}{N} \tag{3.10}$$

as any frequencies higher than this will essentially be averaged out. Recalling the Nyquist theorem, to correctly record this frequency, f the image must be sampled at twice this frequency, $2f$. The shift between interrogation regions can then be calculated as

$$shift = \frac{1}{2f} = \frac{N}{2} \tag{3.11}$$

Therefore in order to correctly sample the image there should be a 50% overlap between successive interrogation regions. For example if a 32x32 pixel interrogation region is being used then the interrogation should be shifted across the image by 16 pixels at a time. This will result in a grid of velocity vectors spaced 16 pixels apart.

3.5.7 PIV processing summary

While the previous sections have covered the analysis of PIV images in sufficient detail to show how velocity measurements may be obtained from the images, it is by no means a complete description of the process. Other problems associated with the use of FFTs in the calculation of the cross-correlation also exist and while the procedure calculating the particles' displacement has been outlined, further techniques exist to increase the accuracy of the calculation. For a fuller description of PIV processing and post-processing the reader is again directed to Raffel et al [25].

Chapter 4

Line plume experiments

4.1 Summary

In this chapter the design criteria for the line plume experiments are discussed and the resulting experimental apparatus described. The experimental method is then given. Finally the experimental conditions for each of the experimental runs are shown.

4.2 Experimental Design

4.2.1 Discharge properties

In order to realistically model the plumes produced by outfall pipes, the discharged solution had to fulfill a number of criteria; it had to be less dense than the receiving fluid so as to be buoyant, it had to have a similar viscosity to the receiving fluid to allow the Reynolds number at the port to be such that the plume was turbulent and it also had to be transparent and miscible in the receiving fluid.

Cost and ease of filling the tank dictated using tap water as the receiving fluid and therefore a fluid less dense than, miscible in and transparent in water needed

to be found. Initially it was thought that an ethanol/water solution would fulfill these criteria and to investigate the necessary discharge parameters the Froude number equation (eq. 2.13) was substituted into the Reynolds number equation (eq. 2.11) to yield an equation for the port diameter, d, required for a discharge of given Froude and Reynolds numbers

$$d = \left(\frac{R\nu_o}{F g_o^{\frac{1}{2}}} \right)^{\frac{2}{3}} \tag{4.1}$$

This equation was then substituted into equation 2.13 to find the term for the required port discharge velocity

$$v_o = (R\nu_o)^{\frac{1}{3}} \left(F g_o^{\frac{1}{2}} \right)^{\frac{2}{3}} \tag{4.2}$$

From the above two equations it was then possible to find expressions for the total discharge, D_T and discharge of ethanol, D_E required, the latter being plotted so that the most economical as well as practical solution could be found

$$D_T = v_o \pi \left(\frac{D^2}{4} \right) \tag{4.3}$$

$$D_E = \left(\frac{P_E}{100} \right) D_T \tag{4.4}$$

where P_E is the percentage by weight of ethanol. These give the discharge rate per port and must be multiplied by the total number of ports for the total discharge rate.

Despite pure ethanol having a similar viscosity to water, when the two are mixed the viscosity can substantially increase (fig. 4.1); the density of the mixture will also not be constant (fig. 4.2)[41]. To see the effect of these changes on discharge parameter equations 4.1-4.4 were plotted for ethanol discharged with a Froude number of 14. This value of Froude number was chosen as one being

similar to that of actual outfalls. It can be seen from the graphs, figures 4.3-4.6, that the use of ethanol in producing a turbulent discharge would require a total discharge rate of at least 10 l/min. Not only would pumping fluid at this rate require an expensive pump, but also it would involve the use of a large volume of ethanol which would both be expensive and also potentially hazardous due to its flammable nature. It was therefore decided to see if a similar solution, but with a lower viscosity could be found.

Methanol having very similar properties to ethanol, but a lower viscosity also looked a good candidate. Even though the viscosity of a methanol/water solution changes in a similar way to an ethanol/water mix (figs. 4.7 and 4.8), the combined viscosity is not as high [42, 43]. As for ethanol, graphs were plotted of equations 4.1 to 4.4 showing the port diameter, port velocity and discharge rates for a Froude number of 14 and a range of Reynolds numbers (figs. 4.9-4.12).

For the practical and economic reasons stated above, ideally a plume solution needs to be found such that a Reynolds number greater than 4000 can be achieved with both a low total discharge rate and also a low methanol discharge rate. From graphs 4.11 and 4.12 it can be seen that this condition is met at both very high methanol concentration, 100 percent, and very low concentration, 10 percent. However, at low concentration the total discharge rate is much higher than for a high methanol concentration. As it seemed that both storing and pumping the volume of liquid required for a rate of 3 litres per minute was more desirable than that required for a discharge of around 20 litres per minute, it was decided to use a plume solution of pure methanol. Equations 4.1-4.4 were then replotted against Reynolds number for a solution of pure methanol, discharged with a Froude number of 14 (figs. 4.13-4.15).

Using figure 4.13 a port diameter of 2.7mm was chosen as this gives a discharge with a Reynolds number greater than 4000 and therefore a turbulent plume, the appropriate discharge rate could then be found from figure 4.14. As a discharge

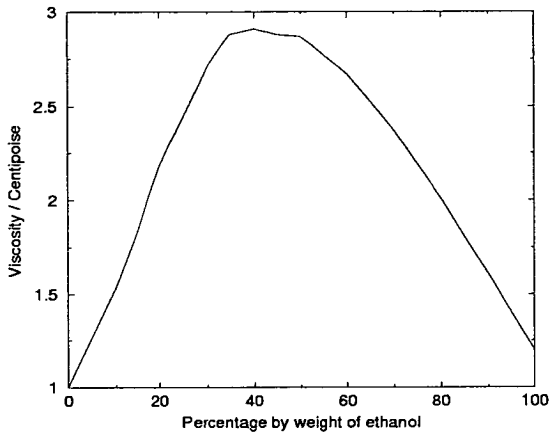

Figure 4.1: Graph of μ_o against P_E.

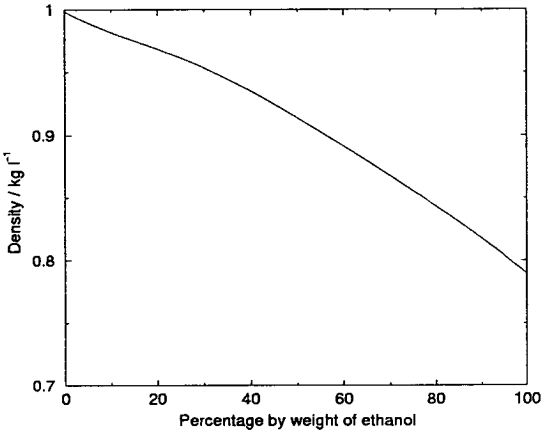

Figure 4.2: Graph of ρ_o against P_E.

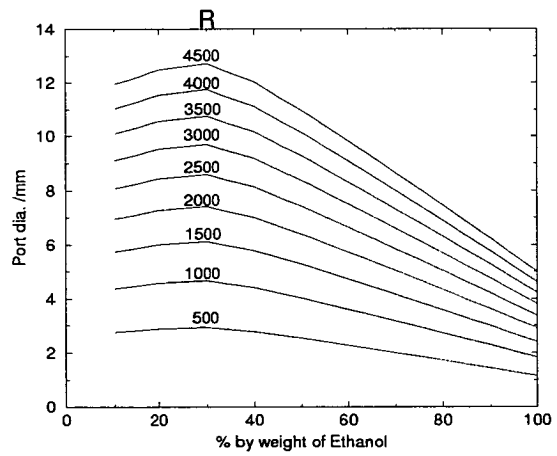

Figure 4.3: Graph of d against P_E, F=14.

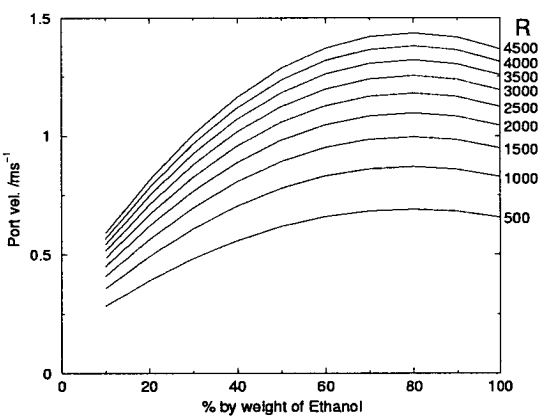

Figure 4.4: Graph of v_o against P_E,F=14.

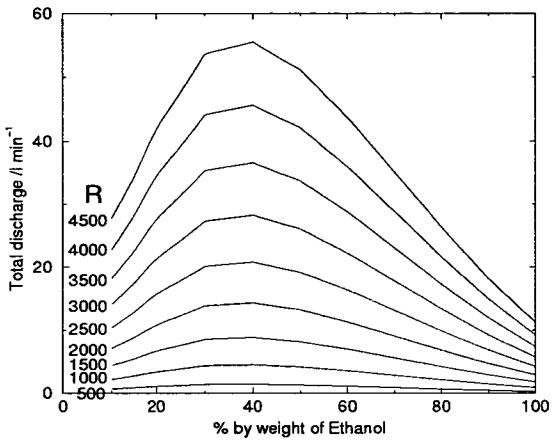

Figure 4.5: Graph of D_T against P_E, F=14.

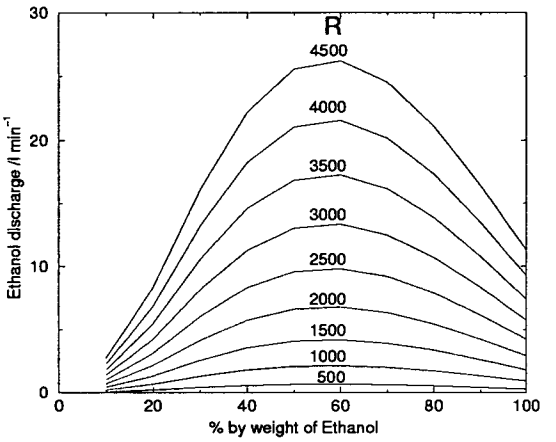

Figure 4.6: Graph of D_M against P_E, F=14.

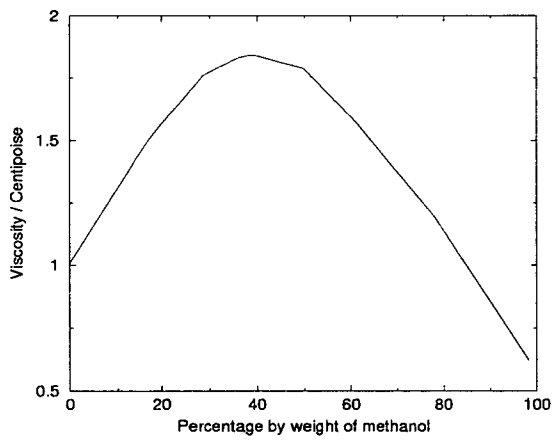

Figure 4.7: Graph of μ_o against P_M.

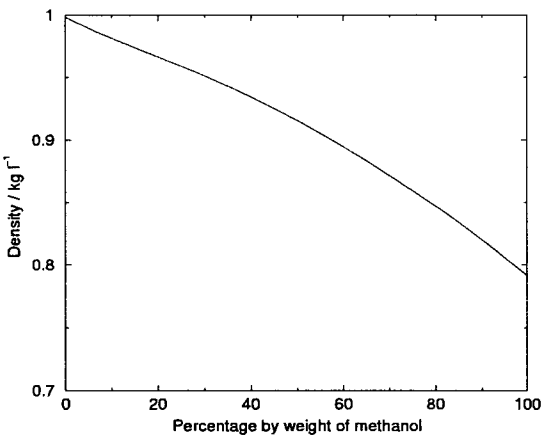

Figure 4.8: Graph of ρ_o against P_M.

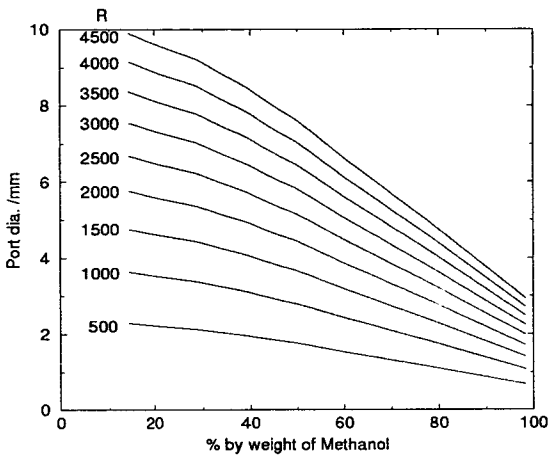

Figure 4.9: Graph of d against P_E, F=14.

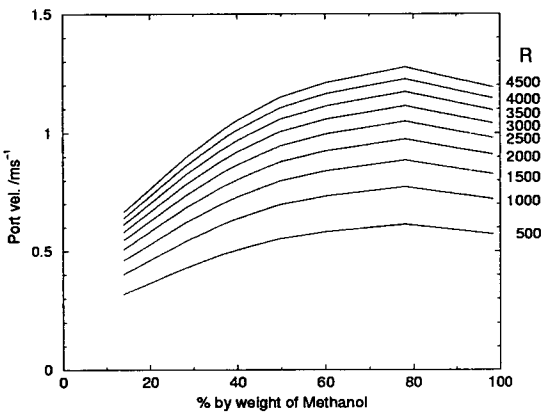

Figure 4.10: Graph of v_o against P_E,F=14.

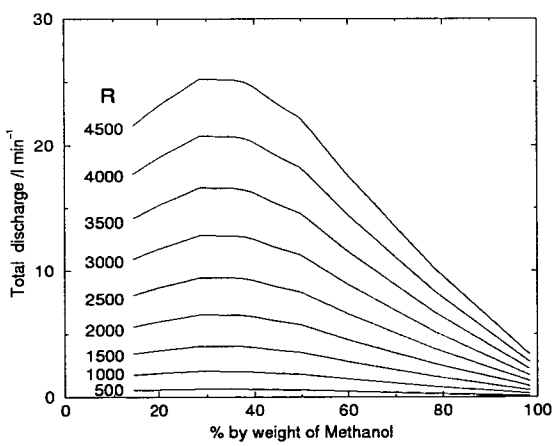

Figure 4.11: Graph of D_T against P_E, F=14.

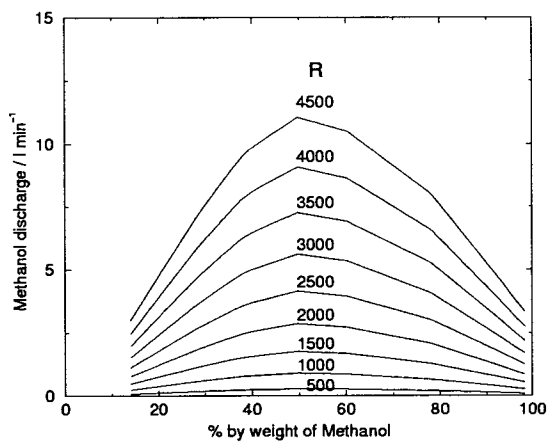

Figure 4.12: Graph of D_M against P_E, F=14.

rate of nearly 3 litres per minute could not be practically achieved using gravity feed alone it was decided to include a pump in the apparatus. For future flexibility, it was decided to obtain a variable rate pump to allow a wider range of flow rates to be achieved should this prove necessary.

The flow rate was to be monitored using a glass, float type flow meter installed between the discharge reservoir and the diffuser. As this type of flow meter has to be calibrated for the specific liquid being measured and was calibrated for water, it had to be recalibrated for methanol. This was done by pumping known volumes of methanol through the meter and recording both the time taken and the flow rate reading. A calibration graph could then be plotted, figure 4.16, and used to calculate the actual methanol flow rate.

4.2.2 Diffuser design

It was intended to model the discharge of a multi-port diffuser, similar to a realistic outfall in which the plumes from individual ports merge quickly to form a single line plume [1]. The discharge was pumped through a model diffuser with seven, evenly spaced, horizontally orientated ports along its length. The port diameter had been determined from the calculations described previously and were positioned so that discharge from the two end ports, reflected from the tank walls could be regarded as discharge from virtual ports spaced with the same port spacing, further along the diffuser (fig. 4.18). To ensure that ports at the far end of the diffuser gave the same discharge as ports at the near end, it was necessary to make sure that the diffuser pipe ran full. Fischer et al. [2] found that the best ratio of total port area to pipe area lay between $\frac{1}{3}$ and $\frac{2}{3}$. Increasing the ratio above this may lead to the pipe not running full and a ratio below this may lead to an increase in the pressure required to pump the effluent out. While the latter consideration may be vital for a real outfall, in the present situation the pump available had a pumping range greatly exceeding that necessary to maintain

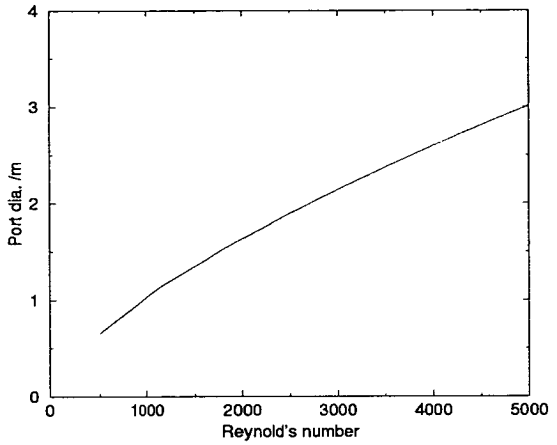

Figure 4.13: Graph of d against R, F=14, P_M=100.

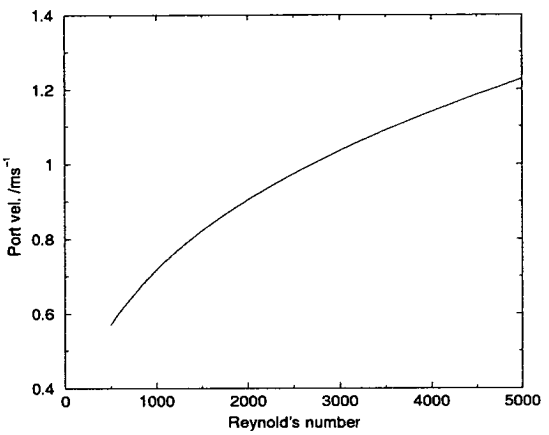

Figure 4.14: Graph of v_o against R, F=14, P_M=100.

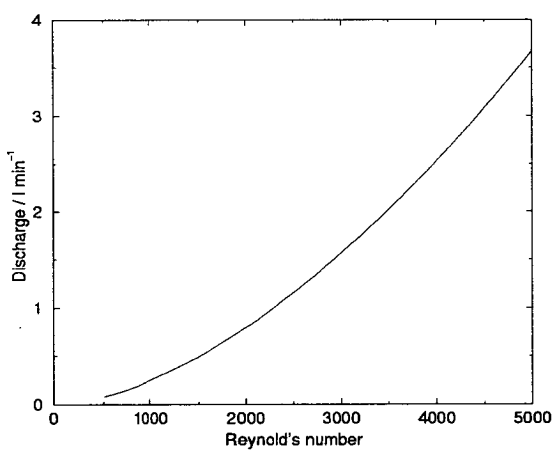

Figure 4.15: Graph of D_T against R, F=14, P_M=100.

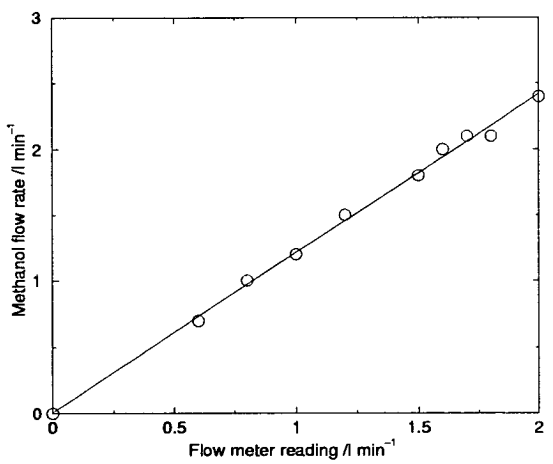

Figure 4.16: Flow meter calibration graph.

enough pressure in the outfall. Therefore only the first of these considerations needed to be born in mind. Half inch diameter copper pipe was used as this is a commonly available diameter and would prove convenient for plumbing to other parts of the apparatus. The total port area was a thirtieth of the cross sectional area ensuring the pipe would run full.

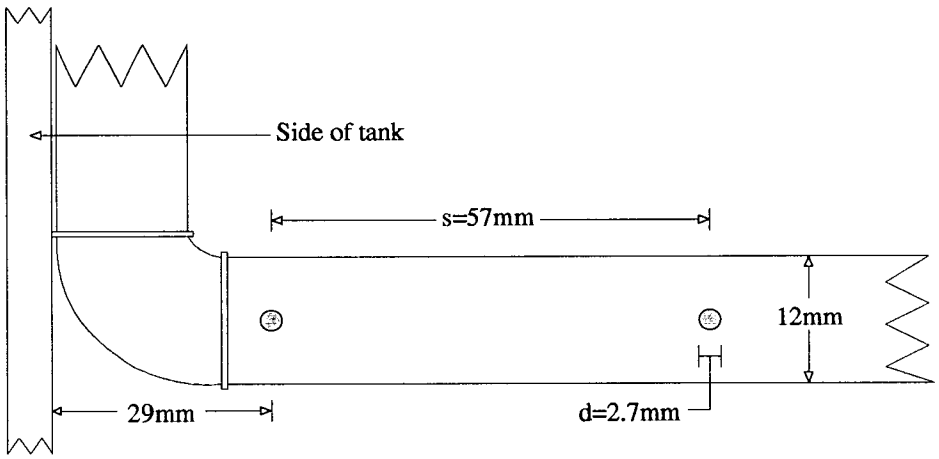

Figure 4.17: Section of the model diffuser used for line plume experiments.

4.2.3 Wave design

The computer controlled wave maker available was able to produce sinusoidal waves with a range of amplitudes and wavelengths. In order that the waves produced would be continuous, a 'beach' of plastic foam was placed at the opposite end of the tank to absorb the waves produced and minimise any reflection. As previously mentioned in chapter 2, to produce movement in the water below the waves similar to that found at actual outflows, the ratio $\frac{h}{L}$ must have a value between 0.05 and 0.5. Given the fixed depth of the tank of 0.7m, to be realistic the waves would require a wavelength of between 1.4m and 14.0m. Also to create a realistic wave effect at the port, the longer the wavelength the better (eq. 2.49). Experimentation with the wave maker found that the longest wavelength wave that could be produced was 4.3m and this was the value chosen. Using the fixed

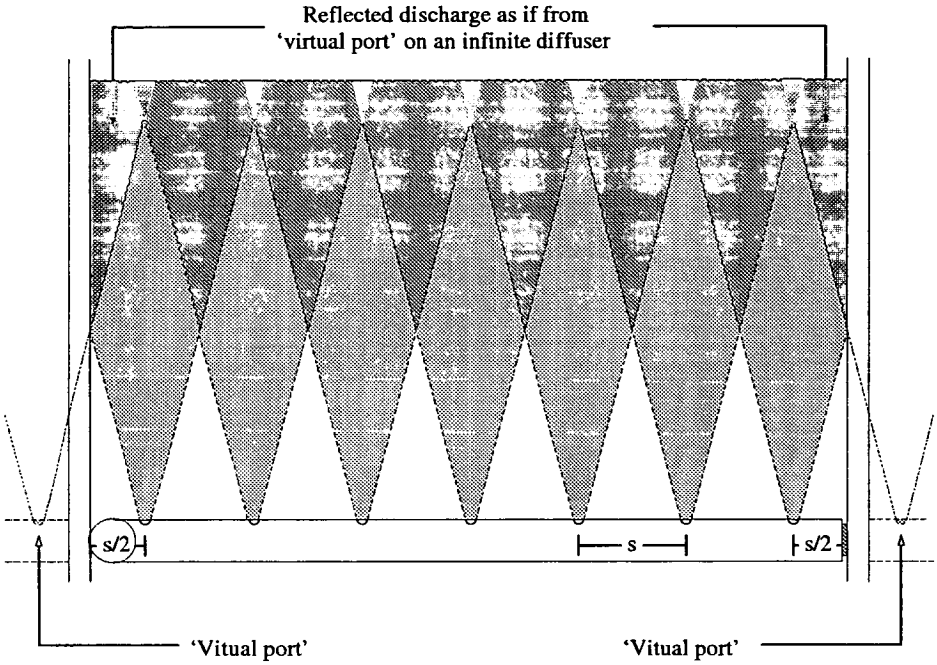

Figure 4.18: Diagram showing reflected discharge from tank walls as though from 'virtual' ports further along an infinite diffuser.

depth of the tank for h and 4.3m for L the ratio of $\frac{h}{L}$ for these experiments will therefore be 0.16, giving both realistic wave conditions and a realistic wave effect at the port.

As described in chapter 2, the extent of the effect of the wave at the port is given by the dimensionless parameter $\frac{L_Q}{Z_M}$ which, as stated previously, is numerically equal to the ratio of the maximum horizontal wave induced velocity at the port to the port velocity. Given that the port velocity had been set by the plume scaling, it was therefore necessary to vary the maximum wave induced velocity at the port, u_{max}, in order to achieve different wave conditions. Equation 2.49 shows that this will be dependent on the wave number, period and amplitude. As the first two of these had already been set by the choice of wave wavelength , the wave effect at the port was varied by using a range of wave amplitudes. The wave maker available on the tank used to perform the experiments however was only able to produce waves with a maximum amplitude of 3.0 cm. Controlling

the wave effect purely by altering the wave amplitude therefore offered a very limited range of cases. However equation 2.49 shows that within the range of this experiment, the wave induced velocities increase as the surface is approached, therefore the discharge depth can also be used to vary the effect of the wave on the port.

It was therefore decided to discharge the solution from three different depths, 30, 45 and 60cm, and vary the wave amplitude at each of these depths. In this way plumes under a wider range of wave conditions could be studied. Even at the greatest discharge depth of 60cm, the diffuser was still 10cm above the bottom of the tank and therefore the effect of the bottom of the tank will be negligible, given that the bottom boundary layer will be of the order of a few millimetres [16].

While this is not an ideal solution, introducing a further variable to the investigation, Chin has shown that any increase in dilution is not dependent on the ratio $\frac{H}{L}$ [16] and therefore variation of this ratio will not affect the outcome of the experiment. However, given a wave maker capable of producing waves with larger amplitudes and wavelengths the wave conditions would have been altered solely by variation of amplitude and wavelength. This would have allowed the diffuser to remain permanently fixed in position.

4.3 Experimental Apparatus

The experiments were conducted in a glass sided and bottomed tank 7.5m long, 0.4m wide and 1.0m deep. At one end of the tank was fitted a computer controlled paddle wave maker and at the other a 2m long, absorbing foam beach. For all experiments the tank was filled with tap water ($\rho = 998 kgm^{-3}$ at $20^{o}C$ [41]) to a depth of 0.7m. The discharge solution was held in a reservoir above the flume connected to which were the variable rate pump and a limiting valve for

controlling the flow rate and a flow meter for measuring the flow rate. The diffuser was then fitted across the width of the tank and plumbed to the flow meter. Underneath the tank was fitted a scanning beam box, as described in chapter 3, this produced a pseudo light sheet, 0.7m wide, which was projected vertically through the glass bottom of the tank (fig. 4.19).

As Rhodamine B powder is not a pleasant substance to work with a stock solution of highly concentrate dye was made up by dissolving 2.56g of Rhodamine powder in a 2.5l winchester of methanol. 10ml of this concentrate stock solution were then added to each winchester of methanol to be discharged.

4.3.1 Image Capture

The diffuser was positioned so that the light sheet was in the plane of the discharge and passed directly through the middle of the central port (fig. 4.19). Images of the fluorescing plume were captured using an 8 bit, black and white, 576x768 pixel array, Cohu CCD camera connected to a frame grabber card installed in a PC. The camera was fitted with an orange filter to filter out the blue laser light so that only the orange fluorescent light was detected. The software used [44] allowed a maximum of ninety nine images to be captured, with a variable time interval between images. All the line experiments were conducted with images taken at half second intervals. This interval was chosen as a compromise between having information from enough wave cycles to be able to create a time average and enough information to record a complete cycle.

The camera was positioned so that the whole of the plume could be visualised and at a height level with the water surface. It was found that if the camera was above or below this level then information would be lost due to reflections from the water/air interface.

Using an 8 bit camera, only 256 grey levels were available so the gain of the

camera had to be set by trial and error to a point where the image was never overloaded, that is the image was brighter than the brightness associated with a pixel value of 255, but also contained as much information as possible about the more dilute and therefore dimmer regions of the plume. Any overloading of the image would prevent that image being used in a time average, as the extent to which the image was brighter than the value of 255 would not be recorded. At the other extreme if the gain was set too low, then a lot of information about the more dilute regions would not be recorded. As different wave conditions produced different diluting effects it was often necessary to repeat this trial and error process for each experiment.

4.4 LIF experiments

Before and after each experiment a series of calibration measurements were taken so that the pixel values of known concentrations could be found. This was done by taking images of a small tank filled with plume solution of a known concentration, placed into the the light sheet. A background image was also taken with the tank completely filled with dye. By removing this background image from images taken during the experiment, and also the calibration, it was hoped that any imperfections in the light sheet could be compensated for.

Once the calibration images had been taken, the calibration tank was removed and for wave experiments, the wave maker started. When the waves reached the far end of the tank and their full amplitude, the pump and limiting valve were adjusted to give the desired flow rate. Only once the plume had reached the free surface was the sequence of images recorded.

Table 4.4 shows the parameters for each of the experiments performed. For all experiments conducted with waves the wavelength was 4.3m.

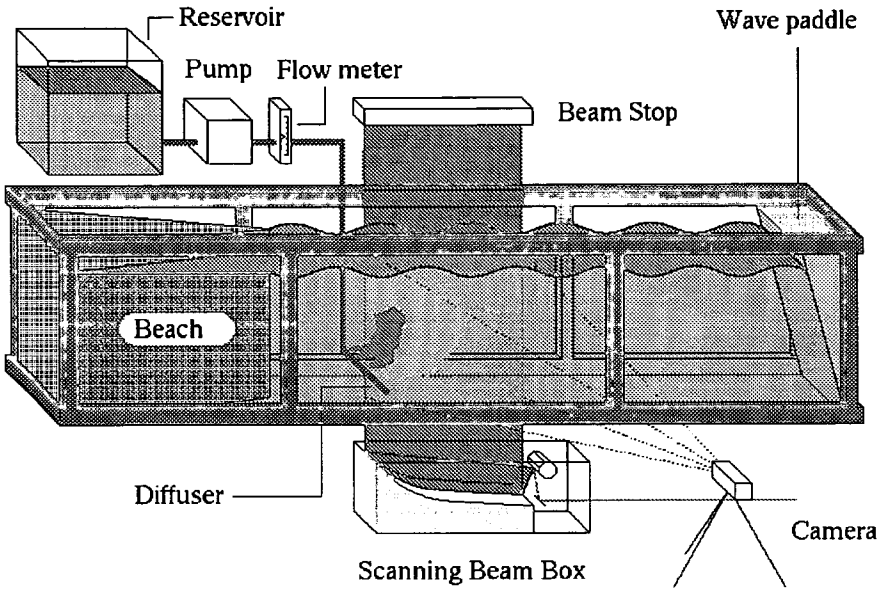

Figure 4.19: Wave flume equipped for LIF study of buoyant plumes.

Expt no.	Discharge depth/m	Wave amp/m	$\frac{L_Q}{Z_M}$
1	0.30	-	-
2	"	0.015	0.051
3	"	0.019	0.068
4	"	0.020	0.095
5	0.45	-	-
6	"	0.020	0.061
7	"	0.022	0.067
8	"	0.030	0.091
9	0.60	-	-
10	"	0.020	0.053
11	"	0.025	0.066
12	"	0.030	0.079

Table 4.1: Parameters for LIF line plume experiments performed.

Chapter 5

Round plume experiments

5.1 Summary

This chapter discusses the design of the round plume experiments and describes the apparatus used. Justification for the use of a moving diffuser as opposed to a moving water column is given and the LIF and PIV experiments performed are described.

5.2 Experimental Design

It had initially been hoped to conduct PIV experiments on the line plume described in the previous chapter. Preliminary experiments however showed that this was not possible with the apparatus arranged as it was. The light sheet passed through the central port of the diffuser, illuminating a slice through the centre of the plume. While the diffuser was discharging solely dyed effluent the discharge from the three ports between the camera and the central port did not interfere with the image of the fluorescing section of the plume, the dilution of the plumes being large. When seeding particles were introduced into the flow however, their opaque nature obscured the view of particles in the measurement region. It was initially thought that this could be overcome by moving the light

sheet to beneath the port closest to the camera. As, due to the construction of the scanning beam box, this was not possible a further solution had to be sought.

The previous line plume experiments had shown that the greatest influence of the wave was to be found in the region close to the port, before the plumes had merged. If the wave effect is greatest before merging then a study of wave/plume interaction could be made on a single round plume. This would overcome the problem of interference from particles contained within other plumes.

Ideally the round plume investigation could have been conducted in the same tank as the previous experiments, allowing the use of the same wavemaker. This would allow direct comparison with the previous results to be made. The tanks within the group though are heavily used and the purple tank was not available within the time scale required for this study, a move to a different tank was thus required.

The available tank had the disadvantage of not being fitted with a wavemaker but was fitted with a computer controlled trolley able to run horizontally along its length. While at first this appeared to be a major hurdle in a study of the effect of waves on plumes, when the motion induced by the waves was considered this became less of a problem. The previous experiments had shown that the increase in dilution at the port was mainly due to the induced motion being at first in the same direction as the discharge and then opposing it. This type of motion could be modelled by fixing the diffuser to the moving trolley. Though it was thought that the vertical motion of the wave could also be simulated by equipping the trolley with the means to raise and lower the diffuser this was deemed prohibitively complicated for the small increase in accuracy. Despite the fact that this approach neglects the vertically induced motion of the wave, it does allow the effect of just one of the components of the wave motion to be carefully controlled and examined. Further justification of this approach is given later in the chapter.

5.2.1 Discharge properties

To keep experimental conditions as similar as possible to those used in the two-dimensional experiments the same discharge solution of pure methanol was used. However to produce a single three-dimensional plume a new diffuser was designed. A single half inch diameter copper tube was terminated with a 2.7mm diameter port, the same diameter as used in the previous experiments (fig 5.1). By keeping the flow rate through the port the same as in the previous experiments it was hoped to again produce a plume with a Froude number of 14 and a Reynolds number greater than 4000.

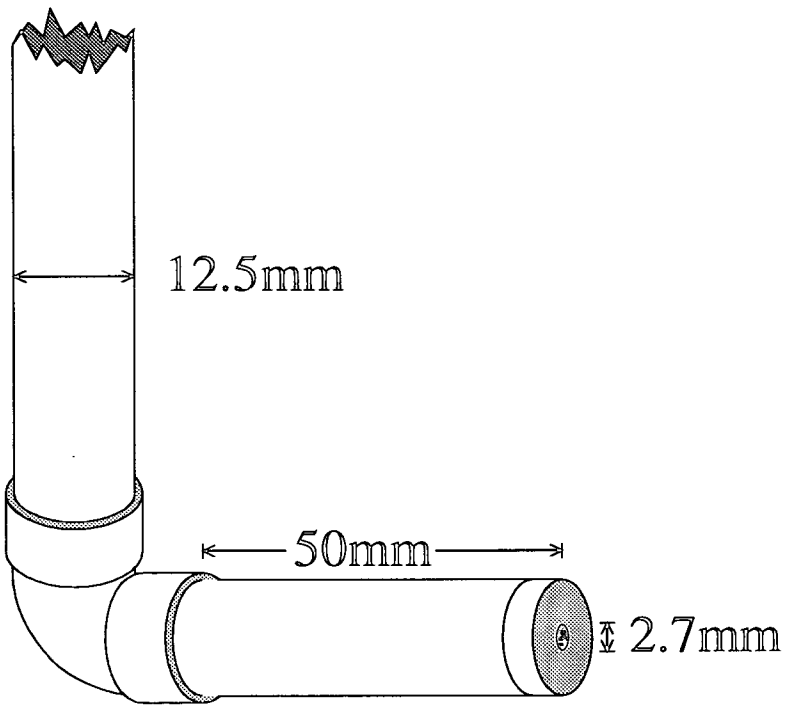

Figure 5.1: Model diffuser used for round plume experiments.

5.2.2 Wave emulation

As described in chapter 2, within the experimental parameters of this experiment, the effect of the waves is to induce an elliptical motion in the water column

beneath the surface. This motion can be resolved into two sinusoidally varying components, one horizontal the other vertical. Under the conditions being investigated the horizontal component is approximately twice as large as the vertical component and it is this component that opposes the discharge. It was decided therefore to examine the effect of this component of the wave motion by moving the diffuser and camera together horizontally in a sinusoidal motion through a tank of still water.

While the case of water moving past the diffuser in a sinusoidal motion and that of the diffuser moving sinusoidally through still water are not obviously identical as the frames are accelerating, it has been shown that they are [45, 46, 47] by putting the equations of motion of the oscillating frame in the same form as those of the inertial frame. Following Earnshaw [45] the incompressible Navier Stokes and continuity equations for the inertial frame are given as:

$$\frac{\partial u_i}{\partial t} + u_j \frac{\partial u_i}{\partial x_j} = -\frac{1}{\rho}\frac{\partial p}{\partial x_i} + \nu \frac{\partial^2 u_i}{\partial x_j^2} \tag{5.1}$$

$$\frac{\partial u_j}{\partial x_j} = 0 \tag{5.2}$$

where $x_i = (x_1, x_2, x_3)$ are the co-ordinates in the inertial (tank) frame, ρ is the fluid density and ν the fluid's kinematic viscosity. While the problem in question involves the interaction of two different liquids with different densities and viscosities it can be seen from the previous experiments that the discharged fluid is quickly diluted to concentrations of around two percent. At this dilution the plume's density and viscosity are very close to that of the receiving water and therefore the plume and the pure water can be thought of as being one liquid with small perturbations in both density and viscosity. Any acceleration due to buoyancy brought about by the difference in the liquid's density will also only be in the vertical direction and therefore will be the same in both frames.

In the trolley frame, the co-ordinates (x_1', x_2', x_3') oscillate relative to the tank such that

$$\begin{aligned} x_1' &= x_1 - a\sin\omega t \\ x_2' &= x_2 \\ x_3' &= x_3 \\ t' &= t \end{aligned}$$

Now

$$\frac{\partial f}{\partial x} = \frac{\partial f}{\partial x'}\frac{\partial x'}{\partial x} + \frac{\partial f}{\partial t'}\frac{\partial t'}{\partial x} = \frac{\partial f}{\partial x'} \tag{5.3}$$

and

$$\frac{\partial f}{\partial t} = \frac{\partial f}{\partial x'}\frac{\partial x'}{\partial t} + \frac{\partial f}{\partial t'}\frac{\partial t'}{\partial t} = \frac{\partial f}{\partial t'} - a\omega\cos\omega t\frac{\partial f}{\partial x'} \tag{5.4}$$

so equations 5.1 and 5.2 become

$$\frac{\partial u_i}{\partial t'} - a\omega\cos\omega t\frac{\partial u_i}{\partial x'} + u_j\frac{\partial u_i}{\partial x_j'} = -\frac{1}{\rho}\frac{\partial x_i'}{+}\nu\frac{\partial^2 u_i}{\partial x_j'^2} \tag{5.5}$$

and

$$\frac{\partial u_j}{\partial x_j'} = 0 \tag{5.6}$$

As the origin of the non-inertial, trolley, frame moves with velocity $(a\omega\cos\omega t, 0, 0)$,

$$\begin{aligned} u_1' &= u_1 - a\omega\cos\omega t \\ u_2' &= u_2 \\ u_3' &= u_3 \end{aligned}$$

Substituting these into equations 5.5 and 5.6 gives

$$-\frac{1}{\rho}\frac{\partial p}{\partial x_i'}+\nu\frac{\partial^2 u_i'}{\partial x_j'^2}=\frac{\partial u_i'}{\partial t'}-a\omega^2\sin\omega t'\delta_{i1}-a\omega\cos\omega t'\frac{\partial u_i'}{\partial x'}+u_j'\frac{\partial u_i'}{\partial x_j'}+a\omega\cos\omega t'\frac{\partial u_i'}{\partial x_j'}\delta_{j1} \tag{5.7}$$

$$\frac{\partial u_j'}{\partial x_j'}=0 \tag{5.8}$$

where

$$\delta_{i1}=\begin{cases}1 & \text{if } i=1\\ 0 & \text{if } i\neq 1\end{cases}$$

As $p'=p-\rho a\omega^2 x\sin\omega t'$

$$\frac{\partial u_i'}{\partial t'}+u_j'\frac{\partial u_i'}{\partial x_j'}=-\frac{1}{\rho}\frac{\partial p'}{\partial x_i'}+\nu\frac{\partial^2 u_i'}{\partial x_j'^2} \tag{5.9}$$

and

$$\frac{\partial u_j'}{\partial x_j'}=0 \tag{5.10}$$

This shows that the motion in the trolley frame is governed by the same equations as in the tank frame but with a different pressure field, therefore the flows will be identical.

To make comparisons with the line plume experiments the trolley movement was designed to model the horizontal motion of the waves used in the previous experiments. To achieve this the period of the trolley oscillations used was equal to the period of the waves used in the earlier experiments. As stated in chapter 2 the wave effect on the discharge is numerically equal to the ratio of the wave induced velocity at the port to the port discharge velocity so the 'wave effect'

was varied by changing the amplitude of the trolley motion while keeping the period the same. Though not necessary to change the effect of the waves as in the previous experiments, discharges at three different depths were studied for comparison.

In order to achieve the relative motion both the camera and the diffuser needed to be moved simultaneously relative to the tank. One of the Edinburgh tanks, the red tank, was already fitted with a computer controlled trolley that could move on rails along the length of the tank and it was decided to carry out the experiments in this tank. While the mounting of the diffuser on the trolley seemed to be easily achievable, mounting the camera presented a number of difficulties.

In the previous experiments the camera had been positioned approximately two metres from the light sheet so that the whole plume was within the field of view of the camera. This distance could be shortened by using a wider angle lens but this would result in quite large optical distortion of the image, such as are seen in images using a very short focal length fish-eye lens. The problem of mounting the camera on the trolley but at a distance of around two metres from the light sheet therefore needed to be addressed.

Initially it was thought that the camera could be mounted on an arm extending from the trolley but this presents a number of practical challenges ranging from the actual physical size of the apparatus to counter balancing the trolley. However probably the most significant would be that any small vertical movement in the trolley would be greatly magnified at the end of a two metre arm which could result in the camera's and diffuser's motion being far from identical.

If the camera could be mounted on the trolley itself however, then any difference in movement between the camera and diffuser should be minimised, however the camera still needs to view the diffuser and light sheet under the trolley. It was thought that this could be achieved by reflecting the image of the plume round to the camera by means of an inverted periscope. The design finally decided upon is

shown in figure 5.2. The height of the mirrors was chosen such that the camera's full field of view would not be restricted and the width was chosen so that the full width of the light sheet could be viewed without the need to move the mirrors.

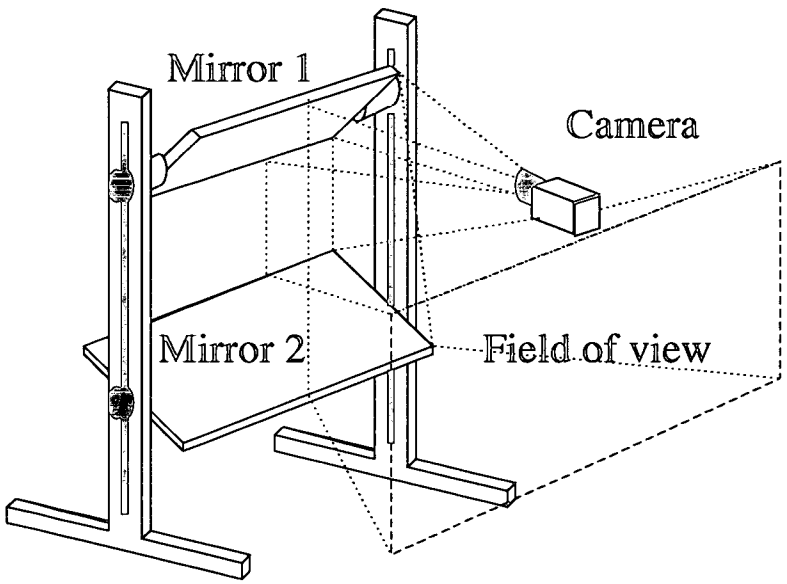

Figure 5.2: Diagram showing arrangement of mirrors for round plume experiments

5.2.3 3d visualisation

Unlike the line plume of the initial experiments which was assumed to be identical along its length above the merging of the individual plumes, with a round plume, as the name implies, this is not the case. In order to visualise the variation in concentration and velocity fields along the y-axis of the plume, it was decided to image a number of slices through the plume and then combine these to build a three dimensional representation of the plume (fig. 5.3). This would entail the laser light sheet being passed through the plume at a number of places along its y-axis.

As it was not possible to move the scanning beam box and therefore the light sheet in this plane, it was instead decided to move the plume relative to the light

sheet. This was achieved by mounting the diffuser on a section of the trolley that could be moved across the width of the tank. The camera however was mounted on a fixed section of the trolley so that the light sheet and therefore the section of the plume being illuminated, would always remain in focus (fig. 5.4).

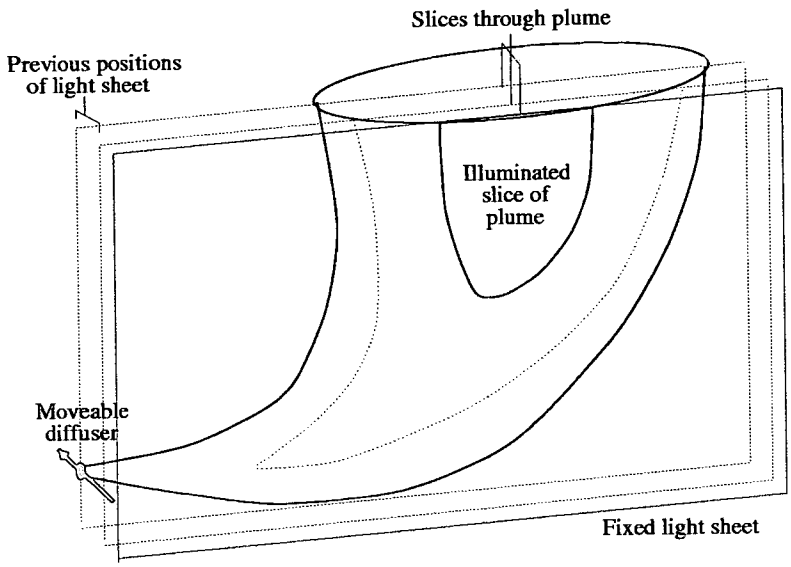

Figure 5.3: Diagram showing cross sectional slices through round plume

5.3 Experimental Apparatus

The round plume experiments were conducted in a glass bottomed and sided tank 6.0m long, 1.0m wide and 0.5m deep, known as the 'red tank'. This tank was also fitted with a computer controlled trolley able to run the entire length of the tank. As previously described, on this were mounted the diffuser and camera as well as the effluent reservoir, pump and flow meter. As with the purple tank described in the previous chapter, the red tank was also equipped with a scanning beam box to produce a metre wide pseudo laser light sheet. This light sheet too was projected vertically through the centre of one of the central sections of the tank (fig. 5.7).

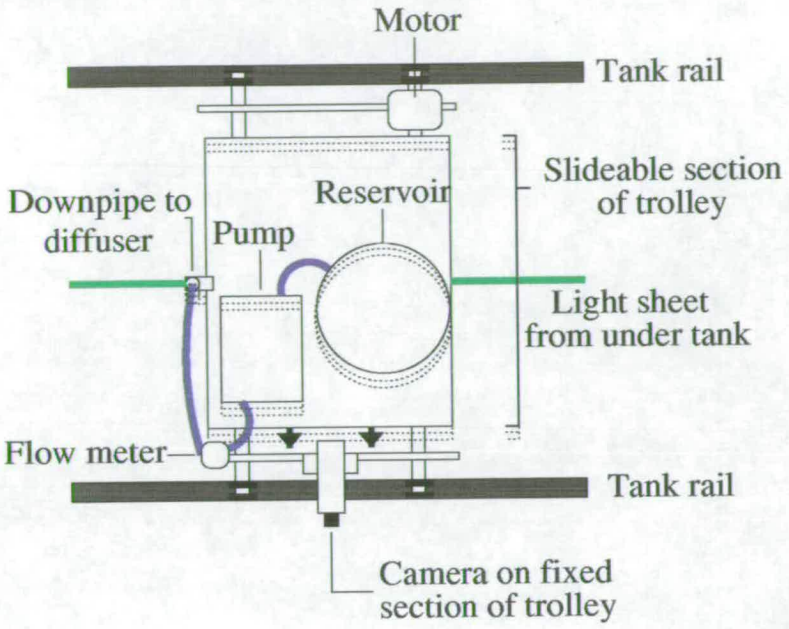

Figure 5.4: Diagram showing lateral adjustment of trolley

5.3.1 Trolley programs

The Mint software [48] controlling the trolley servo motor required two data files to reproduce the required trolley motion. The first a *.mnt file giving the program parameters such as the number of oscillations required, the second a *.arr file containing a list of numbers relating to the trolley's velocity at a given step in a single oscillation. To produce these data files a further program was used [49] that when fed with an oscillation time period and amplitude would output the relevant data files. These data files were produced for each of the wave conditions with the time period being kept constant but with the amplitude being varied.

5.3.2 Image capture

For the LIF experiments conducted the Cohu camera and frame grabbing software described in chapter 4 were again used but for the PIV experiments however a cooled, 12 bit, PCO CCD camera was used.

The PCO camera was used in its long double exposure mode [50] which allows two images to be taken a short time interval apart and was controlled by OFS VidPIV software and a TC142 timing box [51]. The exposure time of the first image is governed by the length of TTL pulse initially sent to the camera but the second exposure time is fixed by the configuration in which the camera is being run, in this case 119ms. In the exposure mode used a dead time of $1\mu s$ separated the two exposures.

Bearing in mind the technical considerations outlined in 3 the required exposure time was calculated from the theoretical plume discharge rate, the camera's field of vision and a proposed interrogation area of 32x32 pixels. To acquire pairs of images with the required particle displacement it was necessary that the particles be imaged on successive scans of the laser beam when used at its highest scan rate of 150Hz. Scanning at this frequency gives a scan period of 7ms and to prevent double exposure of any of the particles, this also gives the required exposure time. While it was possible to set the first of the camera's exposures to this value using a pulse of the same length the fixed length of the camera's second exposure was longer than required, so it was necessary to use an external electronic shutter fitted between the camera and lens. The timings for the electronic shutter could also be controlled by the PIV software, the timing box and a Uniblitz shutter driver [52]. The pulse timings, device responses and resultant image exposure times are shown in figure 5.5.

So that the velocity field at different phases of the 'wave motion' could be measured, it was necessary to trigger the camera from the motion of the trolley. A line had previously been connected from the servo motor of the trolley giving a voltage output proportional to the velocity of the trolley and this was used to trigger the camera. The signal was first amplified and then fed into a peak locating box. This box produced a positive TTL pulse at each peak in the signal from the trolley, corresponding to the point at which the trolley was travelling at it's

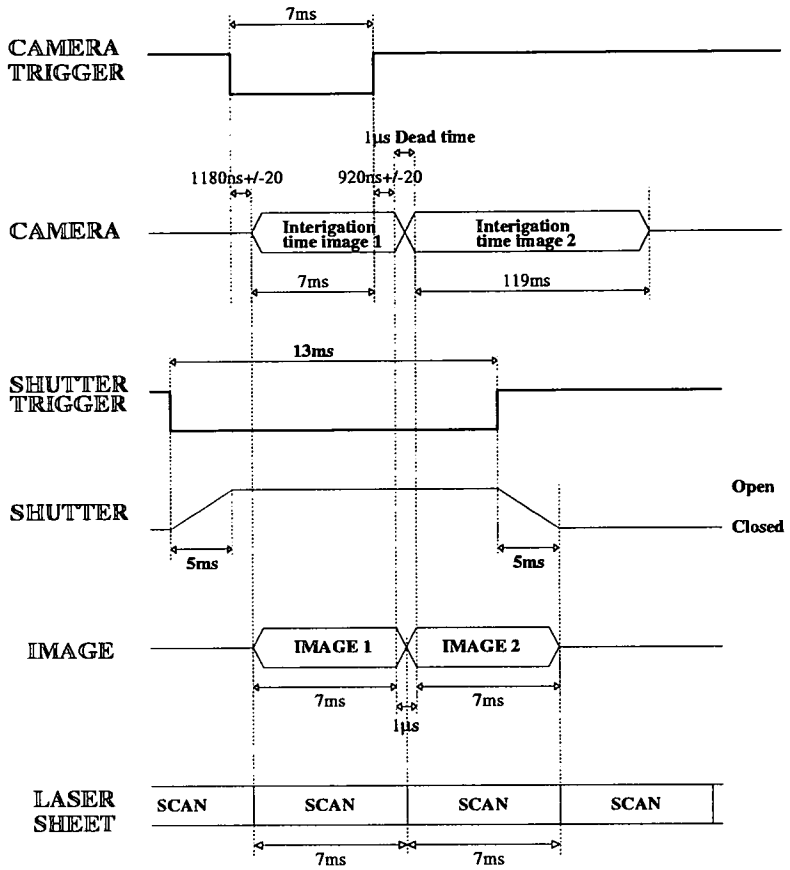

Figure 5.5: Diagram showing PCO camera exposure and shutter timings

highest velocity, that is at the central point of its oscillation, down the tank. The pulse from the peak locating box was then fed into a pulse generator, enabling a delay to be added, before a pulse was finally sent to the timing box connected to the PIV computer allowing a further delay to be added before triggering of the camera. To ensure the camera was triggered at the correct phase of the motion the signal from the trolley and that to the camera were monitored using a CRO and the delay on both the signal generator and PIV computer adjusted until the correct phase of the motion was being imaged. The timing electronics are shown on figure 5.6.

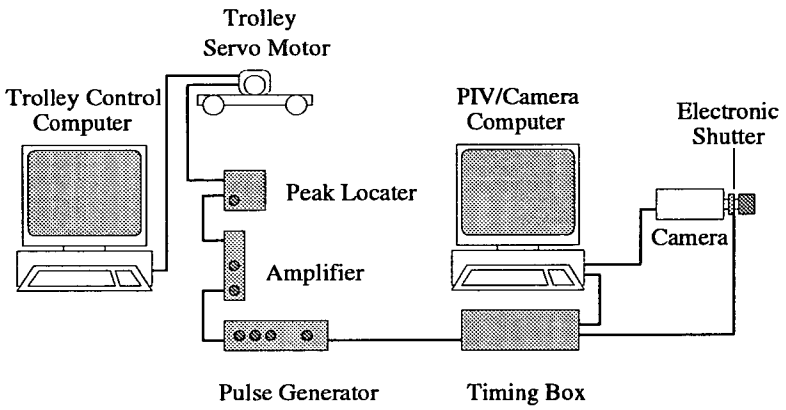

Figure 5.6: Diagram showing timing for PIV experiments

5.4 LIF experiments

The plume solution was dyed with the same stock solution used in the previous experiments, however 20ml of solution was used per winchester (2.5l) of methanol instead of the usual 10ml due to preliminary experiments showing that the plume fluoresced less brightly than previously. As before a series of calibration images was taken before and after each experiment using known dilutions of plume solution. For the 'wave' experiments the trolley was then set in motion using the program relevant to the amplitude required. The pump was then turned on and the plume allowed to reach the surface before the camera was set running. Table 5.1 shows the parameters of the LIF experiments conducted

5.5 PIV experiments

The PCO camera and PIV software is a highly used resource and therefore it was not possible to conduct the same range of experiments as for the LIF work. As well as the no-waves case only two further conditions were studied and for each of these only two slices through the plume were investigated. It was hoped however

Expt no.	H/m	z disp./mm	Trolley amp/cm	$\frac{L_Q}{Z_M}$
i	0.30	0	-	-
ii	0.30	5	-	-
iii	0.30	10	-	-
iv	0.35	0	-	-
v	0.35	5	-	-
vi	0.35	10	-	-
vii	0.40	0	-	-
viii	0.40	5	-	-
ix	0.40	10	-	-
x	0.30	0	3.0	0.034
xi	0.30	5	3.0	0.034
xii	0.30	10	3.0	0.034
xiii	0.30	0	4.0	0.045
xiv	0.30	5	4.0	0.045
xv	0.30	10	4.0	0.045
xvi	0.30	0	5.0	0.056
xvii	0.30	5	5.0	0.056
xviii	0.30	10	5.0	0.056
xix	0.35	0	6.0	0.067
xx	0.35	5	6.0	0.067
xxi	0.35	10	6.0	0.067
xxii	0.35	0	7.0	0.079
xxiii	0.35	5	7.0	0.079
xxiv	0.35	10	7.0	0.079
xxv	0.35	0	8.0	0.090
xxvi	0.35	5	8.0	0.090
xxvii	0.35	10	8.0	0.090
xxviii	0.40	0	3.5	0.040
xxix	0.40	5	3.5	0.040
xxx	0.40	10	3.5	0.040
xxxi	0.40	0	5.5	0.062
xxxii	0.40	5	5.5	0.062
xxxiii	0.40	10	5.5	0.062
xxxiv	0.40	0	7.5	0.084
xxxv	0.40	5	7.5	0.084
xxxvi	0.40	10	7.5	0.084

Table 5.1: Parameters for LIF round plume experiments performed.

that sufficient information could be gained from these limited results.

Further to this the camera/lens arrangement used for the PIV experiments though giving the required spatial resolution, was unable to fit the full plume within its field of vision. As from initial LIF experiments it had been seen that the region in which the wave motion had greatest effect was that closest to the port, this was the region studied.

While it has been shown that conifer pollen can be successfully used in the studies of flows in water (ρ=0.998kgl^{-1})[32, 53, 45, 54] the present study required the use of pure methanol (ρ=0.790kgl^{-1}) and its suitability could therefore not be assumed. While pollen mixed with water remains suspended for several hours without visible settling [32], pollen mixed with pure methanol settles in a matter of seconds. This initially suggests that pollen's response to the flow will not be very good. However early experiments to measure the plumes's concentration showed that it quickly reaches that of the order of a few percent. While pollen in pure methanol had settled quickly, pollen in a solution of ninety percent water and ten percent methanol, a solution comparable to that of the plume near the diffuser, showed no visible settling over a period of hours. This suggested that pollen could after all be used for this study.

The density change of the plume solution not only affects the buoyancy of particles in it but also its refractive index. This had not been considered a problem with the line plume experiments. The dilutions of the effluent were high and therefore the differences in refractive index small. Any small variations in the imaged position of a given 'point' or any blurring due to the index mismatches would also be averaged out by the time averaging process. The PIV technique however is dependent on being able to accurately determine the change in position of the particles and is also susceptible to change in particle size which could be caused by blurring of the particles.

As with the line plume experiments the plume soon becomes very dilute and

so any differences in refractive index will be very small, however close to the port they may be more significant. In this region however the discharge also has its highest velocity, initially beyond the measurement capacity of the PIV system in use resulting in blurring of the particles. Any further blurring due to mismatching of the refractive indices is therefore unimportant. These issues and proposed improvements to the technique are discussed further in the final chapter.

In order to produce the seeding density required in this region approximately 3ml of pollen were added to each 2.5l of methanol. The discharge was then set to the correct rate using the pump and limiting valve before the required trolley motion was started. Once the plume had reached a steady state the sequence of images was taken. For those experiments in which the trolley remained stationary the camera was triggered at its maximum frequency of 2Hz by the PIV software itself rather than by the trolley movement.

Expt no.	H/cm	z disp./mm	Trolley amp./cm	$\frac{L_Q}{Z_M}$	Phase/^{o}
I	0.45	0	0	-	-
II	0.45	0	7.5	0.084	0
III	0.45	0	7.5	0.084	180
IV	0.45	0	7.5	0.084	270
V	0.45	0	7.5	0.084	90
VI	0.45	0	3.5	0.040	0
VII	0.45	0	3.5	0.040	180
VIII	0.45	0	3.5	0.040	270
IX	0.45	0	3.5	0.040	90
X	0.45	10	0	0	-
XI	0.45	10	7.5	0.084	0
XII	0.45	10	7.5	0.084	180
XIII	0.45	10	7.5	0.084	270
XIV	0.45	10	7.5	0.084	90
XV	0.45	10	3.5	0.040	0
XVI	0.45	10	3.5	0.040	180
XVII	0.45	10	3.5	0.040	270
XVIII	0.45	10	3.5	0.040	90

Table 5.2: Parameters for PIV round plume experiments performed.

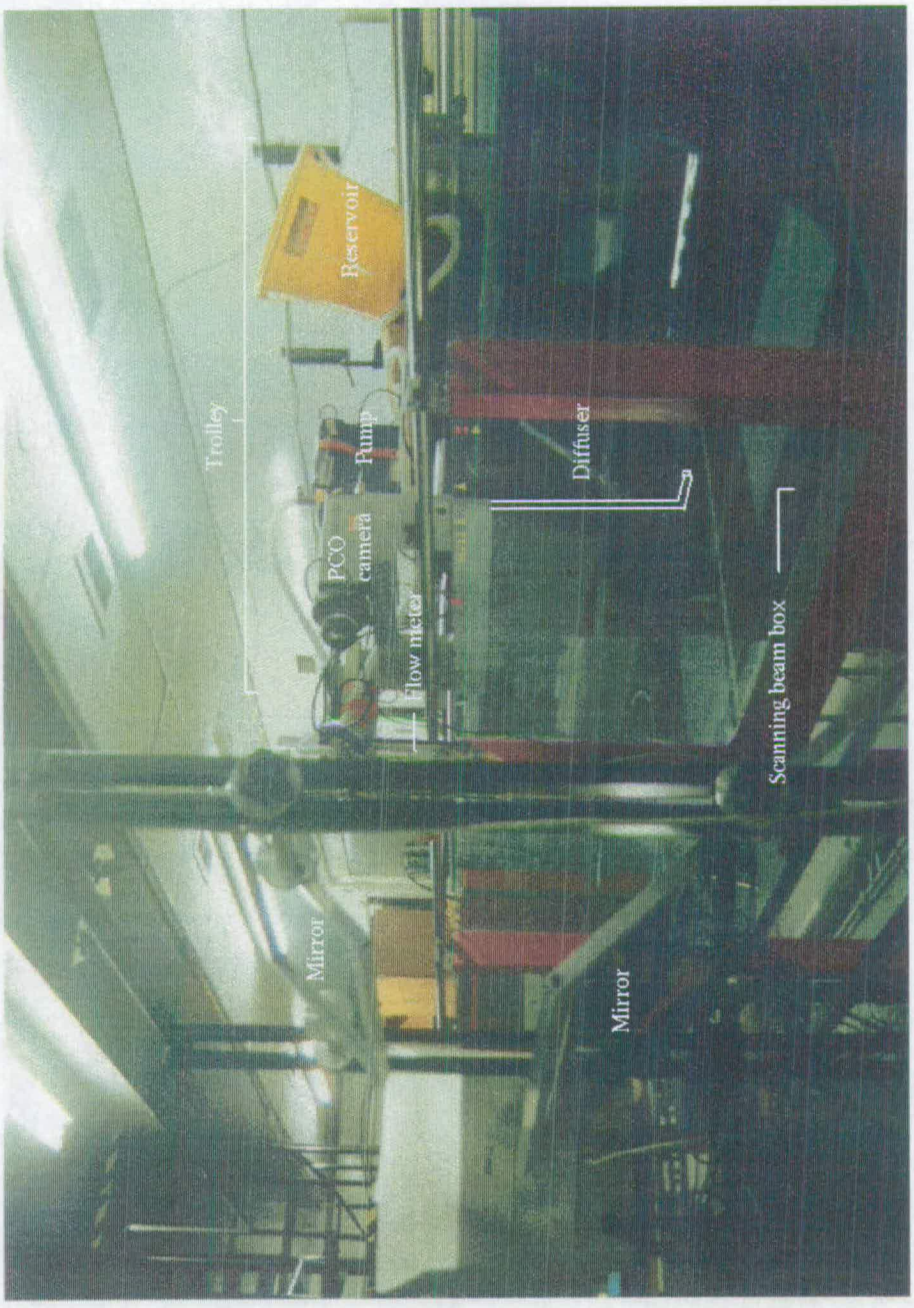

Figure 5.7: Experimental apparatus for round plume experiments

through by the fractional variation in the background image taken after each set of experiments.

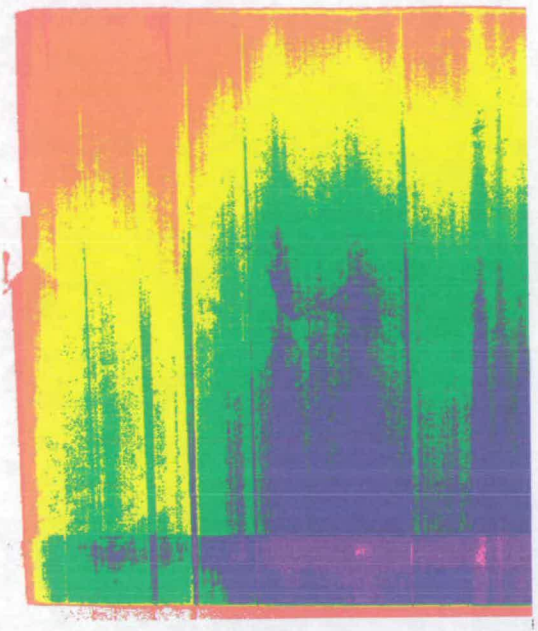

Figure 6.1: Fasle coloured image showing variation in laser light sheet

Mathematically this process may be written as

$$I_{P(i,j)} = \frac{I_{O(i,j)}}{I_{B(i,j)}} \overline{I_B} \tag{6.1}$$

where $I_{P(i,j)}$ is the intensity of pixel (i,j) in the processed image, $I_O(i,j)$, the intensity of that pixel in the original image, $I_B(i,j)$ the intensity of that pixel in the background image and $\overline{I_B}$, the average pixel intensity of the background image. While background effects may not be obvious on a single instantaneous image, they may become more apparent on a time-averaged image composed of many instantaneous images. Figure 6.2 shows a reverse video (for clarity), time-averaged image with a number of dark vertical bands running through it caused by variation in light sheet intensity. Figure 6.3 shows the same image once it had been processed with the vertical lines much less visible.

Figure 6.2: Time averaged, reverse video CCD image.

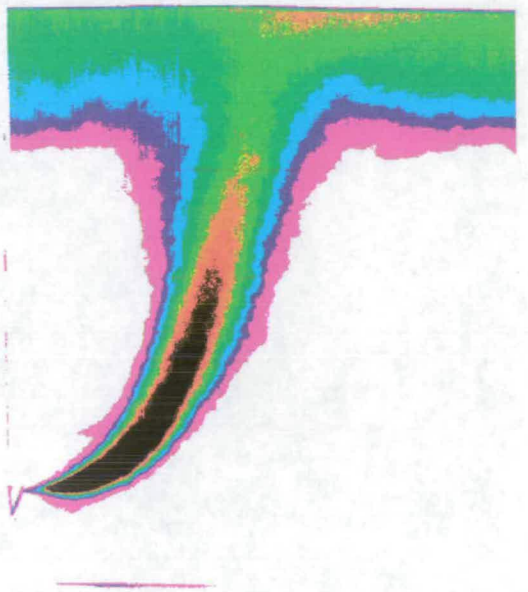

Figure 6.3: Processed image with background removed.

6.3 Calibration of concentration maps

With the background removed from all the images to be processed, including the calibration images, the images of the plume could then be calibrated. This was achieved by first finding the average pixel value associated with each of the calibration images. This was done using another program [56] to find the average pixel intensity over an area of the calibration image chosen by the user. Having found the average pixel values associated with each calibration image a calibration graph could then be plotted (fig. 6.4). From the graph the linear relationship between fluorescent intensity and concentration can clearly be seen.

Finally the calibration values could be entered into a third program [57] to convert the images of the plume (fig. 6.5) into concentration maps (fig. 6.6). For clarity this program also false coloured the image according to the calibration data. As theoretical values are normally quoted for a time-averaged plume, this program

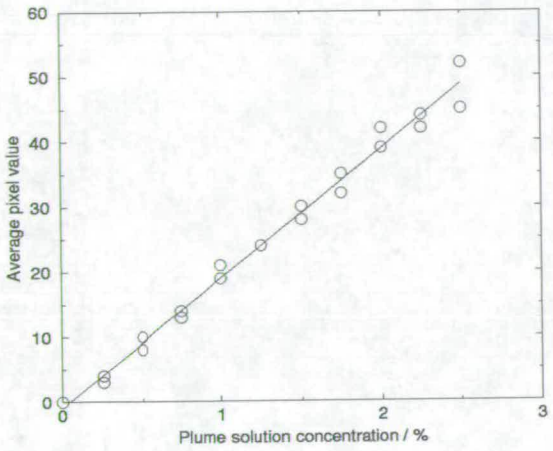

Figure 6.4: Graph showing calibration plot.

Figure 6.5: Instantaneous reverse video CCD image of plume.

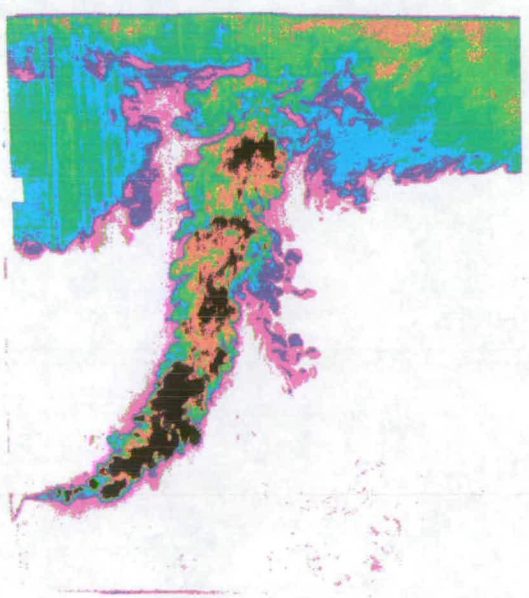

Figure 6.6: False coloured instantaneous concentration map.

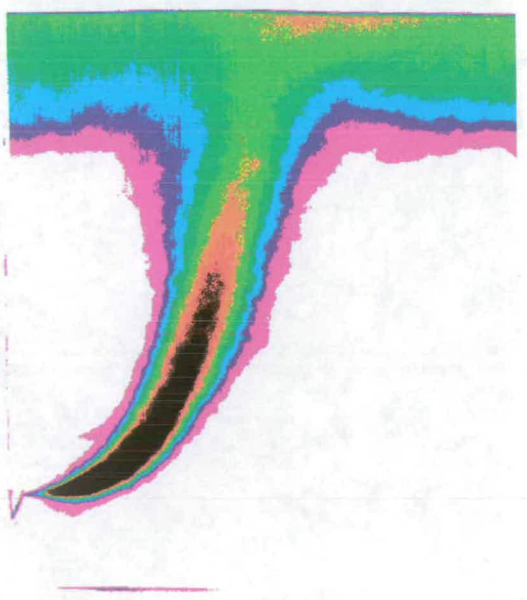

Figure 6.7: False coloured time-averaged concentration map.

also averaged all the instantaneous image files to produce a single time-averaged concentration map (fig. 6.7).

6.4 Post processing

In order to further process the LIF images an analysis program was written in C++ that also incorporated the calibration functions of the programs described above. A 'bmp' object was written that as well as containing the mathematical functions required for operations such as removal of the background information and averaging of images, also contained functions for other analysis tasks:

A 'calibrate' function to allow an image or images to be converted to false coloured, calibrated concentration maps using the data from the calibration experiments in a similar manner to the program described previously;

A 'centre' function to be detect the centreline on a calibrated, time-averaged image of the plume and output its position as well as the concentration along it together with lines normal to it;

and finally a function to find the average deviation in concentration at a point in the image from the time-averaged value at that point.

To detect the centreline of the plume two different algorithms were tried. The first approach attempted to find the centreline by scanning each row of the array containing the image intensity data and finding the highest value. These column values could then be averaged over a number of rows to give the position of the centreline. While this approach worked well with the majority of images, problems arose with images of plumes released into large amplitude waves. In these images the detected centreline appeared to be to the side of the true centreline. This may be explained by the fact that, as will be seen in chapter seven, with increasingly large wave effect the plume departs from having a Gaussian profile to one with two peaks. Under these conditions the centreline of the plume will

therefore be a local minima and the point detected by the program the more intense of the two peaks.

In an attempt to overcome this problem a second algorithm was tried. Rather than detect the greatest value of intensity along a given row, the 'centre of mass' of the row was instead found, the 'mass' of a pixel being its intensity. The central pixel of each row of the plume $j_{cl}(i)$ may then be expressed as

$$j_{cl}(i) = \frac{\sum_{j=0}^{j=j_{max}} I_{(i,j)} j}{\sum_{j=0}^{j=j_{max}} I_{(i,j)}} \tag{6.2}$$

where $I_{(i,j)}$ is the intensity of the pixel at coordinates (i, j).

While this method in theory overcomes the problem of finding the centre of a plume with two concentration peaks of equal magnitude in a plume symmetric about its axis, any lack of symmetry will result in a shift of the detected centreline from the true centreline.

Though both of these methods detected centrelines close to the true centreline for the majority of the plume rise height, correlation in the region of the plume close to the port was very poor. Figure 6.8 shows the detected centreline points marked in white (actual detected points have been retouched by hand for clarity). The departure from the true centreline may be explained by the fact that in the region close to the port the plume is horizontally orientated. Scanning the image horizontally for a maximum value or centre of mass therefore will not detect the true centreline. To find the plume centreline in this region a vertical scan through the image was also made using the maxima detection algorithm (fig. 6.9). Though this scan successfully detected the centreline in the horizontal region of the plume it can be seen that there is a departure from the true centreline in the later, vertical region of the plume.

In order to successfully detect the plume centreline over the full rise height a combination of these two scans was used. Figure 6.10 shows the centreline detected by using a vertical scan in the lower third of the plume's rise height and a

horizontal scan in the upper two thirds. This was the method of detection used in the analysis of the results described in the following two chapters.

As well as the centreline itself, the concentration profiles normal to the centreline are also of interest. The centreline detection function therefore also found the positions of a user defined number of normals at a user defined spacing along the centreline (fig. 6.11). Having detected both plume centreline and normals to it, the program was able to output the coordinates for the centreline as well as the discharge concentration along it and the normals. This allowed comparison of the centreline dilution along the full plume rise height for discharges into a range of no-wave and wave conditions.

The program's mathematical functions also made it possible to find the magnitude of the fractional average deviation in concentration from the time averaged concentration at every pixel, that is $\frac{\overline{<C'_{(i,j)}>}}{\overline{C_{(i,j)}}}$, over the complete image. Results of this type should help in identifying the regions in which the waves were having their greatest effect. The concentration map of the time averaged image was in turn subtracted from each of the instantaneous image maps and the resulting values squared to remove negative values. The result was then square rooted and averaged with the resultant values from the other images. Finally the averaged values were normalised by dividing through by the time averaged values. Mathematically this may be expressed

$$\frac{\overline{< C'_{(i,j)} >}}{\overline{C_{(i,j)}}} = \frac{\sum_{a=1}^{a=N} < C_{a(i,j)} - \overline{C_{(i,j)}} >}{N\overline{C_{(i,j)}}} \tag{6.3}$$

where $C_{a(i,j)}$ is the concentration at point (i,j) on instantaneous image number a and N the total number of instantaneous images. Figure 6.12 shows an example image showing the average magnitude of deviation from the time averaged values (white = no deviation, then red through to violet with increasing deviation).

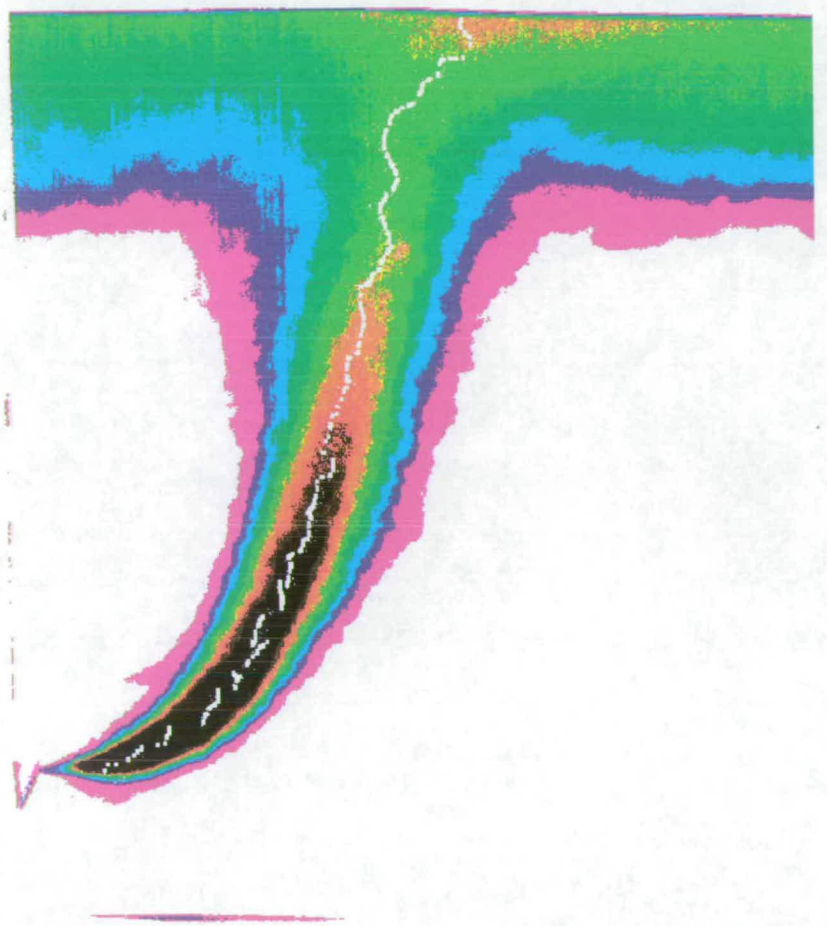

Figure 6.8: Centreline detection using horizontal scanning showing good correlation with true centreline in the vertical region of the plume.

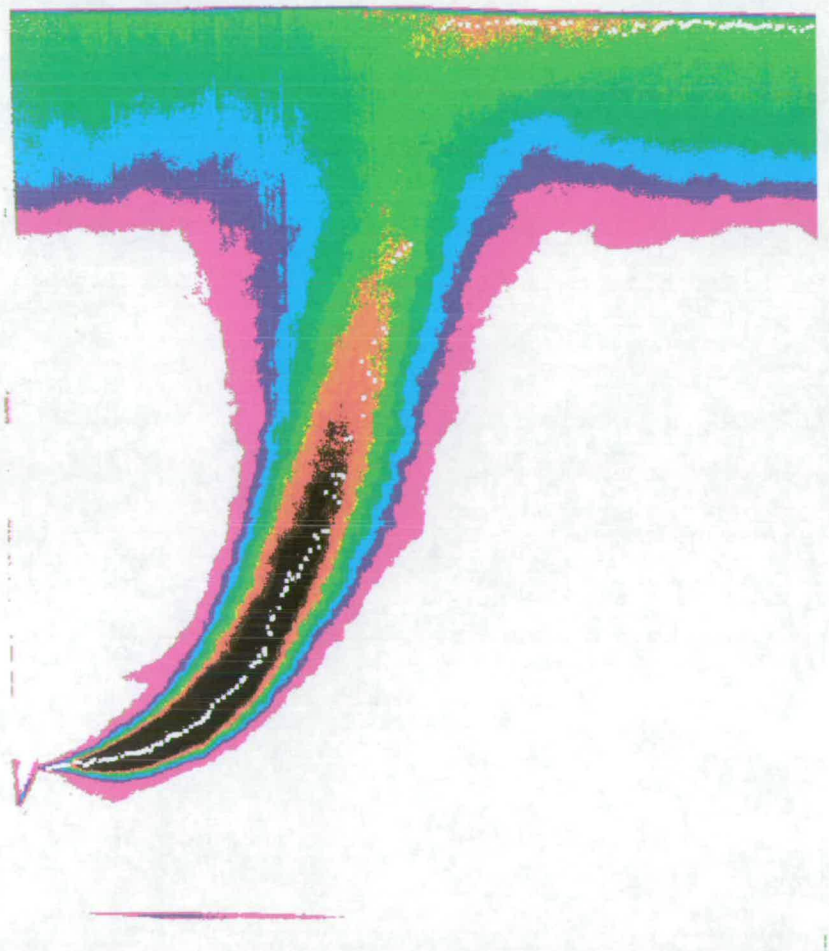

Figure 6.9: Centreline detection using vertical scanning showing good correlation with the true centreline in the horizontal region of the plume.

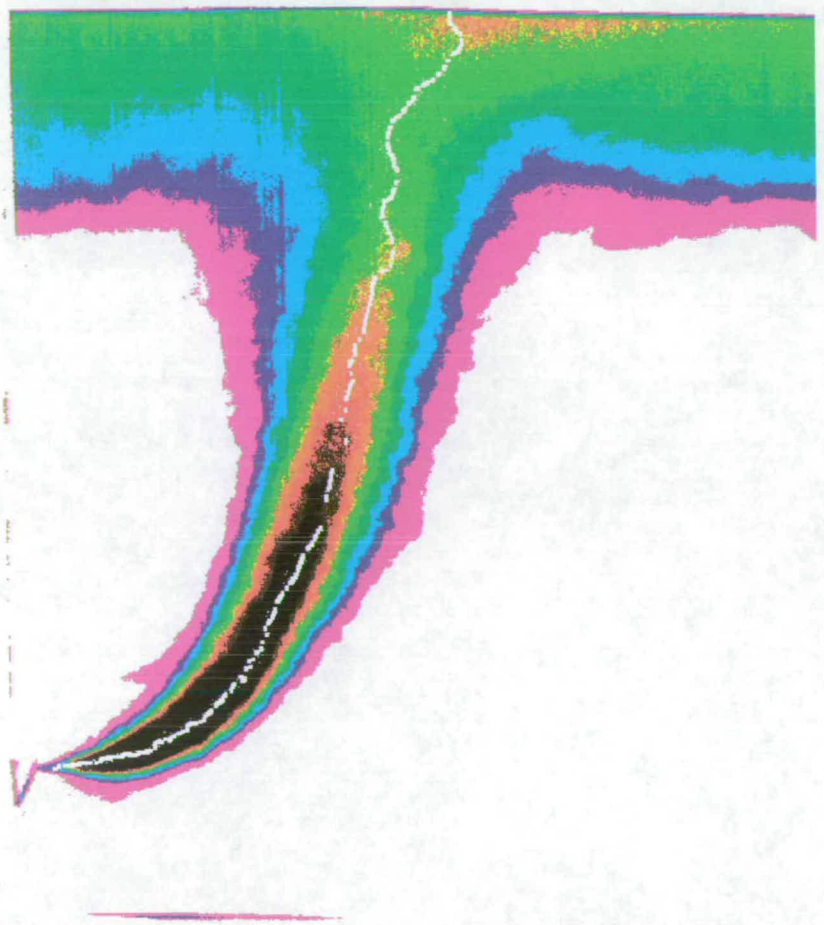

Figure 6.10: Centreline detection using combined horizontal and vertical scanning method showing good correlation with the true centreline throught the rise height of the plume.

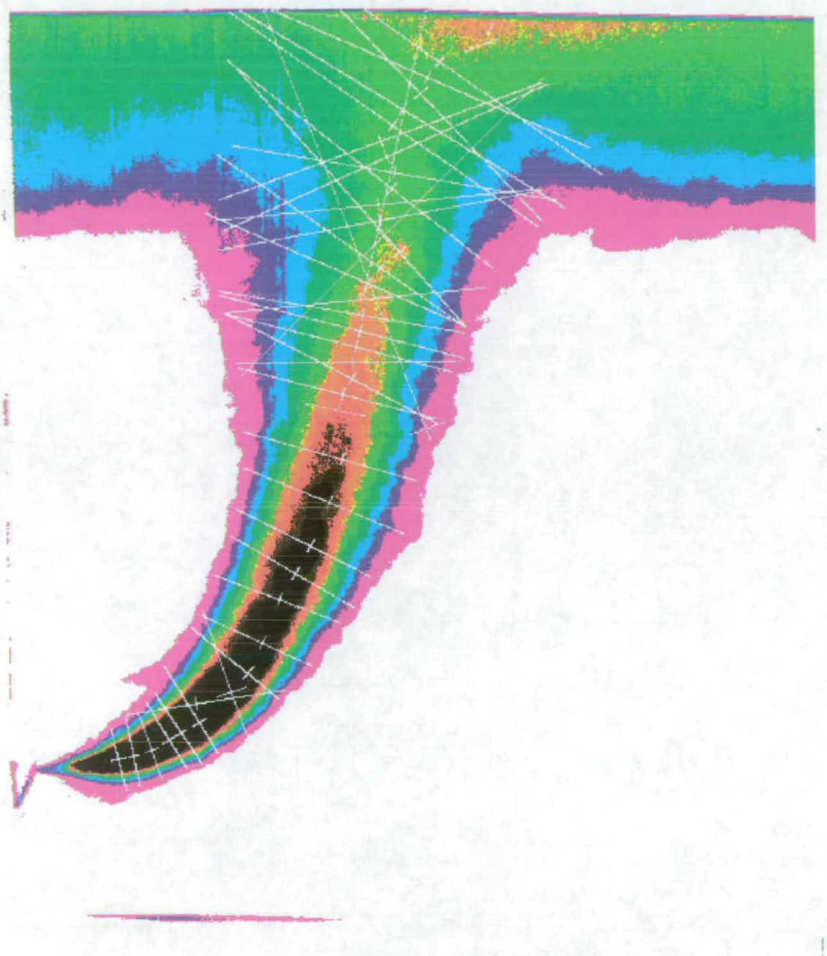

Figure 6.11: Processed image showing detected centreline and normals to it.

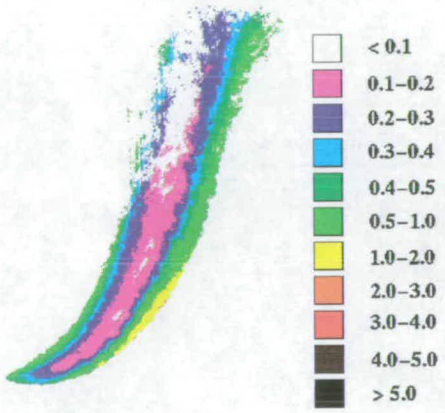

Figure 6.12: Example image showing deviation from time averaged values.

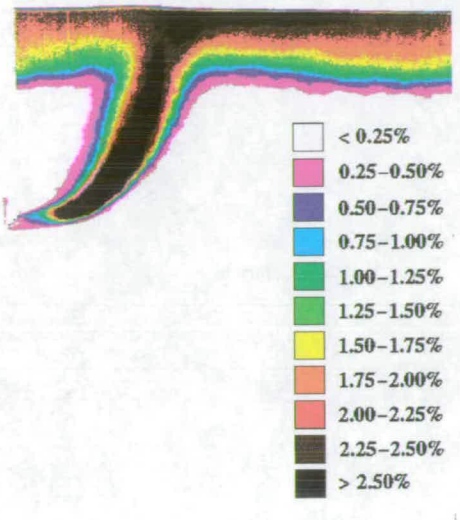

Figure 7.1: Time averaged concentration map. H=0.30m No waves

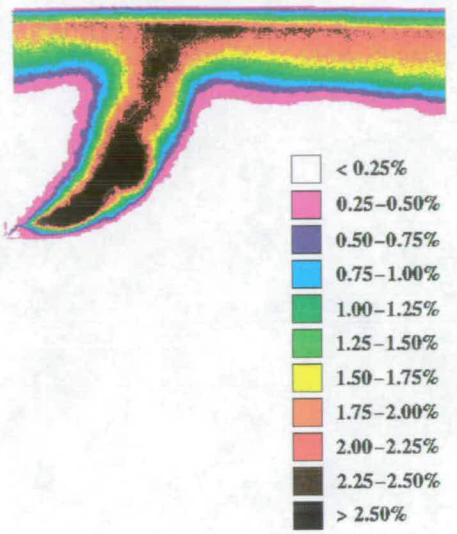

Figure 7.2: Time averaged concentration map. H=0.30m $\frac{L_Q}{Z_M}$=0.051

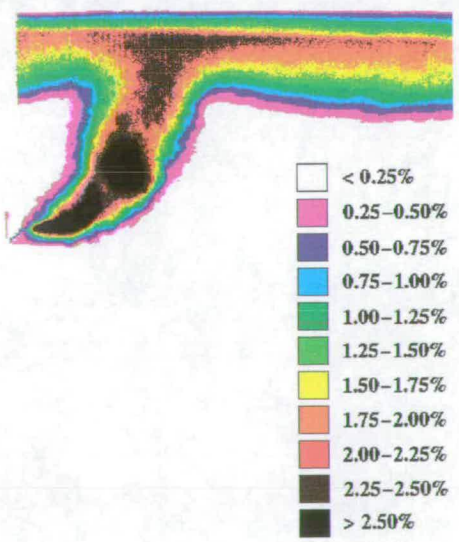

Figure 7.3: Time averaged concentration map. H=0.30m $\frac{L_Q}{Z_M}$=0.068

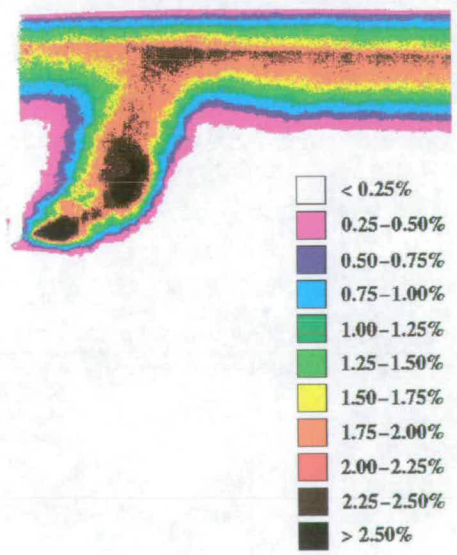

Figure 7.4: Time averaged concentration map. H=0.30m $\frac{L_Q}{Z_M}$=0.095

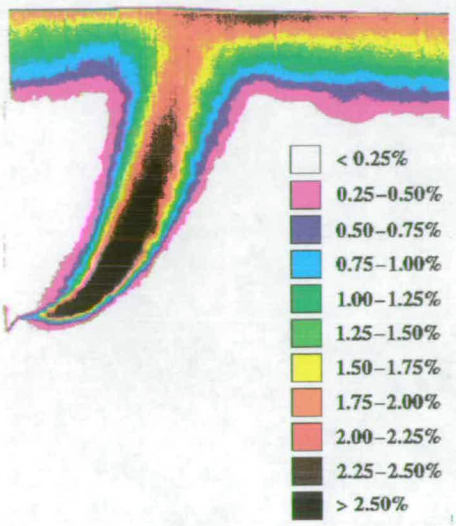

Figure 7.5: Time averaged concentration map. H=0.45m No waves

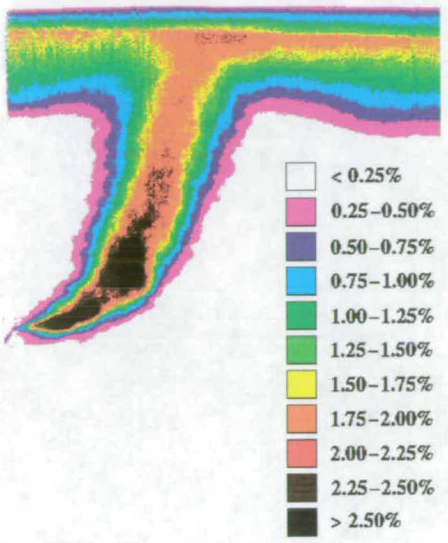

Figure 7.6: Time averaged concentration map. H=0.45m $\frac{L_Q}{Z_M}$=0.061

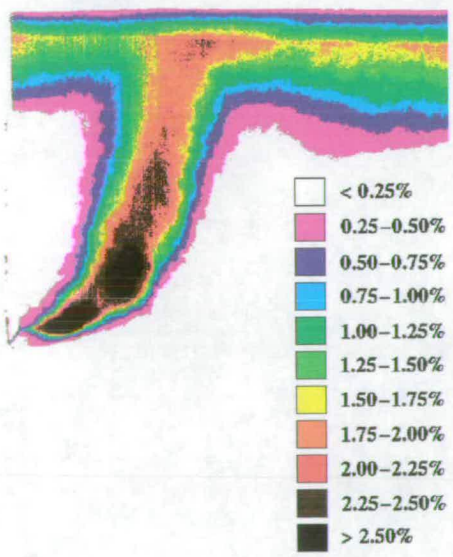

Figure 7.7: Time averaged concentration map. H=0.45m $\frac{L_Q}{Z_M}$=0.067

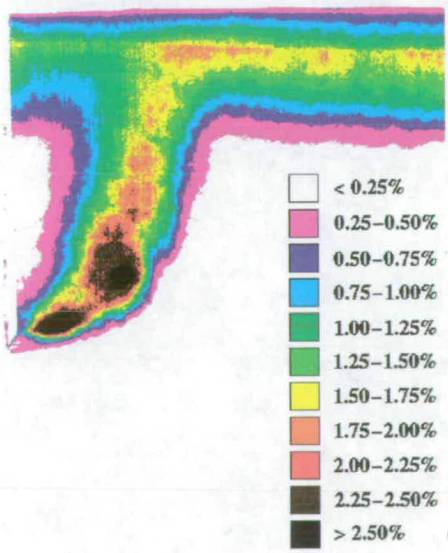

Figure 7.8: Time averaged concentration map. H=0.45m $\frac{L_Q}{Z_M}$=0.091

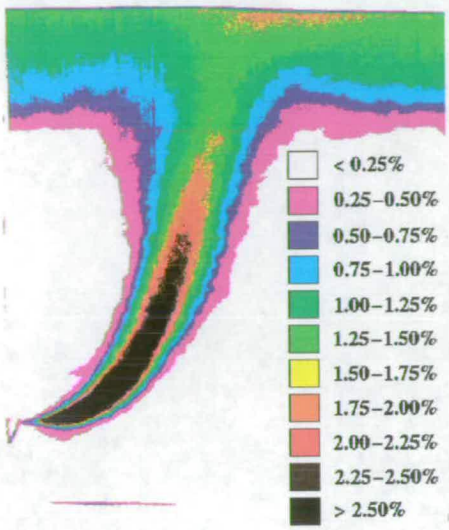

Figure 7.9: Time averaged concentration map. H=0.60m No waves

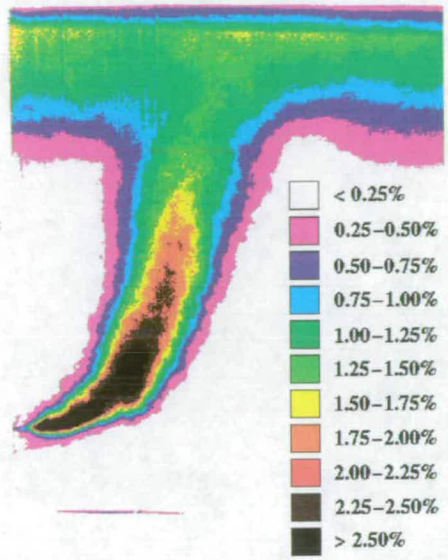

Figure 7.10: Time averaged concentration map. H=0.60m $\frac{L_Q}{Z_M}$=0.053

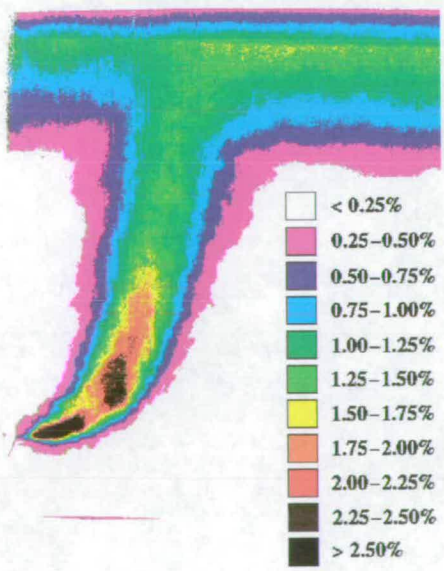

Figure 7.11: Time averaged concentration map. H=0.60m $\frac{L_Q}{Z_M}$=0.066

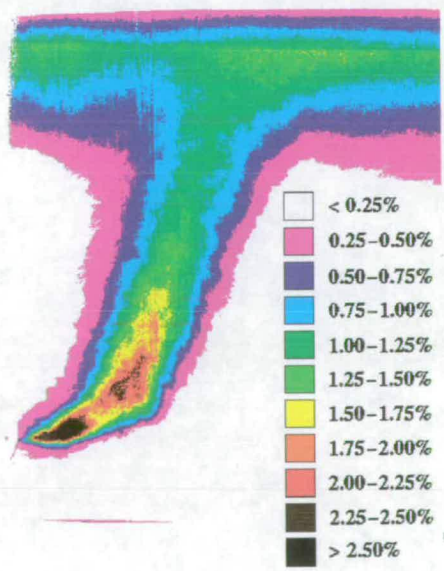

Figure 7.12: Time averaged concentration map. H=0.3m $\frac{L_Q}{Z_M}$=0.079

2, this equation is that for a pure line plume and the experimental results will only begin to tend to this equation once the individual plumes have merged but within $z = 25s$. In this case the merging point, $z = 2.5s$ equates to $\frac{z}{H} = 0.23$ and $z = 25s$ to $\frac{z}{H} = 2.4$. Figure 7.13 shows that the experimental results and the theoretical concentration show agreement from $\frac{z}{H} = 0.4$ or $z = 4.4s$, after the merging point but well within the expected agreement region.

An increase in dilution due to the effect of the waves is again shown by figure 7.13 , the greatest effect being within a fifth of the rise height. After this initial increase a region with constant or slightly increased concentration is seen before a final region in which dilution increases at a similar rate for both wave and no-wave cases.

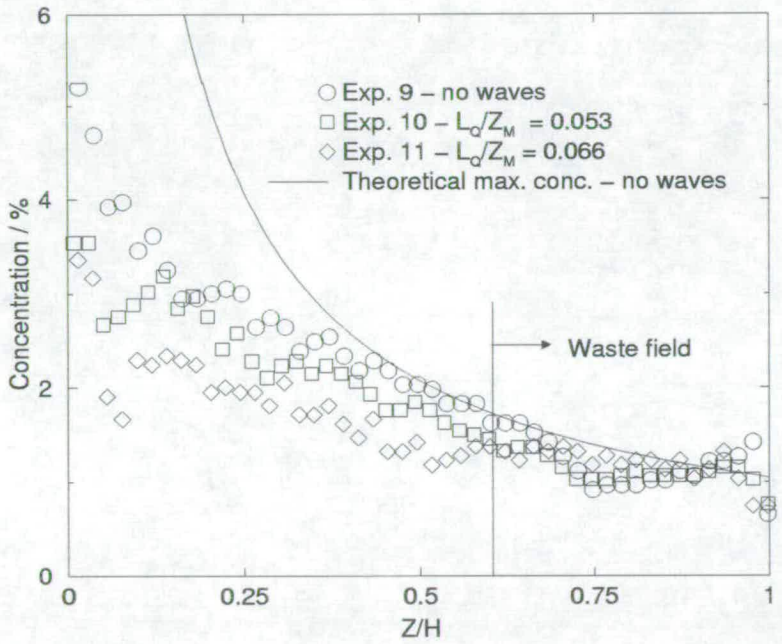

Figure 7.13: Normalised (rise height divided by discharge depth) centre line concentration.

The initial and final regions were observed by Chin who noted the discharged jets 'exploding' close to the port when the wave induced velocity opposed that of the discharge, but the plume merely being translated from side to side further above

the port [16].

Chyan and Hwung [21] though investigating a jet orientated vertically, also noted that the rise height could be divided into a number of regions. The region analogous with the initial 'exploding' region they named the 'deflection region' as a vertical jet's trajectory is deflected by the wave motion in this region. They too, then recognised a region of lower or decreased dilution as observed in the present results and noted that the increase in concentration was higher in stronger wave conditions. They named this the 'transition region' and argued that here the initial jet momentum had decayed to the extent that the jet flow was no longer significantly deflected. Indeed in the present results this increase in concentration takes place at around $2Z_M$ in the rise height, the point at which the jet momentum becomes of the order of half of the wave induced horizontal momentum. In this region the influence of the initial jet momentum has decreased to such an extent that it no longer influences the plume's trajectory and motion is solely due to the wave effect. Above this point as with the present and Chin's results they observed a 'developed region' in which the plume is translated horizontally by the wave motion and identified by a decreased rate of dilution.

The normal concentration profiles from four sections of a plume discharged into still water (experiment 9) are shown in figure 7.14. The profiles are as expected from theory; Gaussian in profile throughout the rise height. Figure 7.15 however shows profiles from a plume discharged with waves present (Experiment 4, $\frac{L_Q}{Z_M} = 0.095$). It can be seen that while initially approximately Gaussian in profile, the profile soon develops two distinct peaks.

This profile can be explained if a Gaussian profile in still water is first assumed and then the plume motion due to the wave examined. As the plume is approximately vertical for the majority of its rise height, the normal profiles are approximately horizontal and therefore only the horizontal component of the wave motion need be considered. Equation 2.35 shows that the wave induces a

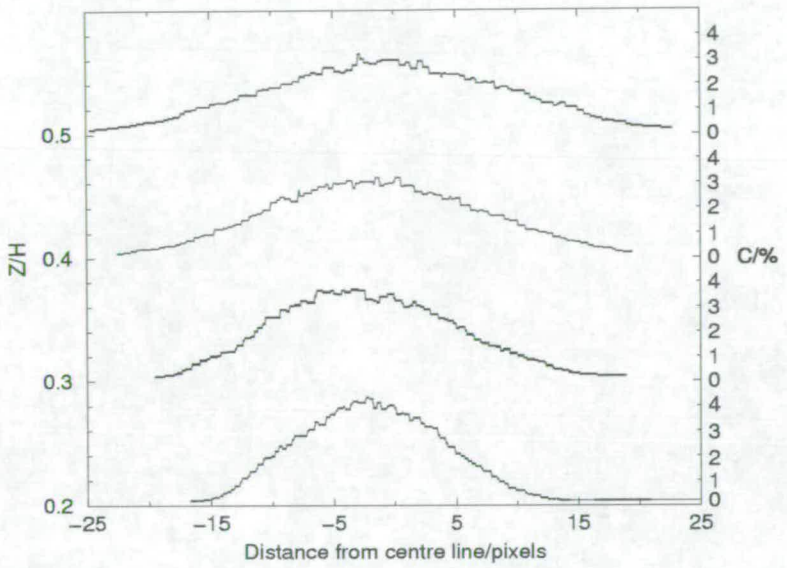

Figure 7.14: Graph showing Gaussian normal concentration profile for plume in still water.

sinusoidally varying horizontal motion in the column of water under the plume and therefore on the plume. Given a sinusoidally varying displacement the spatial distribution function for the plume can be calculated and then convolved with the Gaussian concentration profile (fig 7.16). The resulting profile is then similar to that observed experimentally, though the theoretical result shows peaks of equal magnitude while the experimental results show the right peak to be smaller. This may be explained if the trajectory of the plume is considered. While for the above analysis the plume is considered to be vertical, in the case studied the initial jet is orientated horizontally and therefore as the plume becomes vertical the fluid on the outside edge of the plume has a greater area to occupy and will therefore be more dilute. This may be seen in figures 7.1, 7.5 and 7.9 where the bands of any given concentration level are thinner on the outside edge of the plume than on the inner edge.

The double peak phenomena was only observed in the two experimental runs with the strongest wave effect, that is experiments 4 and 8, $\frac{L_Q}{Z_M} = 0.095$) and $\frac{L_Q}{Z_M} = 0.091$). This is not to say that the plumes on other runs conducted under

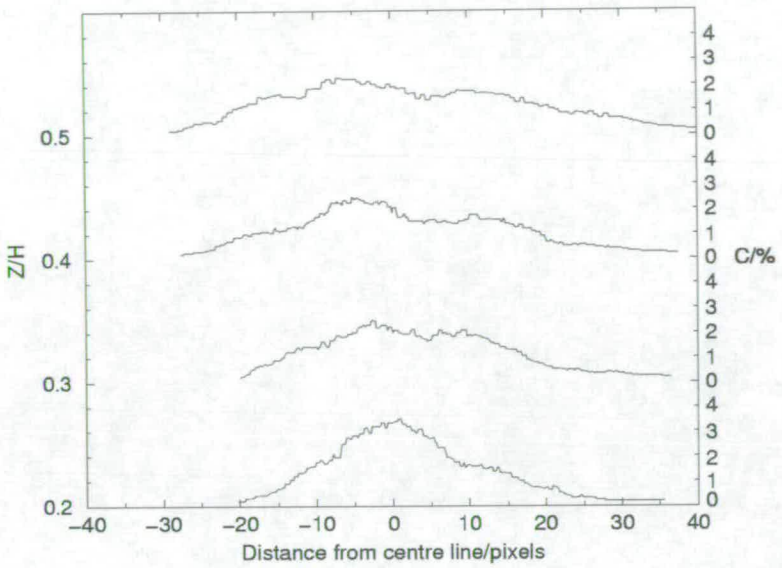

Figure 7.15: Graph showing departure from Gaussian normal concentration profile due to wave motion.

wave conditions were unaffected. A smaller horizontally induced motion, rather than resulting in two distinct peaks, will lead merely to a slight widening of the plume.

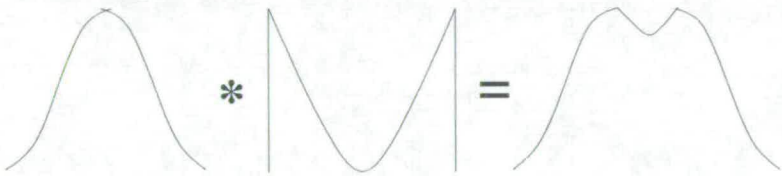

Figure 7.16: Effect of wave motion on gaussian concentration profile.

In order to quantify the effect of the waves on increasing plume dilution, a program was used to find the average increase in dilution in the region below $\frac{Z}{H} = 0.6$ between wave and no-wave cases. This region was chosen in order to omit the wastefield as in this region no further mixing with fresh water will be possible. The average increase was then plotted against $\frac{L_Q}{Z_M}$ (fig. 7.17) and with Chin's experimental data [16]. From the gradient of the line of best fit the increase in

dilution due to the effect of the waves can be written as

$$\frac{S}{S_o} = 1 + 6\frac{L_Q}{Z_M} \tag{7.1}$$

While this equation is that for the average dilution of a line plume, the $\frac{L_Q}{Z_M}$ coefficient is comparable with that for a round plume as calculated by Chin,

$$\frac{S}{S_o} = 1 + 6.11\frac{L_Q}{Z_M} \tag{7.2}$$

This does not seem unreasonable given that the greatest increase in dilution due to the wave effect occurs in the region before merging. In this initial region the discharge is in the form of a number of individual round plumes and these will each behave in the same way as that studied by Chin. After merging it has been seen that there is limited further mixing due to the effect of waves.

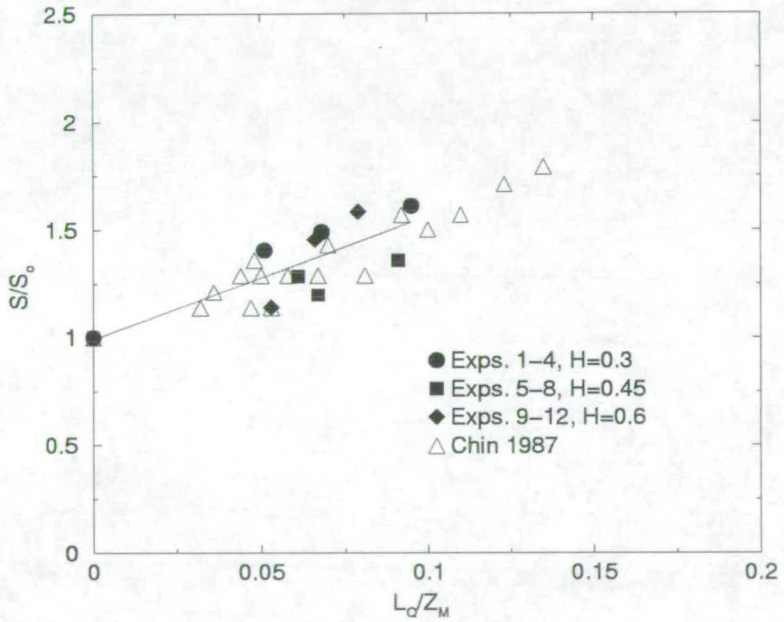

Figure 7.17: Increase in dilution against $\frac{L_Q}{Z_M}$.

The exploding effect observed by Chin also leads to a broadening of the plume most clearly seen in figures 7.1-7.4. Figures 7.18 and 7.19, non dimensional plots of plume width against rise height, show that the rate of broadening is increased

for rise height less than $2Z_M$, Chyan's deflection region. In this region the rate of broadening is 1.6 times higher than that for rise height greater than $2Z_M$, with a line of best fit gradient of 1.1×10^6 compared with a value of 0.69×10^6 in the latter developed region. As can be seen from figure 7.20, the rate of dilution in this region is of the the order of that of the no-waves case and therefore the waves are having no further effect on the plume dilution.

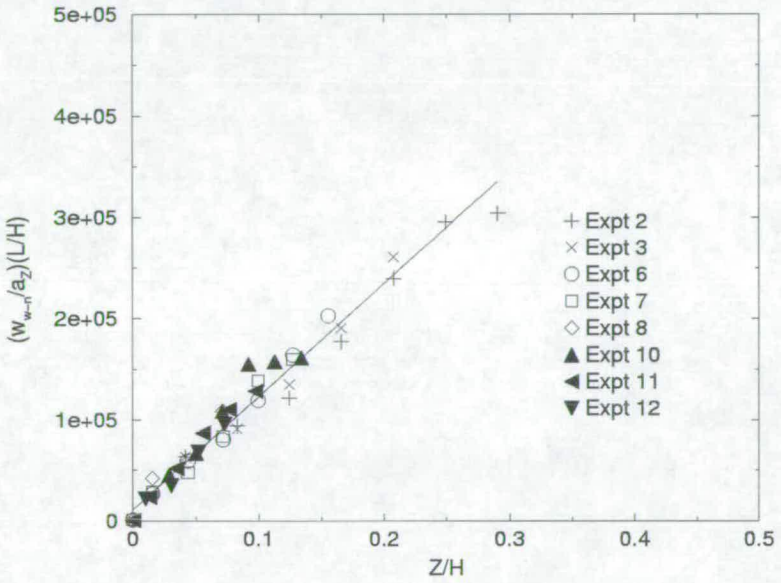

Figure 7.18: Plume width for $Z < 2Z_M$.

To identify the mechanism responsible for the increase in dilution due to wave motion, the time-averaged concentration maps for each experiment were further analysed to find the average magnitude of deviation from the time-averaged concentration value, $\frac{\overline{<C'>}}{\overline{C}}$. A low value of $\frac{\overline{<C'>}}{\overline{C}}$ would imply that there is little entrainment of fresh fluid taking place, the concentration at that point remaining fairly constant over time. For values of $\frac{\overline{<C'>}}{\overline{C}} > 1$ where the average variation from the mean is greater than the mean itself, the concentration at that point will vary greatly over time implying a greater level of entrainment of fresh fluid.

Figures 7.21-7.24 show experiments conducted using a discharge depth of 0.3m, figures 7.25-7.28 those discharged from 0.45m and figures 7.29-7.32 those from

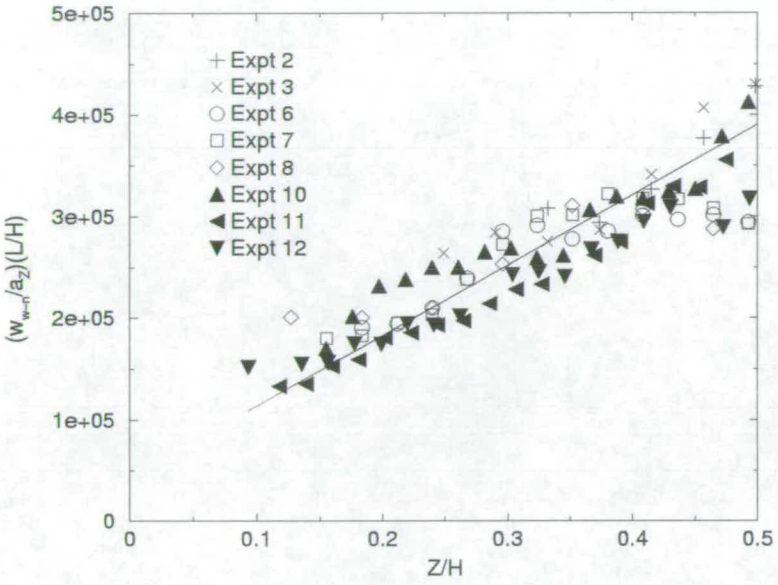

Figure 7.19: Plume width for $Z > 2Z_M$.

0.6m. As with the earlier images the first in each sequence shows a discharge into still conditions and the following three images discharges into waves with increasing amplitude.

For discharges into ambient conditions, figures 7.21, 7.25 and 7.29, it can be seen that the greatest deviations from the mean concentration values are to be found around the edges of the plume. This is to be expected as it is in these areas that the greatest volume of fresh water will be entrained by the plume. As described earlier there is a thinner layer of effluent between the plumes's core and fresh liquid on the outside edge of the plume. It is therefore unsurprising that the greatest levels of variation from the mean are to be found in this region.

Under the influence of waves, while the magnitude of the largest deviation from the average value may not greatly increase, the area over which large variations take place is greater. For example in figure 7.21 values of $\frac{\overline{<C'>}}{\overline{C}} > 1.0$ are confined to the edges of the plume, whilst under the influence of waves values of this magnitude are found closer to the core of the plume. This shows that under

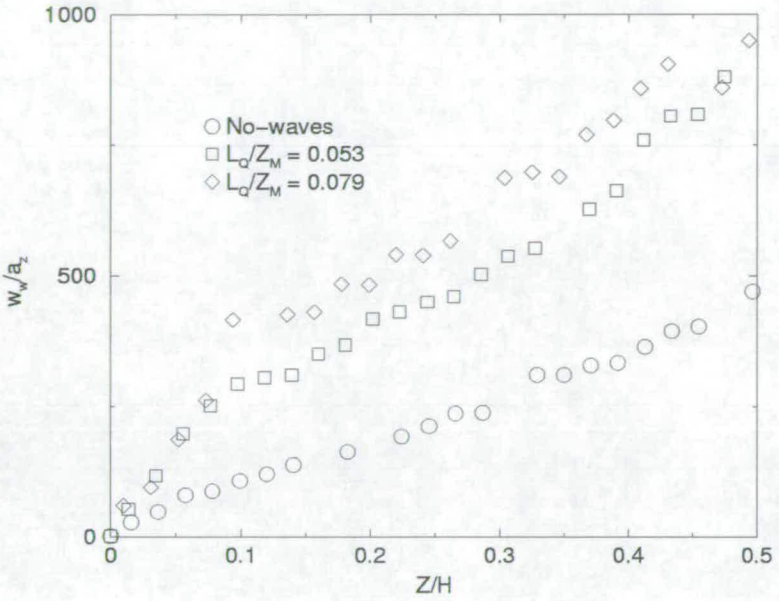

Figure 7.20: Plume width for no-wave and wave cases.

the influence of waves cleaner fluid is entrained deeper into the plume than under ambient conditions resulting in an overall increase in dilution of the plume. Again it can be seen that entrainment is greatest around the outside edge of the plume where fresh liquid may more easily be mixed deeper into the plume.

Once again the wave effect is can be seen to be greatest in lower fifth of the plume's rise height, corresponding to the area in which the plume's horizontal momentum is greater than the horizontal wave momentum. In this region waves of sufficiently large amplitude allow large variations from the mean to be found at the very core of the plume.

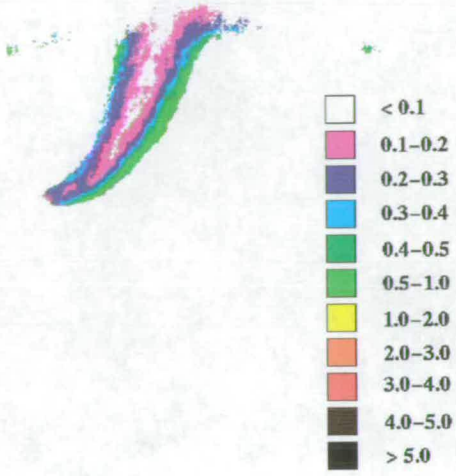

Figure 7.21: $\frac{\overline{<C'>}}{\overline{C}}$ H=0.30m No waves

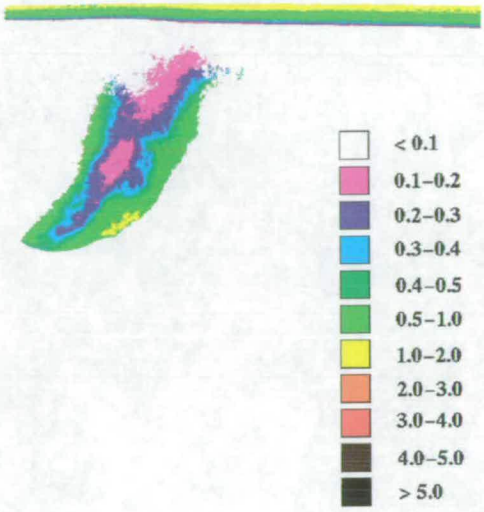

Figure 7.22: $\frac{\overline{<C'>}}{\overline{C}}$ H=0.3m $\frac{L_Q}{Z_M}$=0.051

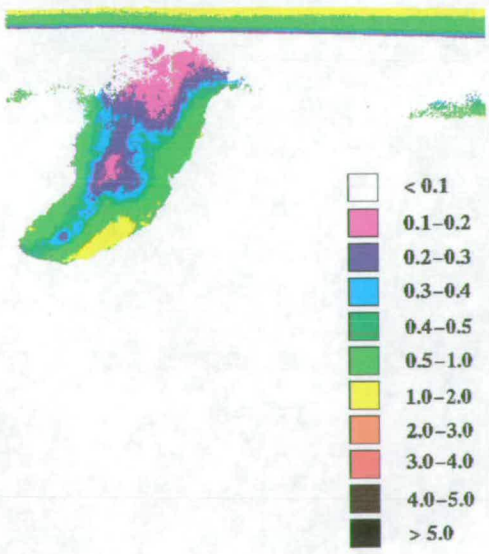

Figure 7.23: $\frac{\overline{<C'>}}{\overline{C}}$ H=0.30m $\frac{L_Q}{Z_M}$=0.068

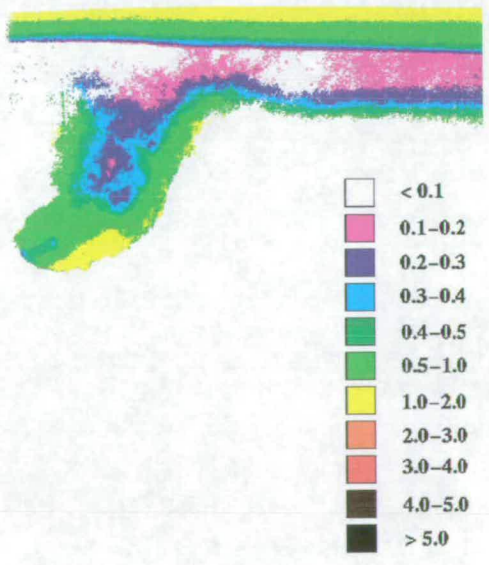

Figure 7.24: $\frac{\overline{<C'>}}{\overline{C}}$ H=0.30m $\frac{L_Q}{Z_M}$=0.095

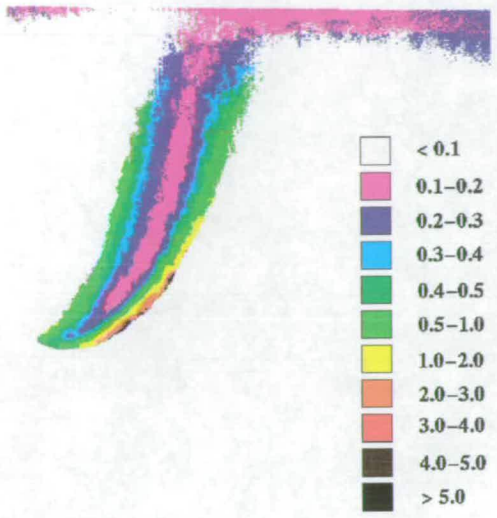

Figure 7.25: $\frac{\overline{<C'>}}{C}$ H=0.45m No Waves

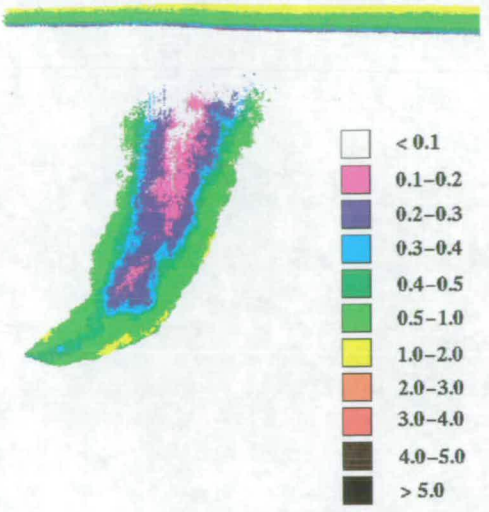

Figure 7.26: $\frac{\overline{<C'>}}{C}$ H=0.45m $\frac{L_Q}{Z_M}$=0.061

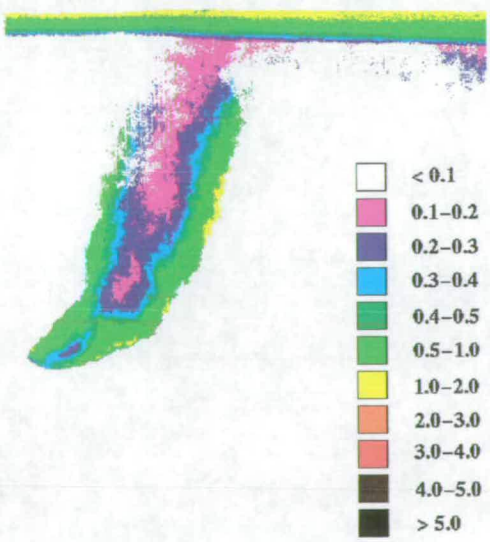

Figure 7.27: $\frac{\overline{<C'>}}{C}$ H=0.45m $\frac{L_Q}{Z_M}$=0.067

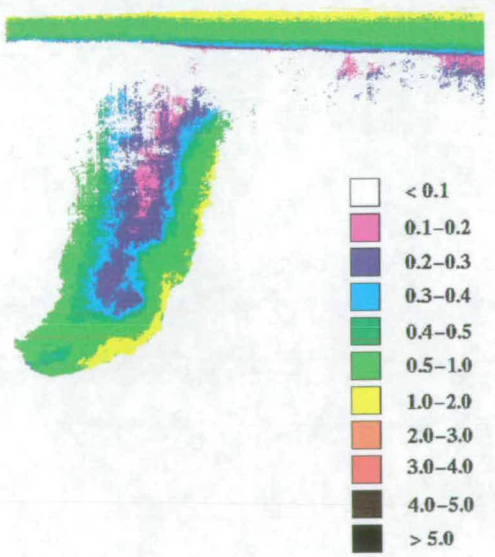

Figure 7.28: $\frac{\overline{<C'>}}{C}$ H=0.45m $\frac{L_Q}{Z_M}$=0.091

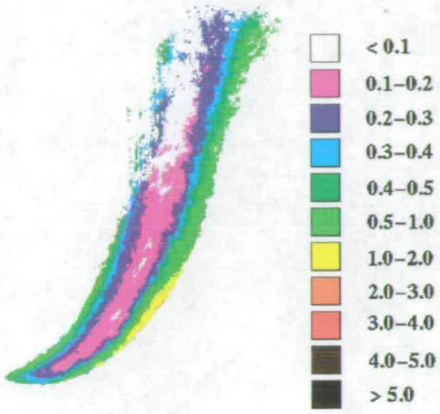

Figure 7.29: $\frac{\overline{<C'>}}{C}$ H=0.60m No waves

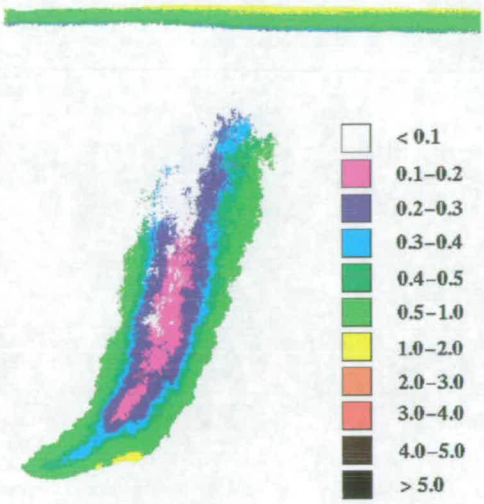

Figure 7.30: $\frac{\overline{<C'>}}{C}$ H=0.60m $\frac{L_Q}{Z_M}$=0.053

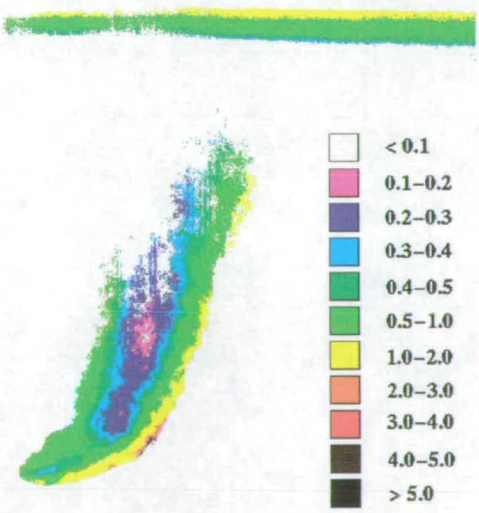

Figure 7.31: $\frac{\overline{<C'>}}{C}$ H=0.60m $\frac{L_Q}{Z_M}$=0.066

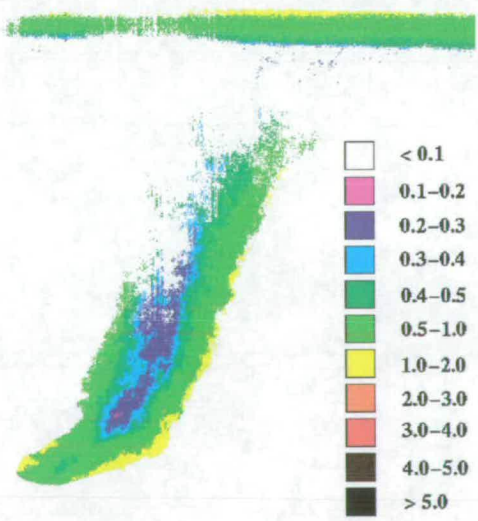

Figure 7.32: $\frac{\overline{<C'>}}{C}$ H=0.60m $\frac{L_Q}{Z_M}$=0.079

Chapter 8

Round plume results

8.1 LIF results

As with the images recorded in the line plume experiments, time averaged concentration maps were produced for each of the experimental conditions. Figures 8.1 to 8.4 show discharges from 0.3m, figures 8.5 to 8.8 discharges from 0.35m and figures 8.9 to 8.12 those from 0.4m. Again the first image in each case shows a discharge into still water and the following three images discharges into waves with increasing amplitude.

The experimental conditions in the lab in which the round plume experiments were conducted were less favourable than those in which the line plume experiments had been undertaken. The laser used was unable to produce the same level of illumination as previously and the room itself had a higher level of background light. These factors both lead to a reduction in the precision with which measurements could be taken and also on the quality of the results as a whole. However even from a visual examination of the images it can be seen that as $\frac{L_Q}{Z_M}$ increases, the area of high concentration close to the port is reduced. As the concentrations become lower, the higher background light level and reduced laser power will have greater relative effect on the measurements. Therefore some apparent increases in concentration may be seen in the body of the plume and

towards the wastefield.

The mirrored region at the top of the plume in each case is due to reflection from the lower surface of the water. In the previous experiments it had been possible to arrange the camera so that it was level with the water surface thus minimising the effect of reflections. However this was not possible to achieve with the mirror system used for the round plume experiments. As the reflections only affect the wastefield region of the images, a region outwith the main area of study this does not pose a problem. The periodic vertical striping visible on some of the images is due to a problem that occurred with the camera during some of the experiments, the dark level varying periodically across the CCD array. The resultant noise will have a greater relative affect on areas of low intensity and is therefore most noticeable in regions of low concentration such as the wastefield. While correction for the noise would be possible by filtering of the images, the region of greatest interest in the present study, that near the port and along the centreline, is least affected and correction was therefore deemed unnecessary.

From the key for the concentration maps in this chapter the decrease in level of precision obtained from the line plume experiments ($\pm 0.13\%$), to ($\pm 0.25\%$) can be seen. As previously mentioned, as well as the higher background light level, this was due to the lower light output of the laser installed for use with the red tank. This resulted in lower fluorescent intensities from the plumes. Calibration points at quarter percent intervals were not then possible, as the difference in intensity between them was too small. This could also partially account for the lack of observed wastefield on the round plume images. Another reason for this could be that the expected concentration of the wastefield due to a single round plume will be less than that for a series of merging round plumes.

Following the analysis of the results outlined in the previous chapter the centreline concentration was found for wave and no wave cases. Figure 8.13 shows the detected centreline concentrations for experiment *i*, a discharge at 0.3m depth

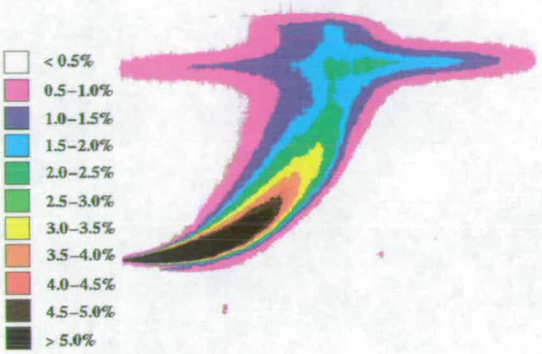

Figure 8.1: Time averaged concentration map. H=0.30 No waves

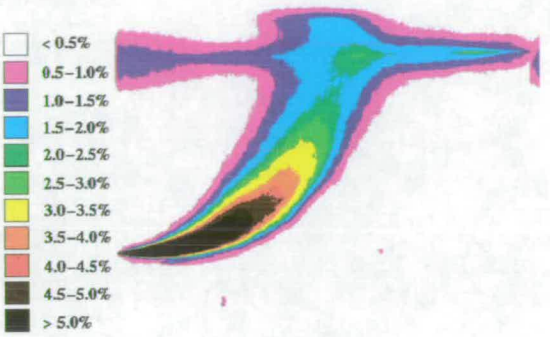

Figure 8.2: Time averaged concentration map. H=0.30 $\frac{L_Q}{Z_M}$ =0.034

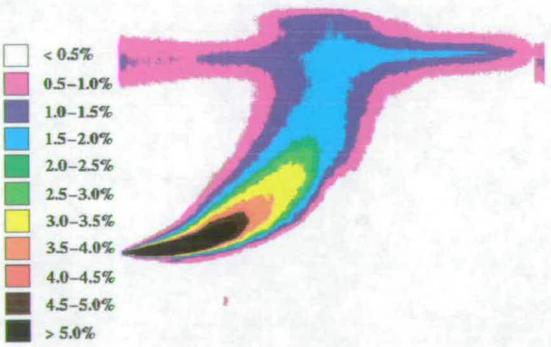

Figure 8.3: Time averaged concentration map. H=0.30 $\frac{L_Q}{Z_M}$ =0.045

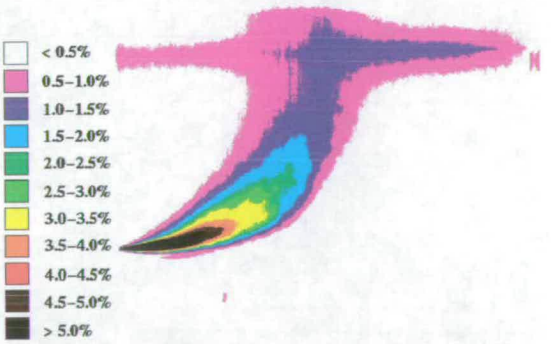

Figure 8.4: Time averaged concentration map. H=0.30 $\frac{L_Q}{Z_M}$ =0.056

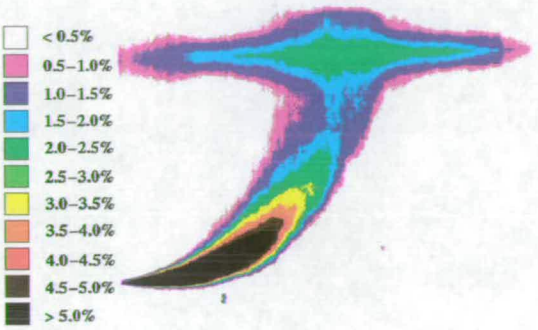

Figure 8.5: Time averaged concentration map. H=0.35 No waves

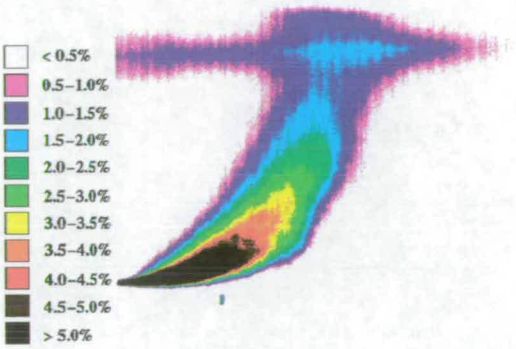

Figure 8.6: Time averaged concentration map. H=0.35 $\frac{L_Q}{Z_M}$ =0.067

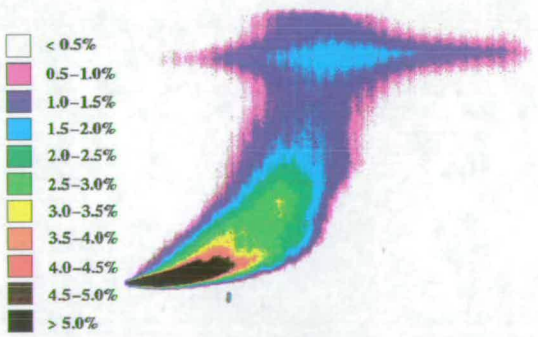

Figure 8.7: Time averaged concentration map. H=0.35 $\frac{L_Q}{Z_M}$ =0.079

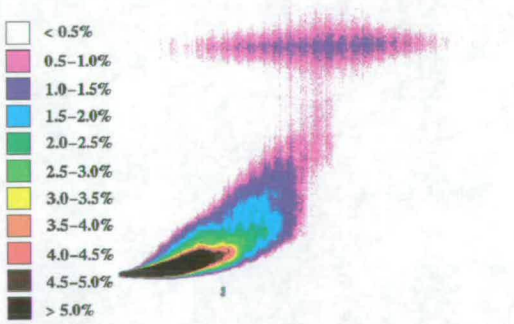

Figure 8.8: Time averaged concentration map. H=0.35 $\frac{L_Q}{Z_M}$ =0.090

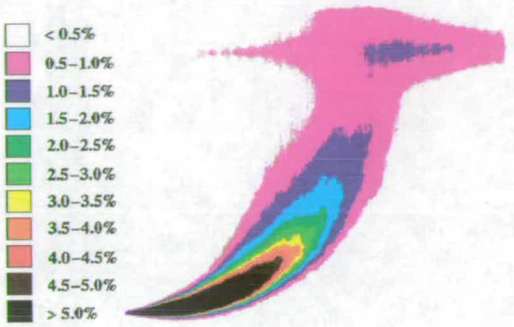

Figure 8.9: Time averaged concentration map. H=0.40 No waves

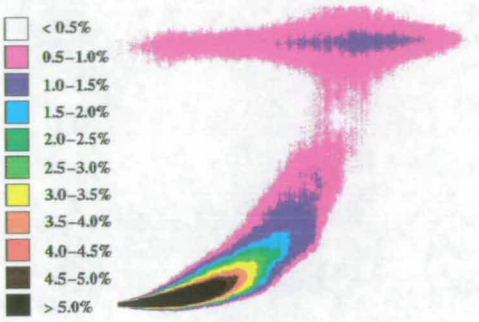

Figure 8.10: Time averaged concentration map. H=0.40 $\frac{L_Q}{Z_M}$ =0.040

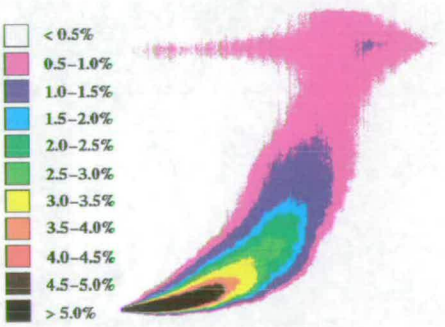

Figure 8.11: Time averaged concentration map. H=0.40 $\frac{L_Q}{Z_M}$ =0.062

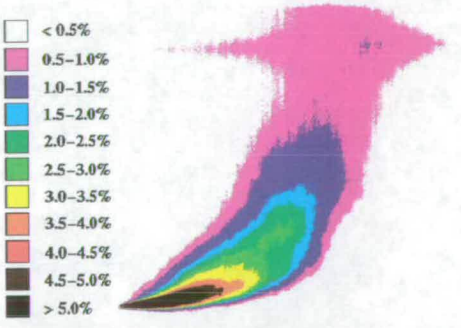

Figure 8.12: Time averaged concentration map. H=0.40 $\frac{L_Q}{Z_M}$ =0.084

into still water and experiments *x* and *xiii*, again discharges from 0.3m but into conditions of increasing wave amplitude. A plot of the theoretical maximum centreline concentration found using equation 2.26 is also shown. The theoretical curve will tend towards actual values for $\frac{z}{l_M} > 10$ which for the plume under investigation relates to a value of $\frac{Z}{H} = 1.05$, a value greater than the actual rise height. Even for the greatest depth discharge possible to be studied in the red tank, 0.4m, agreement with the theoretical curve would not be found until a depth relating to a point in the wastefield, $\frac{Z}{H} = 0.79$. Though the discharge depth is not sufficient to allow direct comparison between the theoretical and experimental results, figure 8.13 does show both lines tending to the same value.

As with the previous results the graph shows an increase in dilution due to the effect of the waves. Again an initial region of high dilution can be seen but the region of reduced or constant dilution is less apparent than with the line plume results. As with the reduction in measured wastefield, this may be due to both the reduced sensitivity of the apparatus and the lower concentrations present in a single round plume. The final region where the rate of plume dilution is comparable with the no-waves case is again seen.

Only being able to measure concentrations to the nearest half percent a meaningful comparison with Chin's earlier results is not possible. His results were obtained from just below the surface where the lowest values of plume concentration are found and the relative errors involved with the present technique are largest. Therefore the approach taken in the previous chapter has been adopted and the average dilution in the lower two thirds of the plumes' rise height found. This also allows direct comparison with the previous results. Figure 8.14 shows a plot of average increase in dilution against $\frac{L_Q}{Z_M}$ and also Chin's data. From the gradient of the line of best fit the average increase in dilution due to the effect of the waves on a round plume can be written as

$$\frac{S}{S_o} = 1 + 5\frac{L_Q}{Z_M} \tag{8.1}$$

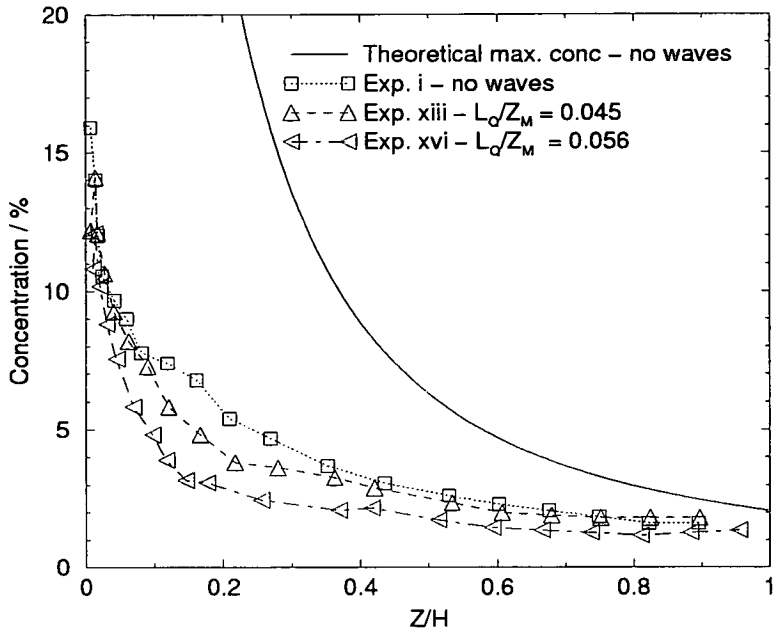

Figure 8.13: Normalised (rise height divided by discharge depth) centre line concentration.

Though this is an average value over two thirds of the plume rise it gives a similar value to Chin's results found at the boil of the rising plume,

$$\frac{S}{S_o} = 1 + 6.11\frac{L_Q}{Z_M} \tag{8.2}$$

This shows that even though the concentration maps of the round plume show a less visibly dramatic increase in dilution, due to the decrease in precision of the results, there is still a similar increase in dilution. The reason for it being slightly lower than for the line plume results may be due to the fact that these results are for an oscillating system and not under full wave conditions. While the horizontal motion has the largest influence on the discharge, the reason it was investigated, the vertical motion will still have an effect. Taking away the vertical component of the motion will therefore decrease the diluting effect on the plume.

It has been seen that the greatest wave induced increase in dilution is in the region close to the diffuser port with the rate of dilution then being similar for both wave

and no-wave cases until the bottom of the wastefield. The average increase in dilution, taken to the wastefield, should therefore give a value comparable to the increase in dilution found at the surface.

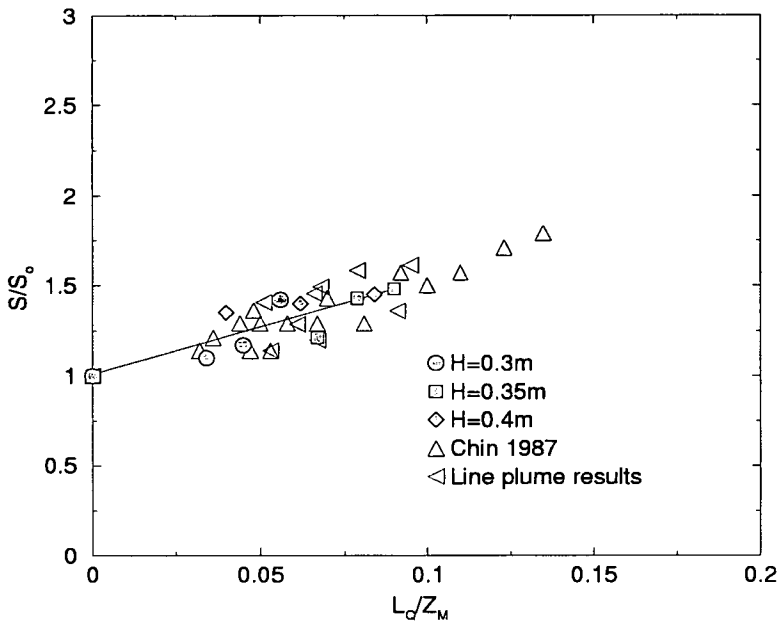

Figure 8.14: Increase in dilution against $\frac{L_Q}{Z_M}$. Line plume, round plume and Chin's 1987 results

Once again the average deviation from the mean concentration value was also found for each experiment. Figures 8.15 to 8.18 show results from experiments discharged from 0.30m, figures 8.19 to 8.22 results of discharges from 0.35m and figures 8.23 to 8.26 those from discharges at 0.40m. Features similar to those in the line plume results are again seen; the greatest entrainment being found at the edge of the plume and the wave motion acting to allow entrainment deeper into the plume itself. This effect is again found to be strongest on the outside edge of the plume.

Figures 8.27 to 8.29 show concentration maps from three slices through the plume at 0.5cm intervals. Figure 8.27 shows a slice through the central axis of the plume, figure 8.28, 0.5cm from the centre and figure 8.29, 1cm from the centre. The graph

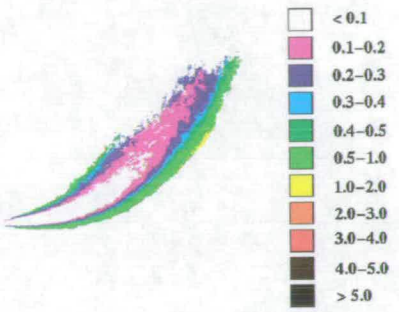

Figure 8.15: $\frac{\overline{<C'>}}{\overline{C}}$ H=0.30m No waves

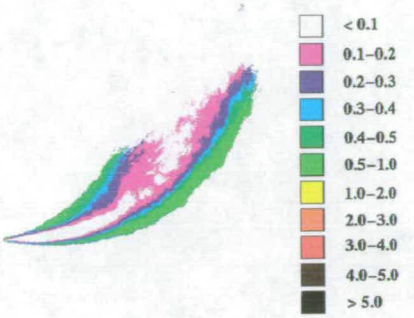

Figure 8.16: $\frac{\overline{<C'>}}{\overline{C}}$ H=0.30m $\frac{L_Q}{Z_M}$=0.034

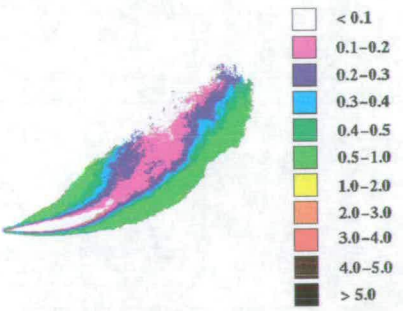

Figure 8.17: $\frac{\overline{<C'>}}{\overline{C}}$ H=0.30m $\frac{L_Q}{Z_M}$=0.045

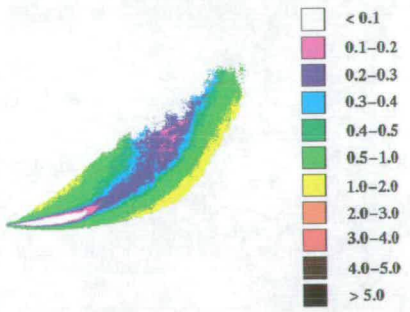

Figure 8.18: $\frac{\overline{<C'>}}{\overline{C}}$ H=0.30m $\frac{L_Q}{Z_M}$=0.056

Figure 8.19: $\frac{\overline{<C'>}}{\overline{C}}$ H=0.35m No waves

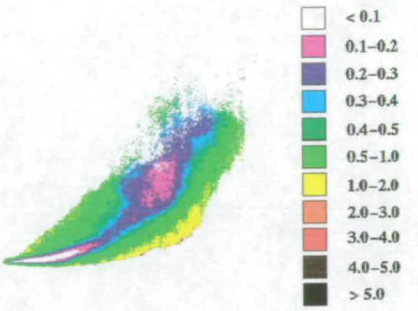

Figure 8.20: $\frac{\overline{<C'>}}{\overline{C}}$ H=0.35m $\frac{L_Q}{Z_M}$=0.067

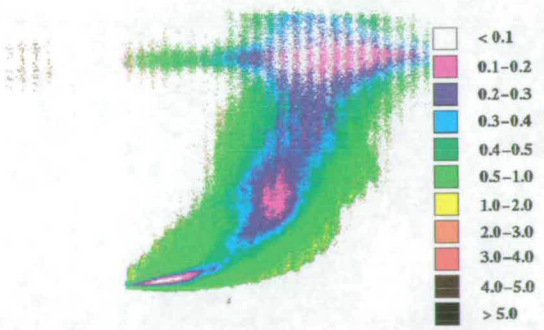

Figure 8.21: $\frac{\overline{<C'>}}{\overline{C}}$ H=0.35m $\frac{L_Q}{Z_M}$=0.079

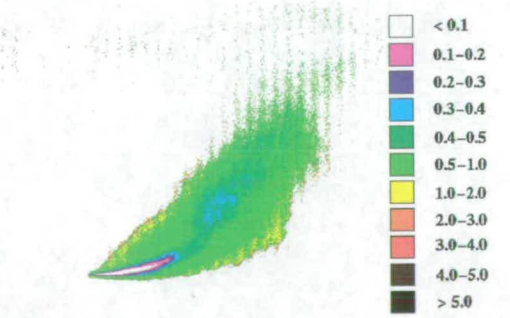

Figure 8.22: $\frac{\overline{<C'>}}{\overline{C}}$ H=0.35m $\frac{L_Q}{Z_M}$=0.090

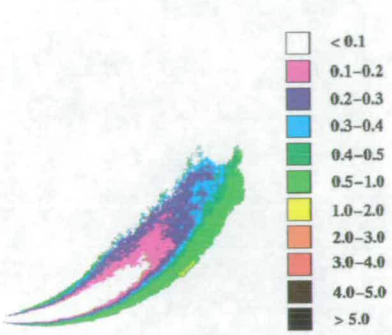

Figure 8.23: $\frac{\overline{<C'>}}{\overline{C}}$ H=0.40m No waves

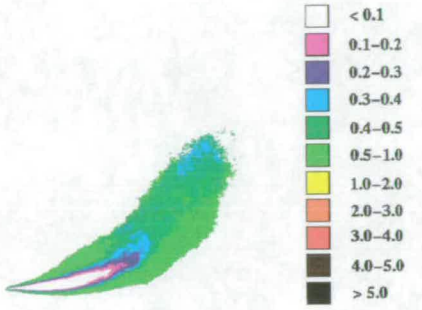

Figure 8.24: $\frac{\overline{<C'>}}{\overline{C}}$ H=0.40m $\frac{L_Q}{Z_M}$=0.040

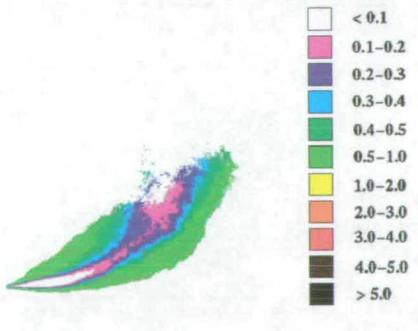

Figure 8.25: $\frac{\overline{<C'>}}{\overline{C}}$ H=0.40m $\frac{L_Q}{Z_M}$=0.062

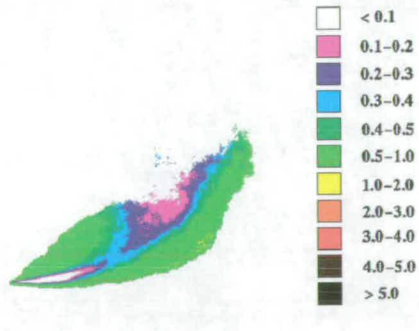

Figure 8.26: $\frac{\overline{<C'>}}{\overline{C}}$ H=0.40m $\frac{L_Q}{Z_M}$=0.084

in figure 8.30 shows normal concentration profiles taken at $\frac{Z}{H}$=0.1 from the three images allowing the variation in concentration in both the x-z and x-y planes to be seen. With further processing and extrapolation of these results it would be possible to build up a complete three dimensional concentration map of the plume.

Though experiment xxv, $\frac{L_Q}{Z_M} = 0.090$, was conducted with wave conditions almost as extreme as experiments 4 and 8 in the line plume experiments where a double peak in the normal profile was observed, no such double peak was observed in the round plume experiments. Even if a double peak were present the lower precision of the round plume experiments would not allow this to be clearly seen. As can be seen in the line plume results the peaks are separated by a 'col' less than 0.5% in concentration lower than the peaks themselves. A feature of this magnitude would not then be apparent with calibration at 0.5% intervals.

8.2 PIV results

The results of the PIV experiments undertaken on round plumes are shown in figures 8.31 to 8.38. The first figure shows a time averaged velocity map for a discharge into quiescent conditions, that is with the trolley stationary. As theoretically predicted the highest velocities are to be found at the centre of the plume, decreasing smoothly to the edges. Towards the edges of the plume the seeding concentration will be below that required for accurate PIV analysis and this results in the more randomly orientated vectors towards the edges of the plume. This effect is particularly apparent on the outside edge of the plume where the mixing is greatest.

To examine the wave effect on the plume, phase averaged velocity maps were produced for four points in the trolley's motion; at the two extremes of the motion and at the mid point of each pass. Figures 8.32 to 8.36 show velocity maps for

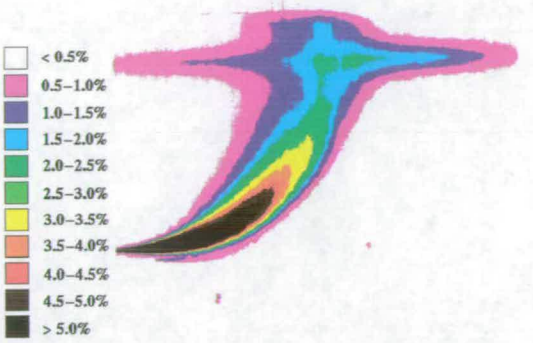

Figure 8.27: Time averaged concentration map. H=0.30m No waves. $\frac{y}{d}$=0

Figure 8.28: Time averaged concentration map. H=0.30m No waves. $\frac{y}{d}$=1.9

Figure 8.29: Time averaged concentration map. H=0.30m No waves $\frac{y}{d}$=3.7

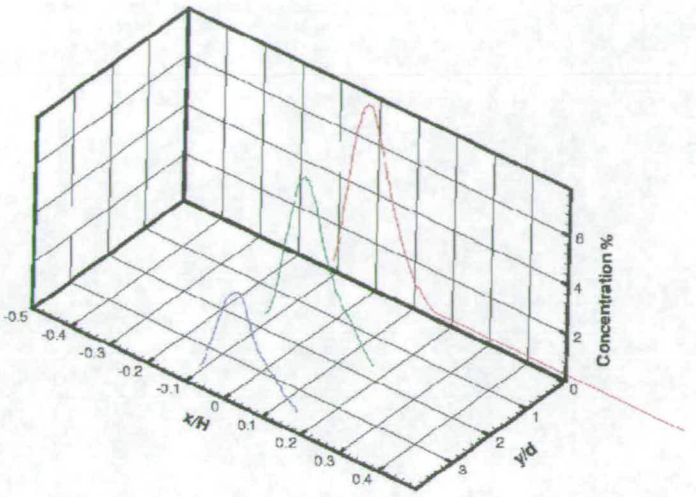

Figure 8.30: Normal concentration profiles H=0.03m $\frac{Z}{H}$=0.1 No waves. $\frac{y}{d}$=0, $\frac{y}{d}$=1.9 and $\frac{y}{d}$=3.7

the mid point of the trolley's motion as it is travelling in the opposing direction to the discharge ($\theta = 0^o$). Under the influence of small amplitude motion (fig. 8.32) the discharge soon appears to be balanced by the trolley motion with the vectors being increasingly turned to the vertical. With larger amplitude motion however (fig. 8.36) the direction of the vectors' horizontal motion is reversed. This motion will also force fresh water further into the core of the plume.

At the turning point of the trolley ($\theta = 90^o$) under small amplitude motion the vectors show little difference to those found in the unperturbed plume (fig. 8.33). In the case of the larger amplitude motion though, inertial effects will be greater and variation from the undisturbed flow can still be seen (fig. 8.37).

As the trolley again passes the mid point of its motion, but in the same direction as the discharge release ($\theta = 180^o$), deviation from the no-waves case can again be seen. With both small (fig. 8.34) and larger (fig. 8.38) amplitude motions the

vectors are swayed further towards the horizontal in the direction of the discharge, the effect being greatest under the influence of the larger motion.

Reaching the second turning point ($\theta = 270°$) the vectors in the plume under small amplitude motion again return almost to the no-wave configuration (fig. 8.35) while inertial effects are again seen under the effect of the larger amplitude motion (fig. 8.39).

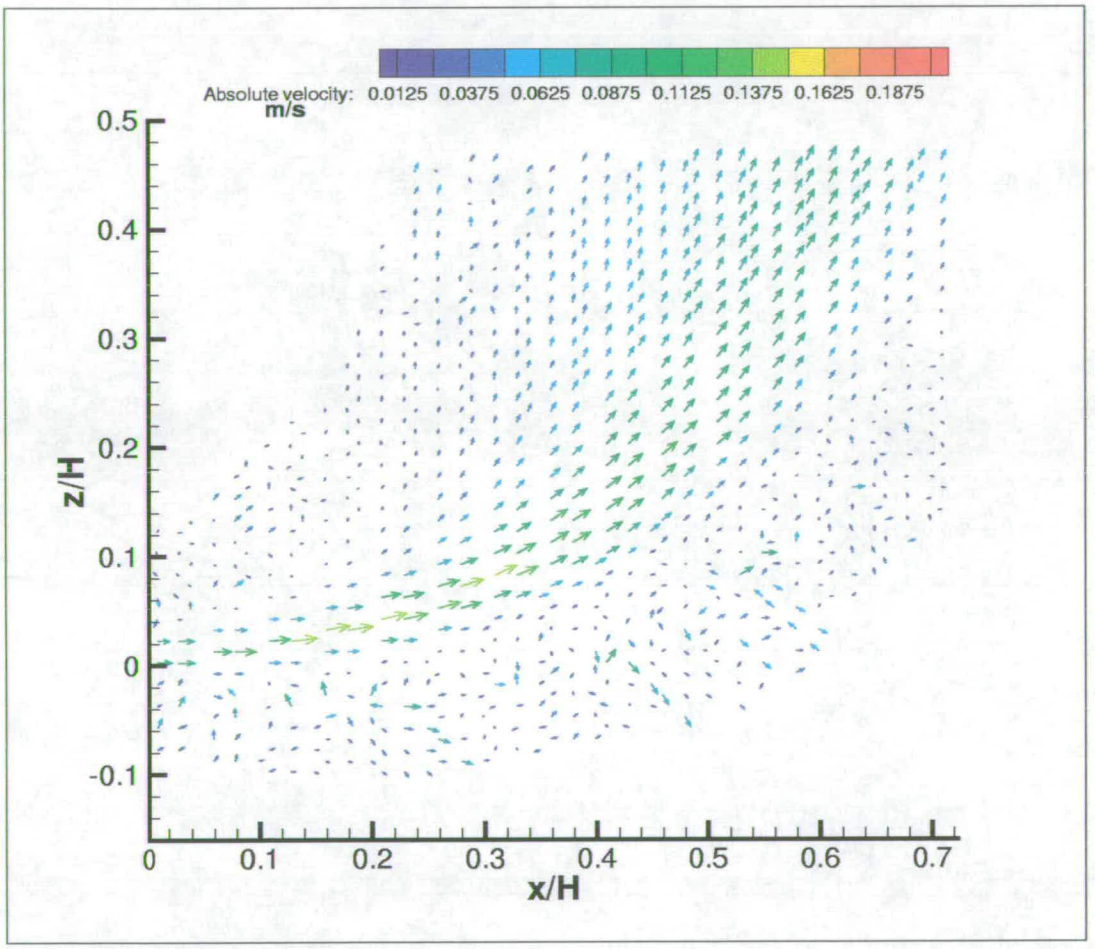

Figure 8.31: Phase averaged velocity map for plume released from stationary trolley. H=0.40m No waves

While the PIV results presented give a general overview of the motion of fluid

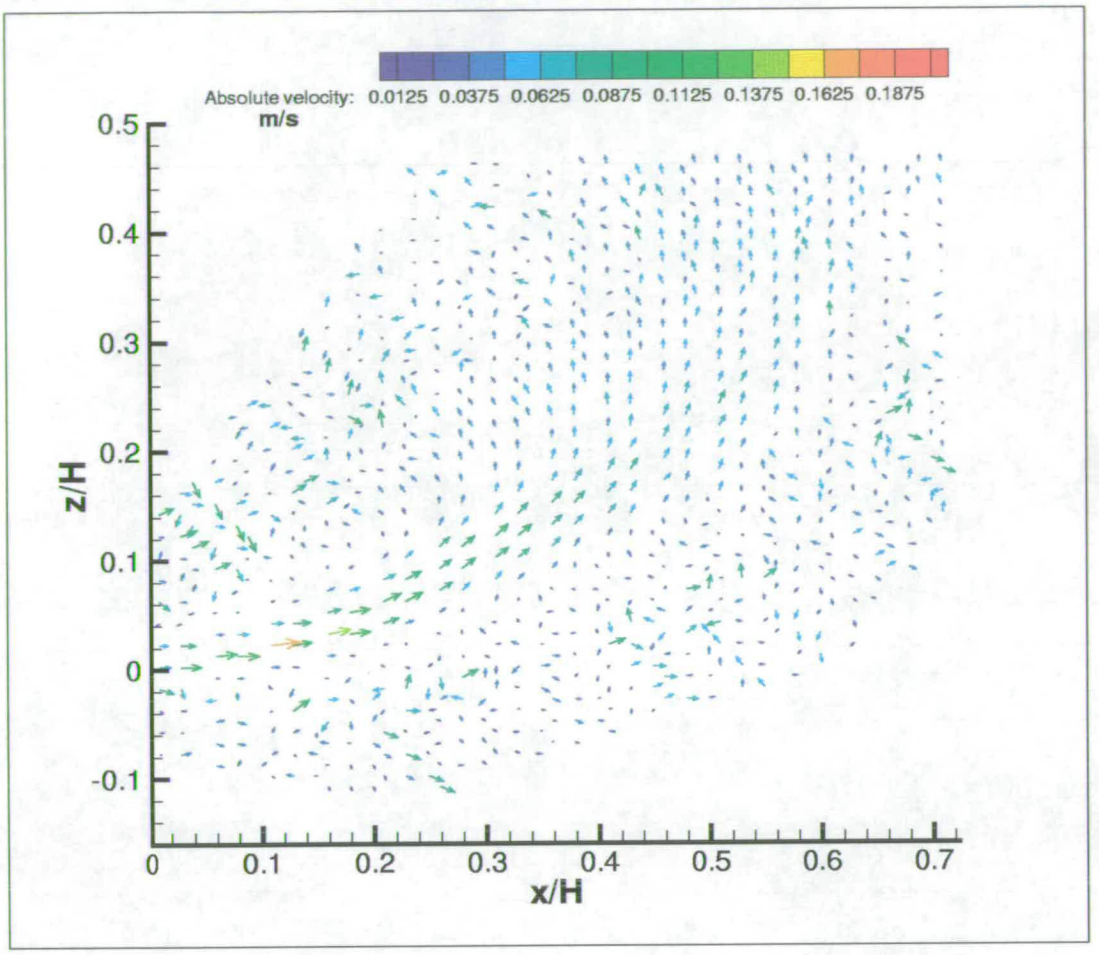

Figure 8.32: Phase averaged velocity map H=0.40m $\frac{L_Q}{Z_M} = 0.040, \theta = 0^o$

within the plume there is much scope for enhanced use of the technique in this application. Suggestions for improvements are outlined in the following chapter.

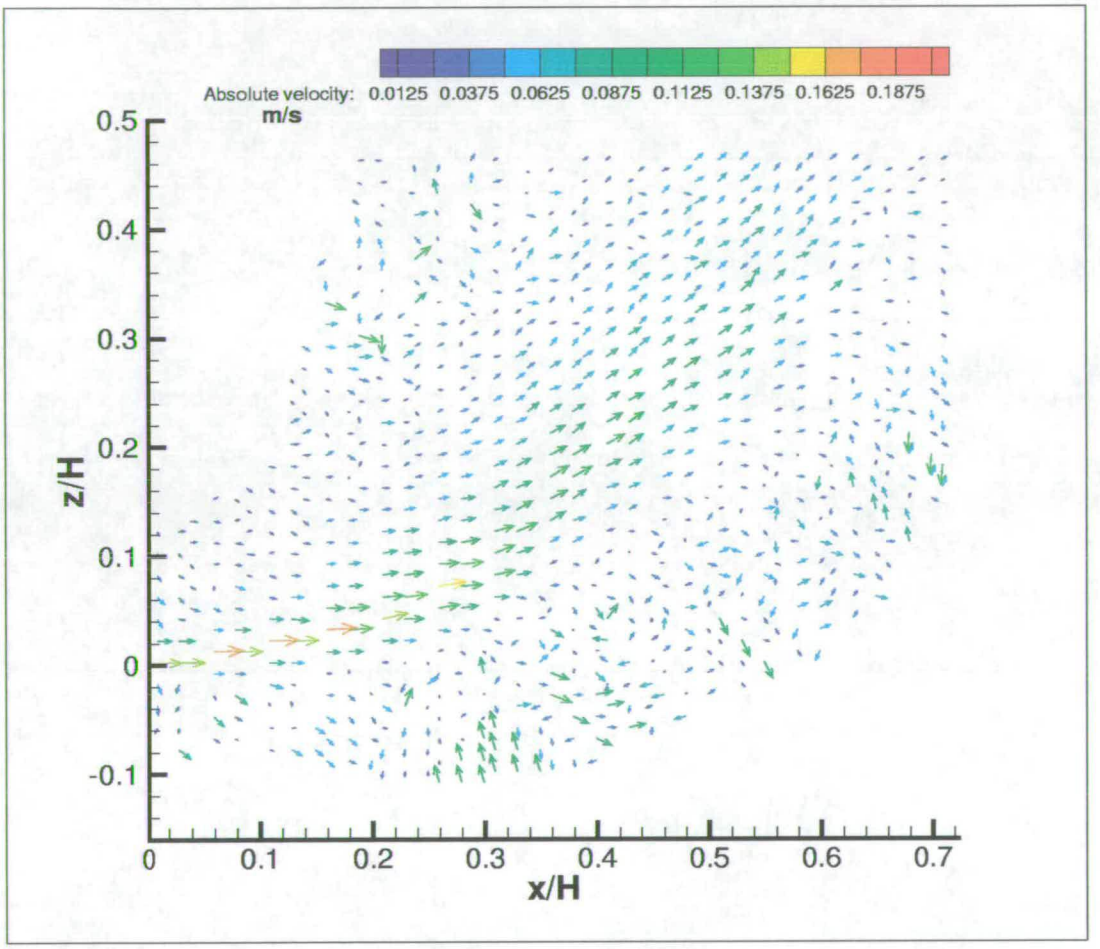

Figure 8.33: Phase averaged velocity map H=0.40m $\frac{L_Q}{Z_M} = 0.040, \theta = 90^o$

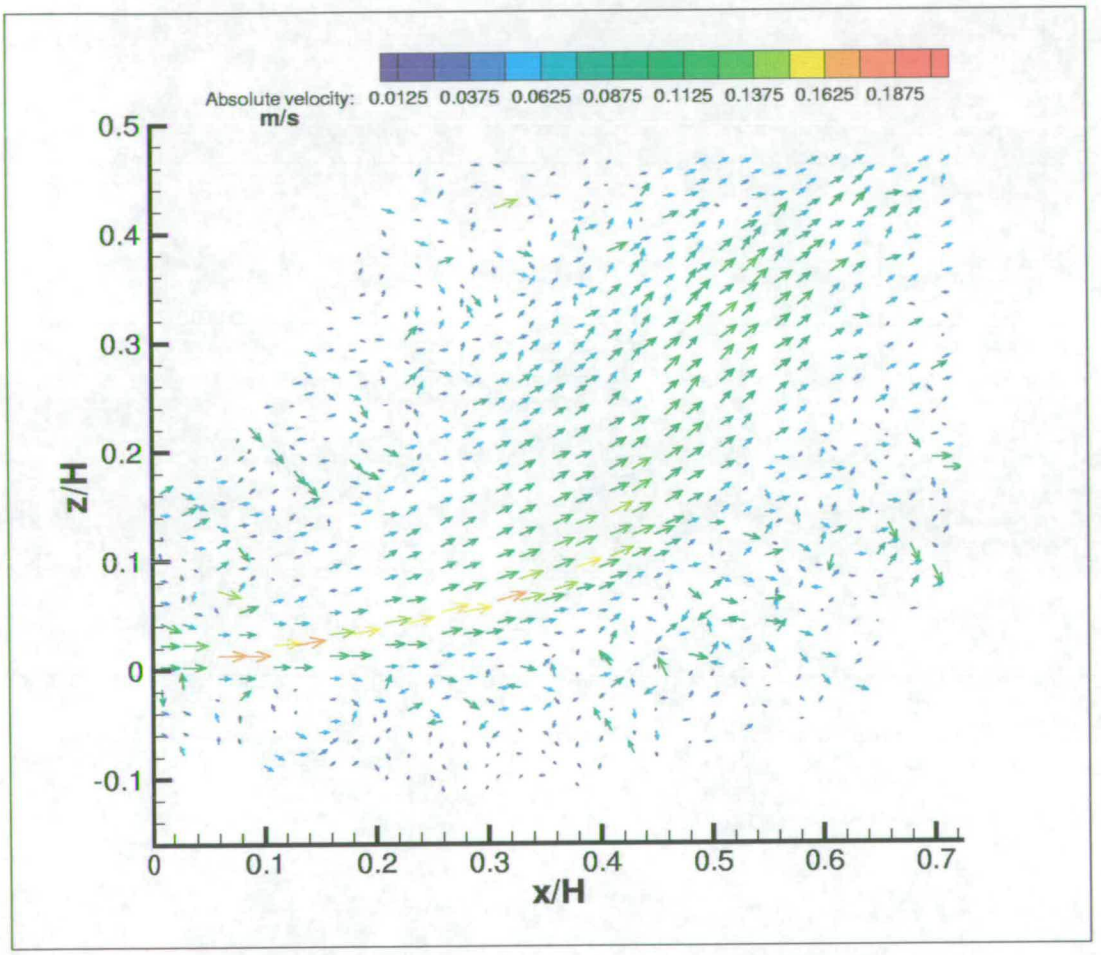

Figure 8.34: Phase averaged velocity map H=0.40m $\frac{L_Q}{Z_M} = 0.040, \theta = 180^o$

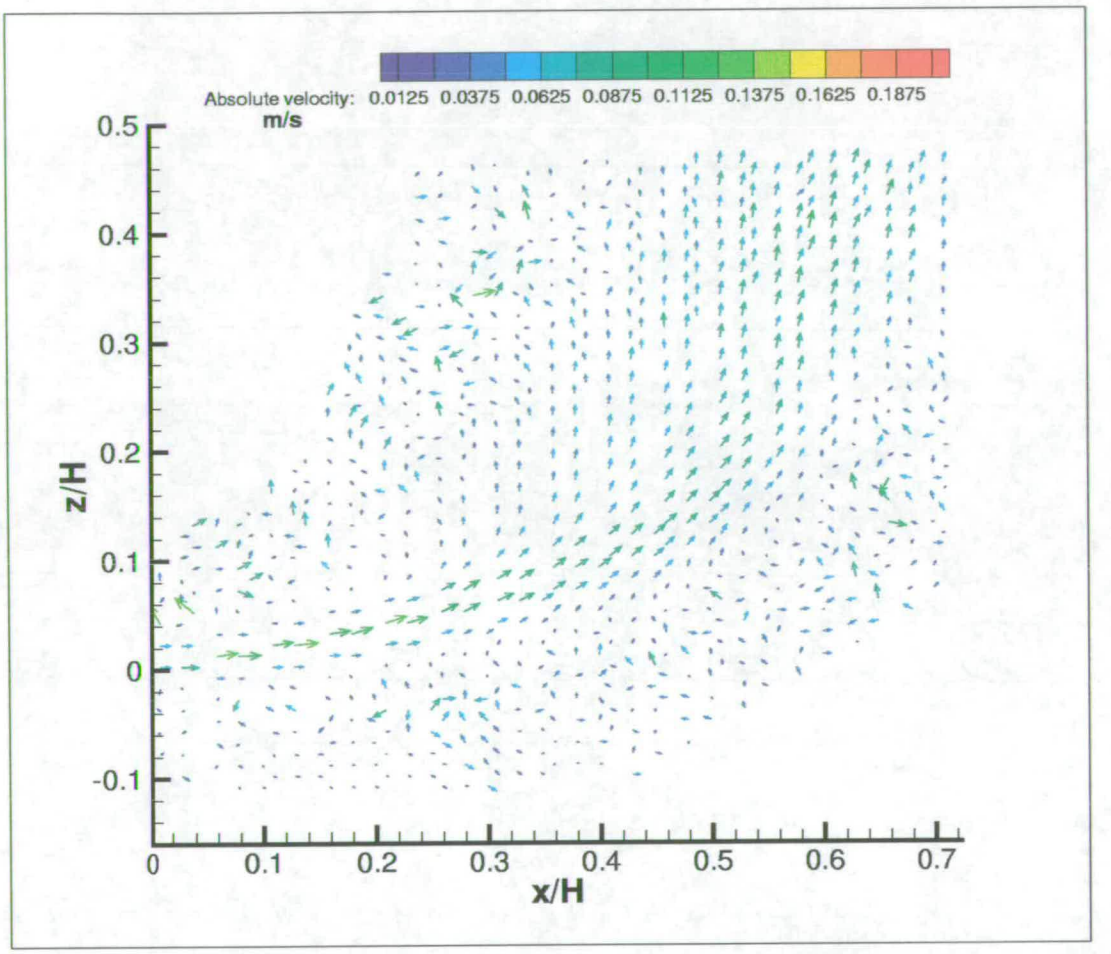

Figure 8.35: Phase averaged velocity map H=0.40m $\frac{L_Q}{Z_M} = 0.084, \theta = 270^o$

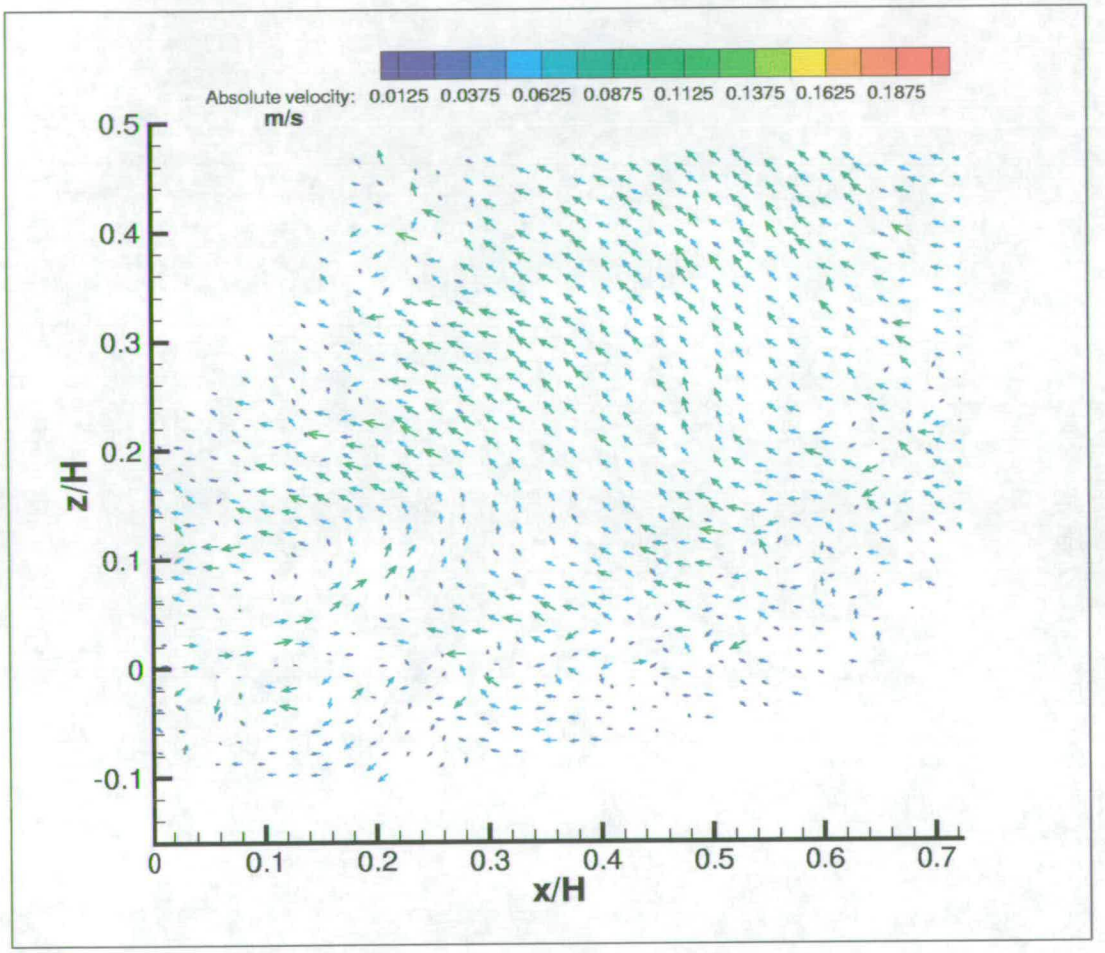

Figure 8.36: Phase averaged velocity map $\frac{L_Q}{Z_M} = 0.084, \theta = 0^o$

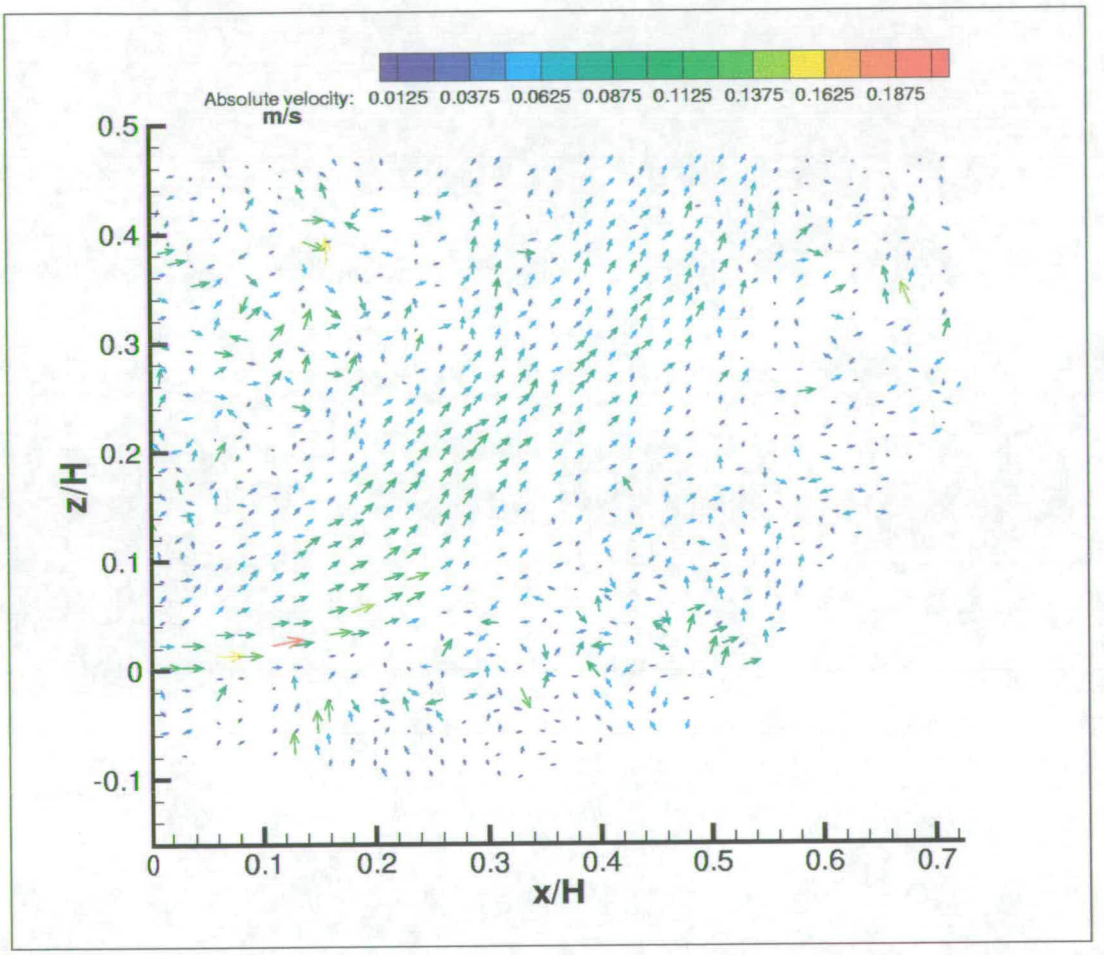

Figure 8.37: Phase averaged velocity map $\frac{L_Q}{Z_M} = 0.084, \theta = 90^o$

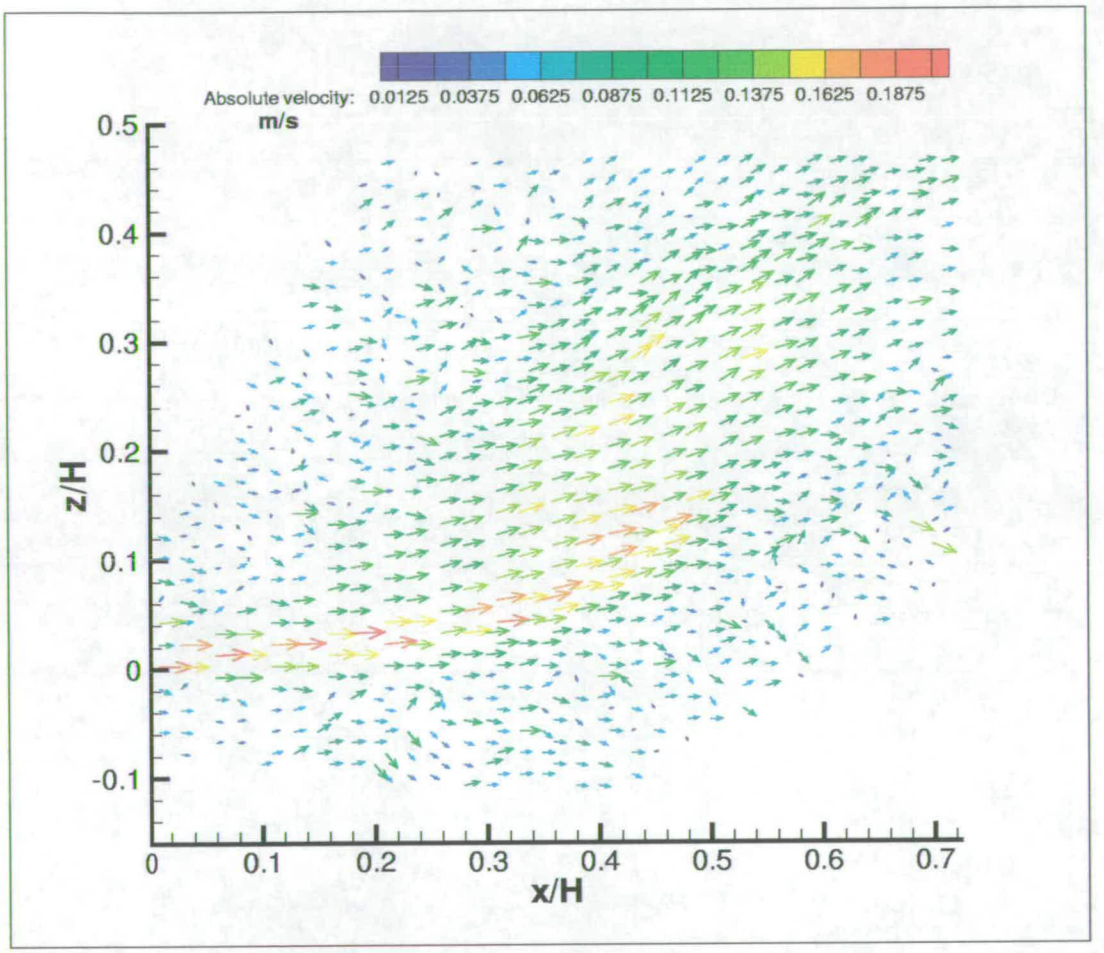

Figure 8.38: Phase averaged velocity map $\frac{L_Q}{Z_M} = 0.084, \theta = 180^o$

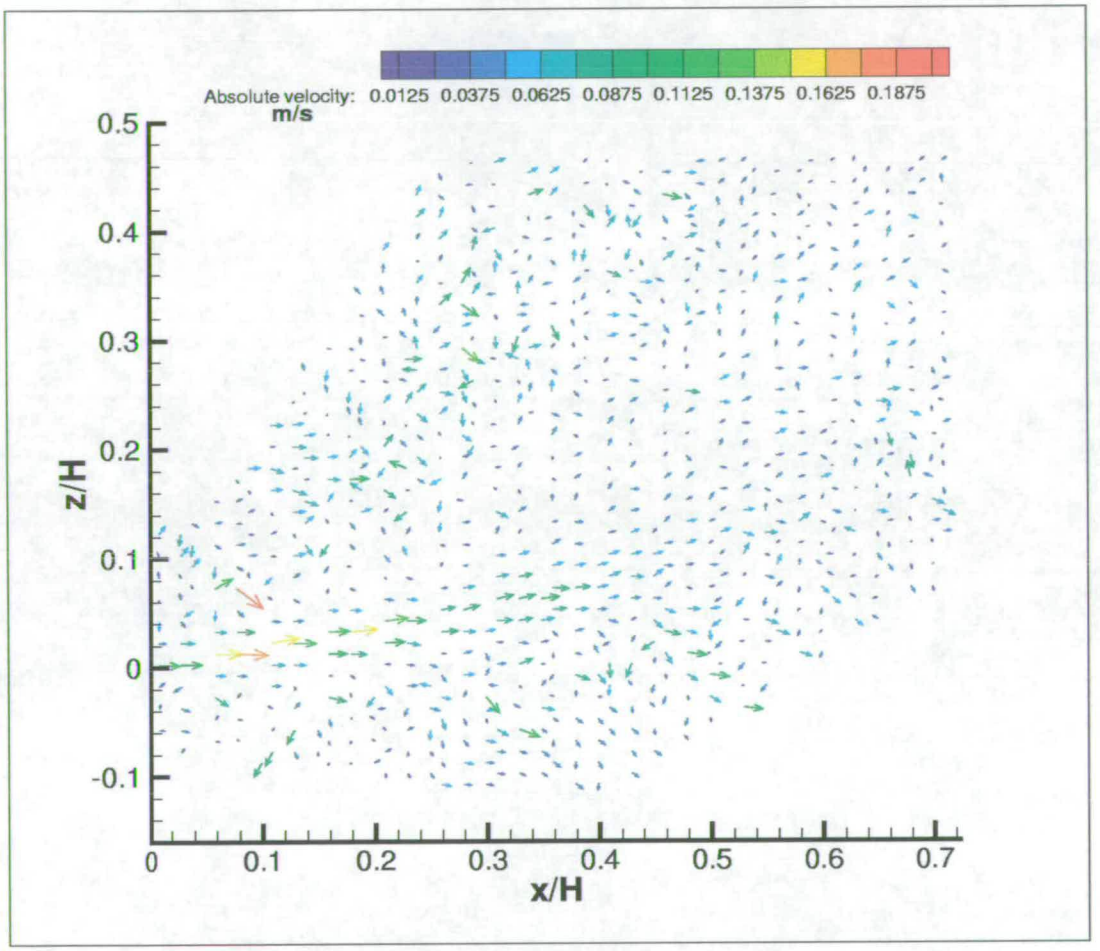

Figure 8.39: Phase averaged velocity map $\frac{L_Q}{Z_M} = 0.084, \theta = 270^o$

Chapter 9

Conclusion

Using an LIF technique it has been shown that under wave conditions of the type present at the sites of outfalls, the dilution of the discharged line plume can be increased by wave effects. The full field nature of the technique allowed not only the increase in dilution to be measured but also allowed the region in which the increase takes place to be clearly identified.

The average increase in dilution of the line plume was found to be similar to the increase in surface dilution reported by other researchers studying round plumes. This is to be expected as the greatest increase in dilution was found to be in the region near to the port and before individual plumes had merged. In this region, where the plume's horizontal momentum is still greater than that of the wave induced motion, a 'spraying' or 'exploding' of the plume is seen. After this point, as the plume's momentum decreases to half that of wave motion, the plume is merely oscillated by the wave motion and plume dilution is comparable to that of a plume released into quiescent conditions. Examination of the average deviation in concentration from that of the mean showed that the wave motion allows entrainment of fresh water deeper into the core of the plume than possible in still conditions, resulting in higher dilutions.

LIF concentration measurements were also made of round plumes released into

still and simulated wave conditions. Increases in plume dilution due to wave effects were found to be comparable with results published by other researchers demonstrating that the simulated conditions emulated actual wave conditions sufficiently well to be used in studies of this type. Again the region where the greatest increase in dilution takes place was identified and entrainment of clean water further into the plume found under the influence of wave motion. Preliminary PIV velocity measurements of the round plume were also made and general observations about velocities within the plume recorded. A method for obtaining three dimensional concentration maps of the round plume was also outlined.

9.1 Technical improvements

From the round plume results it can be seen that the quality of LIF results is greatly dependent on the light source being sufficiently intense. While the addition of further quantities of dye can be used to increase the fluorescent intensity, this will also increase attenuation of the laser light sheet. In the most extreme circumstances the sheet may be absorbed before the water surface is reached. A bright light source and low dye concentration is therefore preferable to a less intense light source and greater dye concentration. With an insufficiently bright light source the difference in intensity between concentrations also becomes less distinct, reducing the precision of the measurement. A more intense light source such as that used for the earlier work would therefore be required for any further experiments.

In determining the correct dye concentration for use in the experiments a very fine line had to be drawn between sufficient illumination and overloading the camera. If overloading takes place on any of the instantaneous images then any time averaged image made from them will not be a true, time averaged image. A 12-bit camera with 4096 grey levels rather than the 8-bit camera used would allow much greater scope for more precise concentration measurements to be

made without overloading.

While time averaged LIF results have been presented it would be interesting to produce phase averaged concentration maps for different phases of the wave motion. This would provide greater insight into the effect of the wave motion on the plume. In order to take images at a given phase of the wave motion a triggerable camera such as the PCO camera used for the PIV measurements would be needed. The camera could then be triggered by the wave maker at the appropriate phase of its motion.

Improvements to the PIV results could possibly be made by seeding the receiving water as well as the discharge. In this way the problem of low seeding densities at the edges of the plume could be overcome allowing better data to be collected from the edges of the plume. This would allow further analysis of the PIV results in this important area.

In this study the PIV and LIF experiments were conducted separately with the disadvantage that it is not the same plume under study each time. Combined LIF and PIV systems are now available [39] allowing simultaneous LIF and PIV images to be taken of the same plume. Combined with this is the possibility of measuring out of plane velocity components with a more recent PIV system [39]. By using such a system in conjunction with the method of moving the light sheet laterally through the flow under study, it would be possible to produce fully three dimensional velocity and concentration maps of a plume interacting with wave motion. This would allow a much fuller study of the wave/plume interaction.

Though a method for producing three dimensional concentration maps has been shown, only basic results from this work have been presented. Further development is still necessary on software to process data of this type to allow further results to be taken from it. Development of the LIF analysis programs is also required to allow the processing of the PIV data in the same way, allowing for example centreline detection.

9.2 Further study

With some of the improvements highlighted above made to the experimental apparatus, the present research could be continued along a number of lines:

It has been seen that the increase in dilution of the plume is greatest when the plume momentum is of the order of the wave induced momentum. As the point at which this happens will depend on the discharge's transition from a jet to a plume, an investigation into the effect of varying the Froude number of the discharge on the plume dilution would be a useful study. It may be that varying the Froude number of a discharge to increase the dilution through wave effects may be more economically viable than construction of a longer or more elaborate outfall. Coupled to this could be an investigation into the angle at which the effluent is discharged into wave conditions, Chyan and Hwung having found that a vertical discharge of a round plume leads to greater dilution than a horizontal discharge [21].

As previously mentioned an LIF study of a plume at different phases of the wave motion would prove useful in studying the greater entrainment of fresh fluid into the plume under wave motion. There is also scope for further study of the wave/plume interaction using PIV. The results presented attempted to cover as large a region of the plume as possible with the resultant loss of spatial resolution. A closer study of areas such as the outside edge of the plume close to the port could yield interesting results.

List of publications

J.M. Buick, A. Shawcross and C.A. Greated. Lattice Boltzmann simulations of fluid plumes. 11^{th} Scottish Fluid Mechanics meeting, June, 1998, Edinburgh.

D.B. Sharp, A. Shawcross and C.A. Greated. Effect of surface waves on buoyant plumes. 11^{th} Scottish Fluid Mechanics meeting, June, 1998, Edinburgh.

D.B. Sharp, A. Shawcross and C.A. Greated. LIF measurement of the effect of surface waves on buoyant plumes. In proceedings of Laser anemometry advances and applications, September, 1999, Rome.

D.B. Sharp, A. Shawcross and C.A. Greated. LIF measurement of the effect of surface waves on turbulent, buoyant plumes. submitted to Experiments in Fluid Dynamics, October 2000.

Also work contained within:
C.A.Greated et al. Boundary effects on wastewater discharges. Final report. EPSRC Grant GR/K85797

Bibliography

[1] P.J.W. Roberts. Sea outfall lecture notes. In *Short Course in Disposal of Effluents in Aquatic Environment. Uni. of Porto*, 1998.

[2] Fisher et al. *Mixing in Inland and Coastal Waters.* Academic Press, 1979.

[3] E.J. List. Turbulent jets and plumes. *Ann. Rev. of Fluid Mechanics*, 14:189–212, 1982.

[4] P.J.W Roberts. Jets and plumes and ocean outfall design. In P.A. Davies and M.J. Valente Neves, editors, *Recent research advances in the fluid mechanics of turbulent jets and plumes*, pages 441–464. Kluwer Academic Publishers, 1994.

[5] P.N. Papanicolaou and E.J. List. Investigations of round vertical turbulent buoyant jets. *J. Fluid Mech.*, 195:341–391, 1988.

[6] P.N. Papanicolaou and E.J. List. Large-scale structure in the far field of buoyant jets. *J. Fluid Mech.*, 209:151–190, 1989.

[7] T.S. Durrani and C.A. Greated. *Laser systems in flow measurement.* Plenum, 1977.

[8] P.J.W. Roberts and G. Toms. Ocean outfall system for dense and buoyant effluents. *J. Env. Eng.*, 114:1187, 1988.

[9] P.J.W Roberts and W.H. Snyder. Hydraulic model study for boston outfall. i: Riser configuration. *J. Hydraulic. Eng.*, 119:970–987, 1993.

[10] M.S. Isaacson R.C.Y. Koh and N.H. Brooks. Plume dilution for diffusers with multi-port risers. *J. of Hydraulic Eng.*, 109:199–220, 1983.

[11] H. Shuto and L.H. Ti. Wave effects on buoyant plumes. In *Proc. 14th Coastal Eng. Conf. Copenhagen*, pages 2199–2208, 1974.

[12] A.M. Ger. Wave effects on buoyant jets. In *Proc. 8th Congress Int. Assoc. Hydraulic Res.*, pages 295–300, 1979.

[13] C. Çiray and A.M. Ger. On some problems of the discharge of cooling water from nuclear power stations. Technical report, Hydraulics lab., Middle East Technical University, 1977.

[14] T-L. Chan and J.F. Kennedy. Turbulent nonbuoyant or buoyant jets discharged into flowing or quiessent fluids. Technical Report 140, IIHR, 1972.

[15] N.M. Ismail and R.L. Wiegel. Opposing wave effect on momentum jets spreading rate. *J. Waterway, port, coastal and ocean engineering*, 109:465–483, 1983.

[16] D.A. Chin. Influence of surface waves on outfall dilution. *J. of Hydraulic Eng*, 113:1006–1018, 1987.

[17] D.A. Chin. Model of buoyant-jet-surface-wave interaction. *J. Waterway, port, coastal and ocean engineering*, 114:331–345, 1988.

[18] L.N. Fan and N.H. Brooks. Numerical solutions of turbulent buoyant jet problems. Technical Report KH-R-18, W.M. Keck Lab. of Hydraulics and Water Resources, Cal. Tech., 1969.

[19] J.M. Chyan H.H. Hwung and Y.H. Chang. Wave effects on the mean flow characteristics of turbulent round jets. In *Proc. Int. Symp. Environmental Hydraulics*, pages 109–114, 1991.

[20] H.H. Hwung and J.M. Chyan. The vortex structure of round jets in water waves. In *Intl. Conf. on Physical modelling of transport and dispersion in conjuction with the Garbis H. Keulegan contennial symposium , IAHR, ASCE*, pages 10A.19–10A.24, 1990.

[21] J.-M. Chyan and H.-H. Hwung. On the interaction of a turbulent jet with waves. *J. of Hydraulic Research*, 31:791–810, 1993.

[22] R.R. Hwang W.C. Yang and T.P. Chiang. Effect of surface waves on a buoyant jet. *J. Marine and Env. Eng.*, 3:63–84, 1996.

[23] C.A. Greated. *Lecture notes: Acoustics and dynamics of fluids.*

[24] J.J. Stoker. *Water waves.* Interscience Publishers, 1957.

[25] M. Raffel C. Willert and J. Kompenhans. *Particle Image Velocimetry, A Practical guide.* Springer, 1998.

[26] C. Gray et al. An analysis of the scanning beam piv illumination system. *Meas. Sci. Technol.*, 2:461–468, 1991.

[27] F.P. Schäfer. Principle of dye laser operation. In F.P. Schäfer, editor, *Topics in applied physics. Vol I*, pages 1–89. Springer, 1973.

[28] P.A. Davies D.B. Hann and C.A. Greated. Optical methods and data processing in heat and fluid flow. In *I. Mech. E. Conference Transactions*, pages 397–406, 1998. City University London.

[29] B.B. Snavely. Continuous wave dye lasers i. In F.P. Schäfer, editor, *Topics in applied physics. Vol I*, pages 91–120. Springer, 1973.

[30] K.H. Drexhage. Structure and properties of laser dyes. In F.P. Schäfer, editor, *Topics in applied physics. Vol I*, pages 145–193. Springer, 1973.

[31] A. Melling. Tracer particles and seeding for particle image velocimetry. *Meas. Sci. Tech.*, 8(12):1406–1416, 1997.

[32] C. Gray. PhD thesis, University of Edinburgh, 1989.

[33] H.C. van der Hulst. *Light scattering by small particles.* Dover, 1981.

[34] E. Hecht. *Optics.* Addison-Wesley, 1990.

[35] R.J. Adrian. Image shifting technique to resolve directional ambiguity in double-pulsed velocimetry. *Applied Optics*, 25:3855–3858, 1986.

[36] R.D. Keane and R.J. Adrian. Optimisation of particle image velocimeters part ii: Multiple-pulsed systems. *Meas. Sci. Tech.*, 2:963–974, 1991.

[37] J. Westerweel. PhD thesis, Delft University, 1993.

[38] R.C. Gonzalez and R.E. Woods. *Digital image processing.* Addison Wesley, 1992.

[39] T. Schlike. PhD thesis, University of Edinburgh, 2001.

[40] T.P. Dewhirst. PhD thesis, University of Edinburgh, 1998.

[41] D.R. Lide editor. *Handbook of Chemistry and Physics 74th ed.* CRC, 1993.

[42] Eigenschaften der materie in ihren aggregatzustanden. In *Transport-phanomene I.* Springer-Verlag, 1969.

[43] D.W. Green editor. *Perry's Chemical Engineer's Handbook 7th ed.* McGraw Hill, 1997.

[44] J. Cosgrove. *multisel.exe.* Fluids and acoustics group, Edinburgh University, 1997.

[45] H.C. Earnshaw. PhD thesis, University of Edinburgh, 1997.

[46] J. Wang. PhD thesis, University of Edinburgh, 1998.

[47] C.J. Garrison. A review of drag and inertial forces on circular cylinders. In *Proc. 12th Offshore Tech. Conf.*, pages 205–218, 1980.

[48] T. Bruce and D. Skyner. *Mint trolley interface software.* Fluids and acoustics group, Edinburgh University.

[49] T. Bruce and D. Skyner. *sine wave Mint trolley interface software.* Fluids and acoustics group, Edinburgh University.

[50] *SensiCam operating instructions.* PCO, 1998.

[51] C. Gray. *VidPIV 3.02 Rowan - Camera/shutter control and PIV processing software.* Optical Flow Systems, Edinburgh.

[52] *Instruction manual for Uniblitz models D122, T132 shutter driver, shutter driver/timer.* Vincent Associates, 1995.

[53] J. Entwistle. PhD thesis, University of Edinburgh, 1999.

[54] J. Wang. PhD thesis, University of Edinburgh, 1998.

[55] D. Sharp. *backcal.exe.* Fluids and acoustics group, Edinburgh University, 1997.

[56] D. Sharp. *avsectio.exe.* Fluids and acoustics group, Edinburgh University, 1997.

[57] D. Sharp. *procbmp.exe.* Fluids and acoustics group, Edinburgh University, 1997.